

Journal of Volcanology and Geothermal Research

The rheology of rhyolite magma from the IDDP-1 borehole and Hrafninnuhryggur (Krafla, Iceland) with implications for geothermal drilling

--Manuscript Draft--

Manuscript Number:	VOLGEO-D-24-00113R1
Article Type:	Research Paper
Keywords:	Viscosity; silicic eruption; obsidian; volcanic eruption; rhyolite; relaxation
Corresponding Author:	Fabian Wadsworth Durham University Durham, United Kingdom
First Author:	Fabian Wadsworth
Order of Authors:	Fabian Wadsworth J�r�mie Vasseur Yan Lavall�e Kai-Uwe Hess Jackie E. Kendrick Jonathan M. Castro Daniel Weidendorfer Shane M. Rooyakkers Annabelle Foster Lucy E. Jackson Ben M. Kennedy Alexander R. L. Nichols C. Ian Schipper Bettina Scheu Donald B. Dingwell Tamiko Watson Georgina Rule Taylor Witcher Hugh Tuffen
Abstract:	<p>Changes in rhyolite melt viscosity during magma decompression and degassing exert a first order control on ascent through the crust and volcanic eruption style. These changes have as yet unknown hazard implications for geothermal drilling in pursuit of particularly hot fluids close to magma storage regions. Here, we exploit the situation at Krafla volcano in which rhyolite has both erupted at Earth's surface and been sampled at shallow storage depths via drilling of the 2009 IDDP-1 and 2008 KJ-39 boreholes. We use differential scanning calorimetry to constrain that the IDDP-1 magma quenched to glass at ~700 K, at a rate of between 7 and 80 K.min⁻¹. We measure the equilibrium viscosity of the IDDP-1 rhyolite at temperatures close to the glass transition interval and show that the rhyolite viscosity is consistent with generalized viscosity models assuming a dissolved concentration of wt.%. We couple these results with micro-penetration and concentric cylinder rheometry over a range of potential magma storage temperatures to constrain the response of surficial Krafla rhyolites to stress. The surficial rhyolites at Krafla match the same viscosity model, assuming a lower dissolved concentration of wt.%. Our results show that at a storage temperature of 1123-1193 K, the viscosity of the stored magma is . At the same temperature, the</p>

	<p>viscosity following degassing during ascent to the surface rises to . Finally, we use high-stress compression tests on the Hrafninnuhryggur surface obsidian to determine the onset of unrelaxed behavior and viscoelastic melt rupture or fragmentation pertinent to understanding the melt response to rapid pressure changes that may be associated with further (near-) magma exploration at Krafla. Taken together, we characterize the relaxation and viscosity of these magmas from source-to-surface.</p>
<p>Suggested Reviewers:</p>	<p>Michael J Heap heap@unistra.fr Michael Heap is actively working on geothermal systems and Krafla in particular and therefore would make a key reviewer of this work.</p> <hr/> <p>Alan Whittington alan.whittington@utsa.edu Alan Whittington is expert in the use of geospeedometry that is used herein.</p> <hr/> <p>Alexandra Kushnir alexandra.kushnir@gmail.com Alexandra Kushnir is an expert in geothermal and hydrothermal systems.</p> <hr/> <p>Michael Cassidy m.cassidy.1@bham.ac.uk Michael Cassidy is an expert in rhyolite systems in general and has insight into the KMT project with which this work is affiliated.</p>
<p>Response to Reviewers:</p>	



Department of Earth Sciences,
Durham University,
Durham, United Kingdom
DH1 3LE
fabian.wadsworth@gmail.com

24th July 2024

Dear Editor,

I am wiring to resubmit the attached manuscript for consideration for publication in the Journal of Volcanology and Geothermal Research. Our manuscript has been reviewed and we have made extensive changes as a result of those reviews. In all cases we have acknowledged and taken on board the reviewer's points and comments and we believe this has led to a real tangible improvement in the paper as a whole; this has been a particularly positive and constructive review process. Below I repeat the points of novelty contained in our paper, which we believe are all the better explained and highlighted in the new version.

Our manuscript contains several points of novelty and interest for a wide readership in both the volcanological and geothermal community.

- (1) We constrain the relaxation and rheological properties of the IDDP-1 borehole rhyolite glass drilled at Krafla volcano, Iceland.
- (2) We constrain the rheology and viscoelastic properties of the Hrafninnuhryggur obsidian found at the surface at Krafla volcano, Iceland.
- (3) We constrain the cooling rate at which both materials formed, which allows us to discuss the likely quench mechanism of the IDDP-1 borehole rhyolite – we find that it quenched during the drilling operation.
- (4) We use the rheology of these materials to validate the Hess & Dingwell (1996) melt viscosity model for use with these rhyolites.

Our work has broad implications for rhyolite systems worldwide, and particularly for those systems that are linked with active geothermal energy production. More specifically, Krafla volcano is emerging as a testbed for a variety of innovative scientific and industrial advances in our understanding of shallow magmatic systems and associated hydrothermal systems. We suggest that our manuscript here submitted will form a cornerstone component of these advances moving forward, and therefore fits with your readership and journal scope.

We look forward to hearing from you.

With very best wishes,

Dr Fabian Wadsworth.

The rheology of rhyolite magma from the IDDP-1 borehole and Hrafninnuhryggur (Krafla, Iceland) with implications for geothermal drilling

Fabian B. Wadsworth¹, Jérémie Vasseur², Yan Lavallée², Kai-Uwe Hess², Jackie E. Kendrick², Jonathan M. Castro³, Daniel Weidendorfer², Shane M. Rooyakkers⁴, Annabelle Foster¹, Lucy E. Jackson¹, Ben M. Kennedy⁵, Alexander R. L. Nichols⁵, C. Ian Schipper⁶, Bettina Scheu², Donald B. Dingwell², Tamiko Watson⁵, Georgina Rule⁵, Taylor Witcher⁷, Hugh Tuffen⁸

¹Department of Earth Sciences, Durham University, DH1 3LE, U.K.

²Earth and Environmental Sciences, Ludwig-Maximilians-Universität, 80333 Munich, Germany.

³Institute of Geosciences, Johannes Gutenberg University, Mainz, Germany.

⁴GNS Science, Lower Hutt 5011, New Zealand, Aotearoa.

⁵School of Earth and Environment, Te Kura Aronukurangi, University of Canterbury, Te Whare Wānanga o Waitaha, Private Bag 4800, Christchurch, Ōtautahi, 8140, New Zealand, Aotearoa.

⁶School of Geography, Environment, and Earth Sciences, Te Herenga Waka, Victoria University of Wellington, PO Box 600, Wellington, 6140 New Zealand, Aotearoa.

⁷Department of Earth Sciences, Uppsala University, Villavägen 16 75236 Uppsala, Sweden

⁸Lancaster Environment Centre, Lancaster University, Lancaster, United Kingdom.

Orcid IDs

Fabian B. Wadsworth	0000-0002-5341-208X
Jérémie Vasseur	0000-0002-0783-5065
Yan Lavallée	0000-0003-4766-5758
Kai-Uwe Hess	0000-0003-1860-8543
Jackie E. Kendrick	0000-0001-5106-3587
Jonathan M. Castro	0000-0003-4865-1737
Daniel Weidendorfer	0000-0002-6118-9287
Annabelle Foster	0000-0002-1578-5328
Lucy E. Jackson	0000-0002-5047-5982
Ben M. Kennedy	0000-0001-7235-6493
Alexander R. L. Nichols	0000-0002-8298-2882
C. Ian Schipper	0000-0002-9064-3370
Bettina Scheu	0000-0002-0478-1049
Donald B. Dingwell	0000-0002-3332-789X
Shane M. Rooyakkers	0000-0001-6876-0995
Tamiko Watson	
Georgina Rule	
Taylor Witcher	0000-0002-4326-3607
Hugh Tuffen	0000-0001-8829-1751

1 Changes in rhyolite melt viscosity during magma decompression and degassing exert a first order
2 control on ascent through the crust and volcanic eruption style. These changes have as yet
3 unknown hazard implications for geothermal drilling in pursuit of particularly hot fluids close to
4 magma storage regions. Here, we exploit the situation at Krafla volcano in which rhyolite has
5 both erupted at Earth's surface and been sampled at shallow storage depths via drilling of the
6 2009 IDDP-1 and 2008 KJ-39 boreholes. We use differential scanning calorimetry to constrain
7 that the IDDP-1 magma quenched to glass at ~700 K, at a rate of between 7 and 80 K.min⁻¹. We
8 measure the equilibrium viscosity of the IDDP-1 rhyolite at temperatures close to the glass
9 transition interval and show that the rhyolite viscosity is consistent with generalized viscosity
10 models assuming a dissolved H₂O concentration of 2.12 wt.%. We couple these results with
11 micro-penetration and concentric cylinder rheometry over a range of potential magma storage
12 temperatures to constrain the response of surficial Krafla rhyolites to stress. The surficial
13 rhyolites at Krafla match the same viscosity model, assuming a lower dissolved H₂O
14 concentration of 0.12 wt.%. Our results show that at a storage temperature of 1123-1193 K, the
15 viscosity of the stored magma is ~3 × 10⁵ Pa. s. At the same temperature, the viscosity following
16 degassing during ascent to the surface rises to ~2 × 10⁹ Pa. s. Finally, we use high-stress
17 compression tests on the Hrafninnuhryggur surface obsidian to determine the onset of unrelaxed
18 behavior and viscoelastic melt rupture or fragmentation pertinent to understanding the melt
19 response to rapid pressure changes that may be associated with further (near-) magma
20 exploration at Krafla. Taken together, we characterize the relaxation and viscosity of these
21 magmas from source-to-surface.
22
23

24
25 viscosity; silicic eruption; obsidian; magma; volcanic eruption; rhyolite; relaxation
26
27

28 29 1. Introduction

30 The rheology of magmatic liquids exerts a first order control on whether or not a volcanic eruption will
31 be explosive (e.g., Cassidy et al. 2018). Part of the challenge for Earth scientists is to decipher the ways
32 in which rheology evolves during magma ascent through the crust. Physical and chemical processes
33 such as bubble growth (Sparks 1978; Blower et al. 2001; Coumans et al. 2020), crystallization (e.g. La
34 Spina et al., 2021), flash nanolitisation (Di Genova et al. 2020; Cáceres et al. 2020; Pereira et al. 2024),
35 and temperature changes due to cooling (including latent heat effects; Blundy et al. 2006), viscous
36 dissipation as heat, or friction (Mastin 2005; Petcovic and Dufek 2005; Costa et al. 2007; Lavallée et
37 al. 2015a; Kendrick and Lavallée 2022), all lead to rheological changes in the melt phase and feedback
38 with the variable development of multiphase suspension rheology (Mader et al. 2013). A standard
39 approach to understanding melt rheology has been to determine the equilibrium viscosity of melts in
40 the laboratory at relevant magmatic conditions and to use these measurements to calibrate empirical
41 model fits. This approach is underpinned by the range of conditions over which the rheological
42 determinations have now been made, encompassing much of the breadth of temperature and dissolved
43 volatile concentrations extant in magmas in the upper crust (Hess and Dingwell 1996; Giordano et al.
44 2008), and exemplified by the low relative residuals between experimental observations and models.
45 However, in most cases, only volcanic deposits at the Earth's surface are directly accessible, and so
46 there remains a degree of uncertainty in the application of these constitutive rheological models to
47 magma transport and eruption.
48
49

50 Drilling projects such as the Iceland Deep Drilling Project (IDDP) afford an opportunity to access and
51 sample the sub-surface directly. The IDDP-1 borehole was drilled approximately vertically in 2009 at
52 Krafla volcano and was designed to reach 4–5 km below the surface in pursuit of supercritical fluids
53 associated with magmatic intrusions. However, at 2.1 km depth, the drill intercepted rhyolitic magma,
54 evidenced by the appearance of quenched silicic glass chips in the drill cuttings (Friðleifsson et al. 2010;
55 Elders et al. 2011). The borehole assembly was pushed upward for 4 minutes, before the melt was fully
56 quenched by drilling fluid, and became stuck (Friðleifsson et al. 2010; Pálsson et al. 2014). This
57 interception of rhyolitic melt and direct sampling of quenched silicic glass from depth provides a unique
58 opportunity to study a shallow rhyolitic magma *in situ* (Eichelberger 2019; Saubin et al. 2021), as well
59
60
61
62
63
64
65

1 as demonstrating the production potential associated with high-temperature fluids (Ingason et al. 2014).
2 Importantly, there are surface effusive rhyolites exposed within ~2 km of the IDDP-1 drill site (**Fig. 1**)
3 at Krafla (Jónasson 1994; Tuffen and Castro 2009; Rooyakkers et al. 2021b), offering a chance to study
4 compositionally similar rhyolites in both a pre- and post-eruptive state.

5 Prior to the well-known IDDP-1 borehole, the KJ-39 borehole was drilled in 2008, south of the
6 Leibortnar-Vítismór field and ~2.5 km south of IDDP-1 (**Fig. 1**). This was drilled directionally to the
7 east at an angle of 30° from vertical with the same aim as IDDP-1: to access supercritical fluids for
8 geothermal purposes. The drill string reached a maximum down-hole distance of 2.865 km where it was
9 stuck and, after being freed using explosives, the bottom hole assembly was found to contain drill
10 cuttings including quenched silicic glass. This, together with the high down-hole temperatures in excess
11 of the local geotherm, the silicic glass suggested that the hole had intersected magma (Mortensen et al.
12 2010; Rule 2020). Therefore, there are two candidate case studies of deep silicic glass extraction from
13 shallow storage regions at Krafla volcano: KJ-39 and IDDP-1.
14

15 Here, motivated by the need to better understand magma properties and potential response to future (in-
16 situ/near-) magma drilling efforts, such as envisaged in the Krafla Magma Testbed (KMT: see
17 <https://www.kmt.is/>; Eichelberger, 2019; Lavallée et al. *in review*), we constrain the rheology of silicic
18 magmatic liquids in a case-study location where both the stored magma and an erupted equivalent of
19 the same rhyolitic magma can be studied in tandem. These rheological data will inform on-going and
20 future efforts aiming at modelling the potential response of magma to drilling, thus supporting
21 implementation plans and risk mitigation strategies for such endeavors.
22
23
24

25 **2. Materials: Hrafninnuhryggur and IDDP-1**

26 We use rhyolitic glass from two neighboring sites in the Krafla volcanic system: Hrafninnuhryggur
27 ('obsidian ridge') and the IDDP-1 borehole (**Fig. 1**). In both cases the glass is taken to represent the
28 melt phase typical of either system (surface and 2.1 km borehole depth, respectively). While these
29 rhyolites are not thought to be genetically linked, they have similar compositions (**Table 1**; Tuffen and
30 Castro 2009; Hampton et al. 2021; Saubin et al. 2021; Rooyakkers et al. 2021b), overlapping values of
31 $\delta^{18}\text{O}$ (IDDP-1: 3.1‰, Hrafninnuhryggur: 2.92–3.28‰; Hampton et al., 2021), and a similar proposed
32 petrogenesis. The differences in composition are subtle in the context of the influence of compositional
33 differences on properties such as viscosity (Hess et al. 1995). In the context of rheological properties,
34 the key difference between the two materials is the dissolved concentration of volatiles, predominantly
35 H_2O . On petrogenetic grounds, a more appropriate direct choice for the surface expression material
36 might have been the recent rhyolitic eruptive products from the Víti crater (Rooyakkers et al. 2021a),
37 however, this material is not as readily available in large glassy chunks such as at Hrafninnuhryggur
38 for large scale testing. The opportunity for sampling large, broadly homogeneous pieces of the
39 Hrafninnuhryggur obsidian, facilitates the multi-method rheological tests that we deploy here. For
40 these reasons, we use the Hrafninnuhryggur obsidian as a proxy for a surface expression of the IDDP-
41 1 rhyolite encountered during drilling.
42
43
44
45
46

47 **a. Hrafninnuhryggur obsidian**

48 The ~24 ka Hrafninnuhryggur ridge (eruption age from Sæmundsson et al. 2000) represents a shallow
49 intrusive-to-extrusive rhyolite exposure, extending down to a maximum of 95 m below the paleo-
50 surface (Tuffen and Castro 2009; Tuffen et al. 2010; Saubin et al. 2019; Foster et al. 2024). The rhyolitic
51 surface outcrops (not including the feeder dyke outcrops) at Hrafninnuhryggur include obsidian-
52 dominated and devitrified-rhyolite-dominated facies (Castro et al. 2009; Tuffen and Castro 2009). We
53 used the obsidian as our experimental material throughout (note that the devitrified rhyolite is thought
54 to be the crystallized counterpart of the obsidian).
55

56 Across all lithofacies outcropping at Hrafninnuhryggur, the total dissolved H_2O concentration in the
57 obsidian was measured previously by Fourier transform infrared spectroscopy (FTIR) to be between
58 0.11 ± 0.01 (sample OR1605) and 0.20 ± 0.01 (sample OR1705) in wt.% (Tuffen and Castro 2009),
59 where we have converted standard deviation to standard error using the quoted number of analyses per
60
61
62
63
64
65

1 sample. Also using FTIR on obsidian from one section of the Hrafninnuhryggur site, Ryan et al. (2015)
2 measured the H₂O concentration to be 0.11 ± 0.04 wt.%, Seropian et al. (2022) measured 0.11 ± 0.01
3 wt.%, and Weaver et al. (2023) measured 0.10 ± 0.01 wt.%. These ranges of H₂O concentrations are
4 broadly consistent with constraints by thermo-gravimetric analysis in which the bulk mass loss up to a
5 high temperature of 1375 K is assumed to represent a volatile concentration in excess of the solubility
6 at those same temperatures at low partial H₂O pressures of laboratory conditions. Using this method
7 and assuming the volatiles are dominated by H₂O, Wadsworth et al., (2018) and Wadsworth et al.,
8 (2019) found 0.14 ± 0.03 wt.%, and 0.15 ± 0.03 wt.% H₂O, respectively.
9

10 **b. IDDP-1 borehole rhyolite**

11 In the case of IDDP-1, chips of both obsidian and felsite were recovered during drilling. Following
12 previous work, we interpret the obsidian chips as representing the quenched product of the melt stored
13 at depth at Krafla. The obsidian chips were all rhyolitic (**Fig. 2**) and contained minor crystallinity
14 (mostly <3 vol.%), consisting of small, <100 μm, crystals of pyroxene, titanomagnetite, and plagioclase
15 (Elders et al. 2011; Zierenberg et al. 2013; Masotta et al. 2018; Saubin et al. 2021). Rare chips
16 containing high crystallinity (55-100 vol.%) are inferred to reflect partial melting of the host felsite
17 (Zierenberg et al., 2013; Masotta et al., 2018), so are not considered here in the context of magma
18 rheology. Typical glass chip internal textures are shown in **Fig. 3**. The dissolved volatile fractions
19 measured previously on these materials are 1.29–2.15 wt. % H₂O (with outlier individual analyses at
20 0.09 and 3.42 wt. %) and a CO₂ concentration on the order of 100 ppm (Elders et al. 2011; Zierenberg
21 et al. 2013; Lowenstern and Pitcher 2013; Watson 2018; Bindeman et al. 2021; Saubin et al. 2021).
22 There is no evidence of magma chemical interaction with the drilling fluids, such as hydration, because
23 the measured OH/H₂O ratio is 1.46–2.53 (Zierenberg et al. 2013). Additionally, no evidence for
24 hydrated margins of individual chips were found in FTIR transects (Watson, 2018). Two-pyroxene
25 geothermometry and modelling of the crystallization sequence suggests in situ storage melt temperature
26 of 1123-1193 K (Zierenberg et al. 2013).
27
28
29
30

31 **c. The Hrafninnuhryggur feeder dyke system**

32 The Hrafninnuhryggur lavas described briefly in Section 2a lie stratigraphically above an intrusive
33 obsidian-dominated rhyolite dyke that is exposed at two depths below the paleo-surface: approximately
34 35–50 m and 95 m (Tuffen et al. 2010; Saubin et al. 2019; Foster et al. 2024). FTIR analyses show that
35 these intrusions have variable H₂O concentrations in the range 0.32–0.53 wt.% (Tuffen and Castro
36 2009; Tuffen et al. 2010; Foster et al. 2024). These outcrops are inferred to represent a shallow conduit
37 region that experienced less degassing than the surface outcrops.
38
39
40

41 **3. Analytical and synthesis methods**

42 We supplement the H₂O concentration analyses of those measured in the Hrafninnuhryggur feeder
43 dyke system with new measurements using a ThermoScientific™ FlashSmart™ elemental analyser
44 which employs a modified Dumas method. Glass chips (2–5 mg) are enclosed in tin containers and
45 combusted in the presence of high purity oxygen with helium as a carrier gas. The combustion products
46 in the gas stream are carried to a gas chromatograph where hydrogen is detected by thermal conductivity
47 and then recalculated to a weight percentage of H₂O using the initial sample mass as a total, and the
48 assumption of complete combustion. This device was calibrated using a BBOT standard and verified
49 with secondary standards before and after measuring each sample. Further details pertaining to this
50 method are provided elsewhere (Moussallam et al. 2016; Weidendorfer et al. 2023).
51

52 In order to calibrate our thermal analysis methods and the manner in which they can reveal information
53 about the viscosity of melts (discussed in Section 4), we synthesize a small aliquot of obsidian with 2
54 wt.% H₂O. To do this, we place 151 mg of powdered obsidian from Hrafninnuhryggur along with 3.1
55 mg of distilled water into a 14 mm long Au capsule (4.0 mm outer diameter, 3.6 mm inner diameter)
56 and seal it shut using a PUK micro-welding system. Then the capsule is loaded into a rapid-quench
57
58
59
60
61
62
63
64
65

1 molybdenum-hafnium-carbide (MHC) cold-seal apparatus. The sample is compressed to 150 MPa using
2 Ar gas as pressure medium before heating the experimental charge to 1273.15 K at a constant heating
3 rate of 15 °C / min. We hold the capsule at those pressure–temperature conditions for 17.5 hours before
4 quenching the run isobarically. The resultant synthesized sample is a natural obsidian but hydrated with
5 2 wt.% H₂O. This sample is referred to later as the ‘hydrated obsidian’.

7 **4. Experimental methods**

8
9 Our experimental methods involved: (1) thermal analysis and (2) rheological determination. The aim
10 of the first approach is to constrain the structural relaxation behavior of both the Hrafninnuhryggur
11 glassy lavas and the IDDP-1 glass chips upon heating. The aim of the second approach is to constrain
12 the rheology of the obsidian lavas at Hrafninnuhryggur. By using existing validated frameworks for
13 silicate melt relaxation dynamics, we can then unify these two approaches and constrain the rheology
14 of the glass at storage conditions intercepted by IDDP-1, and at the Earth’s surface. This workflow is
15 described here.

18 **a. Rheology via thermal analysis using differential scanning calorimetry**

19
20 We use a Netzsch GmbH Pegasus 404c differential scanning calorimeter to constrain the glass transition
21 temperature (as a function of heating or cooling rate) and gain an approximate constraint of the natural
22 cooling rate of the glass samples (Wilding et al. 1996; Gottsmann et al. 2002). We use 30–50 mg chunks
23 of glass loaded into a lidded platinum-rhodium crucible. The crucible is heated in argon or in air at
24 constant rates of heating. The measurement consists of the heat flow (recorded as a voltage in a
25 thermocouple array) at the base of the sample crucible relative to at the base of an empty reference
26 crucible. We perform runs with new samples; first we heated them at 25 K.min⁻¹ to a temperature of
27 823 K (in the case of the IDDP-1 samples) and 1123 K (in the case of the Hrafninnuhryggur obsidian),
28 causing relaxation of the glass and eradication of the thermal history associated with cooling in nature
29 or during drilling. Subsequently we cool the sample at a given rate (e.g., 5, 10, 25 K.min⁻¹) to vitrify
30 the melt and impose a given structural configuration of the glass at a known rate, before heating it again
31 at the same rate to evaluate the glass transition under that matched pair of cooling/heating rates. Then
32 this is repeated at different cooling/heating rate pairs to map shifts in the glass transition under a range
33 of rates. This thermal analysis allows us to find the onset and the peak of the glass transition interval
34 below which the glass is a solid and above which the glass can relax applied stresses viscously. In all
35 cases, we subtract a best-fit baseline (applied to temperatures below the glass transition) from the heat
36 flow data. To do this, we look by eye for the heat flow data that is clearly prior (in temperature) to the
37 onset of the glass transition and fit a polynomial of the form $\beta = d_1 T^{-1} + d_2 T^{-2} + d_3$ (Maier and
38 Kelley 1932) to the data, where β is the heat flow (in arbitrary units), T is the temperature, and d_1 , d_2
39 and d_3 are fit constants. We then subtract this best-fit function from the data in order to render the heat
40 flow curve flat (‘baseline subtracted’) prior to the glass transition.

41
42 The technique of matched cooling-heating runs allows us to observe the dependence of the glass
43 transition on the rate of temperature change (Wilding et al. 1996; Gottsmann et al. 2002), using the
44 semi-empirical relation

$$45 \mu|_{T_g} = \frac{c}{|q|} \quad \text{Eq. 1}$$

46
47 where $\mu|_{T_g}$ is the viscosity assessed at the glass transition temperature T_g , $|q|$ is the absolute value of
48 the heating or cooling rate q , and c is a constant (with units of Pa.K) that relates the viscosity to its
49 imposed prior cooling and re-heating history (sometimes referred to as a ‘shift factor’). c is a weak
50 function of glass composition, and there exists an empirical calibration that relates c to the mol.%
51 cations in the melt that are excess to the charge balancing roles \mathcal{X} dictated by the network-forming
52 cations (Gottsmann et al. 2002). This empirical model is $c = 10.321 - 0.175 \ln(\mathcal{X})$.

For the average of the Hrafninnuhryggur and IDDP-1 compositions given in **Fig. 2** (see **Table 1**), we find that $c \approx 1.21 \times 10^{10}$ Pa.K and $c \approx 1.43 \times 10^{10}$ Pa.K, respectively. These values are found via \mathcal{X} with zero H₂O accommodated in the calculation (i.e., anhydrous compositions); this is discussed later in Section 5). To arrive at these values, we assume that the net effect of iron is not substantial, given that whatever oxidation state we assume (partitioning iron into FeO and Fe₂O₃), the contribution of iron to \mathcal{X} is negligible.

b. Relaxation geospeedometry using differential scanning calorimetry

In silicate glasses, a given property p (such as shear stress) will relax with time proportional to a characteristic relaxation time λ . A common constitutive relaxation equation is the Kohlrausch-Williams-Watts function $p = p_0 \exp[-(t/\lambda)^\zeta]$ where p_0 is the initial value of p prior to relaxation (such as the applied stress), t is time since the onset of relaxation, and ζ is an exponent that, when $\zeta < 1$, stretches the relaxation function beyond a simple exponential, and which is often required to fit data (Kohlrausch 1854; Williams and Watts 1970; Debolt et al. 1976; Kenderes and Whittington 2021). The propensity for glasses to relax a given property underpins the idea behind relaxation geospeedometry in which the functional shape of the evolution of the heat capacity across the glass transition is dictated by the enthalpy relaxation path taken by the glass (Debolt et al. 1976). Because the heat capacity evolution at a given heating rate is dictated by the cooling rate at which the glass was formed, models for heat capacity evolution can be used to extract the cooling rate at which glass forms. The theoretical underpinning of this model is described elsewhere (Debolt et al. 1976; Hodge 2008) and so here we simply introduce the procedural methodology for extracting the cooling rate at which glass – including natural glass – forms.

The fictive temperature T' is the temperature at which the molecular structure of a glass was in equilibrium. At high temperatures far in excess of the glass transition T_g , the fictive temperature and the absolute temperature are equal $T' = T$. If a glass is cooled at a constant rate from the condition that $T' = T$, then at a certain temperature, the glass structure will cease to be in equilibrium because the structure becomes relaxation-limited. A functional model for T' is (Debolt et al. 1976)

$$T' = T_0 + \sum_{j=1}^m (T'_{(j-1)} - T_{(j)}) \left(1 - \exp \left[- \left(\sum_{k=j}^m \frac{T_{(k)} - T_{(k-1)}}{q \lambda_{(k)}} \right)^\zeta \right] \right) \quad \text{Eq. 2}$$

where T_0 is a temperature far from T_g , j is the index of the iteration being performed in Eq. 2, q is the cooling or heating rate, $\lambda_{(k)}$ is the relaxation timescale at index k (i.e., at a given temperature step) and m is the final step. In practice, this is a sum, as shown in Eq. 2, but more properly is an integration procedure. $\lambda_{(k)}$ is given by

$$\lambda_{(k)} = \lambda_0 \exp \left[s \frac{\Delta H}{RT_{(k)}} + (1 - s) \frac{\Delta H}{RT'_{(k-1)}} \right] \quad \text{Eq. 3}$$

where λ_0 and s are fit parameters with $0 < s < 1$ bounds. ΔH is the enthalpy of relaxation. Here R is the universal gas constant. In order to convert Eq. 2 to a heat flow signal, we use

$$\frac{dT'}{dT} = \frac{\beta - \beta_g}{\beta_l - \beta_g} \quad \text{Eq. 4}$$

1 where β is the heat flow signal, β_g is the heat flow signal in the glass (given by the baseline
2 normalization introduced in Section 4a), and β_l is the constant high-temperature heat flow signal for
3 the melt.

4 Procedurally, we use differential scanning calorimetry (introduced in Section 4a) to record the heat flow
5 signal across the glass transition (which is a proxy for the heat capacity). First, we load a sample that
6 was cooled at an unknown rate termed the ‘natural’ cooling rate, and heat it at a known heating rate.
7 This produces a signal that we must model using Eqs 2 & 3 in order to predict the cooling rate at which
8 the glass was originally formed in nature or during drilling. However, for a given glass, ζ , s , ΔH , and
9 λ_0 are all unknowns that depend on glass composition only (Kenderes and Whittington 2021).
10 Therefore, once the natural signal is obtained, we then heat and cool the samples at known matched
11 cooling-heating rates, cycling through the glass transition window. By doing this, we set q in Eq. 2 to
12 a given value that is the case on both the cooling and the subsequent heating cycle. We then minimize
13 using a least-squares regression (Kemmer and Keller 2010) for the fit parameters ζ , s , and λ_0 . We find
14 ΔH by acknowledging $-\ln q = -\ln q_0 + \Delta H/(RT_g)^*$, where q_0 is a fit parameter intercept[†] in a plot
15 of the peak glass transition temperature T_g from the signal as a function of q . Once the fit parameters
16 are determined, the ‘natural’ curve signal can then be fit with only one fit parameter that is q on cooling.
17
18
19
20

21 c. Rheological determination

22 We use a combination of methods to determine the rheology of natural obsidian from
23 Hrafninnuhryggur that, taken together, cover a wide range of applied temperatures and shear stresses.
24 The aim of this multi-method approach is to build a full picture of the melt behavior across all conditions
25 extant in shallow magma transport and eruption.
26

27 First, to determine the viscosity at relatively high temperatures, we use a rotational rheometer in which
28 crushed chips of each raw glass are loaded into thin-walled platinum crucibles and stirred at 1773 K for
29 24 hours, using a Pt₈₀Rh₂₀ spindle to homogenize and remove bubbles. The samples are then removed
30 from the thin-walled synthesis crucible by drilling and hammering. The resulting chips are transferred
31 to a thick walled Pt₈₀Rh₂₀ viscometry crucible of exact geometry and stirred again to ensure
32 homogenization and an absence of bubbles. A Pt₈₀Rh₂₀ viscometry spindle (Dingwell and Virgo 1988)
33 is immersed in the melt and controlled using a Brookfield viscometer which operated at rotation speeds
34 of 0.1–40 rpm. The apparatus, technique, and data processing are described by Dingwell (1989). The
35 technique involves a series of temperature reduction steps with dwells of 1 hour to ensure the system
36 equilibrates thermally, yielding constant torque. The equilibrium torque is then proportional to the shear
37 stress, which is used with the rotation rate to compute the shear viscosity.
38
39

40 At lower temperatures, just above the glass transition interval, we apply the micro-penetration technique
41 (Hess et al. 1995). This involves determining the rate at which a hemispherical iridium indenter
42 displaces the melt when a fixed load is applied. These measurements are applied to the obsidian, cut
43 into 3 mm long plane-parallel discs 5 mm in diameter and polished on both surfaces. The sample is
44 placed in a Netzsch GmbH 402 F1/F3 Hyperion thermo-mechanical analyzer under argon gas flow and
45 the indenter is attached to the vertical push rod. The viscosity is then determined from $\mu =$
46 $\gamma Ft(\xi\alpha^3)^{-1/2}$ where $\gamma = 0.1875$ is a dimensionless constant for a hemispherical indenter, F is the
47 applied force, t is the time since contact of the indenter, ξ is the indenter radius (1 mm in this case) and
48 α is the time dependent distance into the silicate liquid (Pocklington 1940; Tobolsky and Taylor 1963).
49 The viscosity μ is taken at steady-state (high values of t at which $d\alpha/dt$ becomes constant).
50

51 In addition, we can access the relatively low-temperature end of the viscosity spectrum using cylinder
52 compression rheometry, which involves the uniaxial compression of cylinders (Gent 1960; Hess et al.
53
54

55
56 * In some published work there is a 2.303 factor in this equation, which is incorporated when the logarithm to
57 the base 10 is used in place of the natural logarithm (Kenderes and Whittington 2021) which otherwise is not
58 required (Debolt et al. 1976).

59 † We note that in some published sources, what we denote as q_0 is erroneously equated to λ_0 (Kenderes and
60 Whittington 2021), despite the discrepancy in dimensional units between those two parameters.
61
62
63
64
65

2007). We undertook these tests at two scales. At small scale we used a Netzsch GmbH Hyperion® TMA 402 F1 device in which a cylindrical sample 5 mm in diameter and 10 mm in length was set between two ceramic plates and compressed at known applied force (set at 0.1–3 N with 0.2 mN accuracy). The device is encased in a furnace with a maximum temperature of 1775 K and with accuracy (after temperature calibration) of ± 2 K. These measurements are performed in air and sample expansion during heating is subtracted as a baseline prior to deformation. The dependent variable is then the change in sample length with time during pressing. At large scale, compression tests were undertaken at high forces using a 300 kN uniaxial press (from Voggenreiter GmbH with an Instron® hydraulic control system upgrade) on cores of Hrafninnuhryggur obsidian 20 mm in diameter and 40 mm in length. The first iteration (pre-upgrade) of this device and calibration thereof is described in Hess et al. (2007). Linear variable differential transducers (LVDTs) with 10^{-6} m resolution and 150 mm travel range maxima are used with a hydraulic system to operate the position of the upper piston. Force is measured with a Lorenz Messtechnik GmbH K11 load cell with 300 kN working range and an approximate accuracy of 0.05%. While the press can operate in force control mode – wherein the position is the dependent variable of interest – we choose to use it in position control – wherein the force variation with time is the dependent variable of interest. In this position-control mode, the working range of piston velocity is $8.3 \times 10^{-7} \leq u \leq 1.0 \times 10^{-2} \text{ m}\cdot\text{s}^{-1}$ (Wadsworth et al. 2018). A Gero GmbH 3-zone split furnace surrounds the sample and the working pistons either side of the sample with a maximum temperature of 1375 K with a maximum temperature gradient ± 5 K on the sample scale in the hot zone. This furnace has a 0.12 m long uniform hot zone when insulated (Cordonnier et al. 2012c). Temperature is recorded using K-type thermocouples in the air, sample, and in contact with the pistons. Moreover, in these large-scale experiments, acoustic emissions (AEs), associated with potential cracking events during deformation (Vasseur et al. 2018), are tracked via two piezoelectric AE broadband transducers with 125 kHz frequency. The AE signals are fed to a 40 dB buffered pre-amplifier, and recorded in a Richter data acquisition system at 20 MHz from Applied Seismology Consultants. AE event onsets are triggered and recorded using continuous signals via an autoregressive-Akaike-Information-Criterion (AE-AIC) event picker (Beyreuther et al. 2010). The AE-AIC works by detecting a signal onset by using a short-term average/long-term average (STA-LTA) detector algorithm with a time-window of 1 and 20 ms respectively, with an STA/LTA threshold of 2. The signal is then denoised with an amplitude threshold of 68 dB, before picking the signal arrival time using the minimum of the computed AE-AIC signal (Vasseur et al. 2015).

In both the small- and large-scale compression experiments, we look for one of two responses of the samples to deformation. First, we look for a viscous response, which is found when the force F required to maintain a given axial deformation rate $\dot{\gamma}$ rises and equilibrates at a constant value in the absence of acoustic emissions above background. When this response is observed, we can use a well-known model for the viscosity of the cylindrical sample (Gent 1960).

$$\mu = \frac{2\pi F h(t)^5}{3V \dot{h} (2\pi h(t)^3 + V)}, \quad \dot{h} = \frac{dh}{dt} \quad \text{Eq. 5}$$

where V is the sample volume, $h(t)$ is the time-dependent sample height, F is the force applied at each instant of time, and \dot{h} is the velocity (the first-time derivative of the changing sample height) of the piston, where $\dot{\gamma} = \dot{h}/h_0$ with h_0 the initial height. The second possible response of a sample to deformation is a brittle one, recognized when the force value drops intermittently in sharp punctuated events which can be attributed to sample cracking. AEs are also indicative of brittle responses. Analysis of these deformation modes is discussed extensively elsewhere (Coats et al. 2018; Wadsworth et al. 2018) and applied here. Eq. 5 assumes no slip between the pistons and the sample cylinder contacts, which is visually confirmed post-experiment (i.e., the top and bottom end sample radius is within uncertainty of the initial radius). We apply the Trouton correction where the internal shear strain rate $\dot{\epsilon}$ is $\dot{\epsilon} \approx 3\dot{\gamma}$.

5. Results and analysis

Our results are divided into (1) the calibration of the shift factor for hydrous rhyolite melts (Section 5a), (2) the determination of the relaxation behavior and associated glass transition temperature intervals for the materials tested herein (Section 5b), (2) a constraint of the temperature-dependence of viscosity (Section 5c), and (3) unrelaxed viscoelastic effects using a universal melt deformation map (Section 5d). Taken together, these results represent characterization of the IDDP-1 and surface rhyolitic magma rheology.

a. Calibrating the shift factor for hydrous rhyolite

The shift factor c used in Eq. 1 is important for understanding the relationship between the relaxation temperature window and the viscosity at the glass transition. Gottsmann et al. (2001) showed that c relates to the excess cations \mathcal{X} but did not test the effect of H₂O. Therefore, we present a calibration test using the synthesized sample of Hrafninnuhryggur composition (remelted) but hydrated to 2 wt.% H₂O. Using a cooling and heating rate of $|q| = 10 \text{ K} \cdot \text{min}^{-1}$, we find that the glass transition peak temperature is $764 \pm 2 \text{ K}$. Measured using the micro-penetration technique (see Section 4), the viscosity at that exact temperature is $8.13 \times 10^{10} \text{ Pa} \cdot \text{s}$ (with an uncertainty of 0.1 log units). Using Eq. 1, this yields a direct determination of the shift factor by $c = \mu|q| = 1.35 \pm 0.31 \times 10^{10} \text{ Pa} \cdot \text{K}$.

The above determination of c is within error of the value computed using the anhydrous Hrafninnuhryggur composition $c \approx 1.21 \pm 0.05 \times 10^{10} \text{ Pa} \cdot \text{K}$ and the anhydrous IDDP-1 composition $c \approx 1.43 \pm 0.14 \times 10^{10} \text{ Pa} \cdot \text{K}$ (see Table 1). The uncertainties on these values of c computed using the Gottsmann et al. (2001) method arise from taking $\pm 1\sigma$ standard deviation on the compositions given in Table 1 to compute an upper and lower limit on c . We find that H₂O does not have the same effect on the shift factor as the effect of the mol.% excess cations, and we neglect the effect of H₂O on c when c is computed using Gottsmann et al. (2001). To illustrate this further, if we were to compute c using the Gottsmann et al. (2001) model and assuming that the dissolved H₂O is to be incorporated in the mol.% excess cations (\mathcal{X}), then for 2 wt.% H₂O, we would arrive at $c \approx 8.57 \pm 0.40 \times 10^9 \text{ Pa} \cdot \text{K}$ for the Hrafninnuhryggur base composition (Table 1). This is clearly far lower than the measured value.

The shift factor c relates directly to the shear modulus of the melt G (Schawe and Hess 2019) such that $c = G\omega$, where ω has units of K^{-1} and is approximately of order unity (Sipp and Richet 2002). Given that the shear modulus also depends on the dissolved H₂O concentration in rhyolites (Malfait et al. 2011; Whittington et al. 2012), we can account for this possible effect. We compile data for $G(C_{\text{H}_2\text{O}})$ for rhyolitic melts and demonstrate the weak effect of water on the shear modulus, which can be accounted for by $G(C_{\text{H}_2\text{O}}) = b_1 - b_2 C_{\text{H}_2\text{O}}$ where $b_1 = 30.32 \text{ GPa}$ and $b_2 = 0.42$ (Fig. 4). If we assume that this $G(C_{\text{H}_2\text{O}})$ effect contributes to c by the same factor, then using 2 wt.% H₂O as the approximate nominal value, then we find that the factor by which c would be modified from a dry composition would be 0.97. Applying this to the dry value of c , we find our dry estimate (i.e., for IDDP-1 using the dry Gottsmann et al. 2001 method) would be reduced to $c \approx 1.39 \pm 0.14 \times 10^{10} \text{ Pa} \cdot \text{K}$, which is within error of both the measured value, and the original computed value. This means that if there is an effect of H₂O on G that should be propagated to c , then it is either small or it does not exist, and our measurements cannot distinguish these possibilities. Therefore, we do not directly account for H₂O in our determination and use of c . This requires further dedicated investigation to confirm as a general rule for hydrous silicate melts and further work should aim to reduce the uncertainties in the direct determinations of c .

b. The glass transition of the IDDP-1 and Hrafninnuhryggur rhyolitic magma

We find that the IDDP-1 chips have a glass transition onset of $697 \pm 3 \text{ K}$ and peak of $802 \pm 1 \text{ K}$ when analyzed as-collected (Fig. 5a); that is, on ‘first heating’ of the glass chips. Similarly, the Hrafninnuhryggur obsidian has a glass transition onset of $904 \pm 5 \text{ K}$ and peak of $998 \pm 1 \text{ K}$ when analyzed as-collected (Fig. 5a). When we cool the chips and re-heat them at the same rate, we find that the onset remains around $698 \pm 5 \text{ K}$, but the peak is a function of the imposed cooling and heating rate

combination (**Fig. 5b**). The measured peak temperatures on cooling-heating cycles are 773 K (at 5 K.min⁻¹), 783 K (at 10 K.min⁻¹), and 805 K (at 25 K.min⁻¹) (**Fig. 5b**). When we apply the same method to the Hrafninnuhryggur obsidian, we find again that the onset is relatively stable at 923 ± 1.4 K for all heating-cooling cycle rates, but that the peak temperature shifts from 1005 K at 10 K.min⁻¹, up to 1035 K at 30 K.min⁻¹ (**Fig. 5c**). This relative constancy of the onset temperature as well as the dependence of the peak temperature on the imposed thermal history is well documented and underpins the semi-empirical models that aim to convert these temperatures and rate information into equilibrium viscosities (Wilding et al. 1996; Gottsmann et al. 2002). As expected, the glass transition temperature shifts to higher values for higher rates of matched cooling/heating cycles. Interestingly, following geospeedometry interpretations (Wilding et al. 1996; Lavallée et al. 2015b), the similarity of the first-heating heat flow data (**Fig. 5a**) to the 25 K.min⁻¹ matched heating-cooling data (**Fig. 5b**) suggests that the glass chips were quenched during drilling at around 25 K.min⁻¹. The natural quench rate of the Hrafninnuhryggur surface obsidian is slower than 25 K.min⁻¹. In **Fig. 5d** we formally apply the geospeedometry methodology (see Eqs 2–4; Wilding et al. 1996; Lavallée et al. 2015b) to give the computed natural cooling rate for both IDDP-1 and Hrafninnuhryggur. We find that the cooling rate was likely to be between 7 ± 1 and 80 ± 31 K.min⁻¹ for IDDP-1 and around 7 ± 1 K.min⁻¹ for Hrafninnuhryggur.

c. Relaxed melt viscosity

The rheological measurements undertaken at low loads – that is all results obtained from the micro-penetration measurements, the thermo-mechanical analysis, and the uniaxial press under low strain rates – provide a constant ‘relaxed’ value of viscosity and a single value of viscosity for a given temperature, irrespective of the applied conditions. No vesiculation occurred during these tests. Thus, we deem the viscosity obtained to represent the viscosity of a Newtonian system at these conditions. Moreover, the results from the thermal analysis (**Fig. 5**) can be used to estimate the relaxed melt viscosity at the glass transition temperature (**Section 4b**). In order to understand these viscosity values, together with the viscosity values from our rheological study (**Section 4a**), we use the empirical non-Arrhenian Vogel-Fulcher-Tammann (VFT) viscosity law in functional form

$$\mu(T) = \mu_0 \exp\left(\frac{B}{T - T_0}\right) \quad \text{Eq. 6}$$

where μ_0 , B , and T_0 are constants to be determined. As discussed (**Section 1**) the primary difference between the IDDP-1 rhyolite and the surface Hrafninnuhryggur rhyolite is the dissolved H₂O concentration in the melt, which in turn has a first-order control on the viscosity (Hess and Dingwell 1996; Giordano et al. 2008). Hess and Dingwell (1996) used a parameterization via $\mu_0 = a_1 + a_2 \ln(C_{\text{H}_2\text{O}})$, $B = a_3 + a_4 \ln(C_{\text{H}_2\text{O}})$, and $T_0 = a_5 + a_6 \ln(C_{\text{H}_2\text{O}})$ for which $a_1 = -8.163$, $a_2 = 1.918$, $a_3 = 22107$, $a_4 = 5453$, $a_5 = 195.7$ and $a_6 = 32.25$. These constants are found by performing a global minimization of Eq. 3 to experimental test data from published sources (Friedman et al. 1963; Shaw 1963; Burnham 1964; Persikov et al. 1990; Hess et al. 1995; Baker 1996; Dingwell et al. 1996; Schulze et al. 1996; Dorfman et al. 1996; Scaillet et al. 1996) that were collected using similar techniques to those employed herein. Here, we compile those same data in order to visually assess the quality of the minimized model (**Figs 6a & 6c**). We find that the fit is reliable at predicting the data with particular efficacy at $C_{\text{H}_2\text{O}} \leq 4$ wt.% (**Fig. 6a**) which encompasses the values found for IDDP-1 and other Krafla rhyolites (Tuffen and Castro 2009; Zierenberg et al. 2013; Watson 2018; Saubin et al. 2021).

Using our data for Hrafninnuhryggur and for IDDP-1, we can fit the Hess and Dingwell (1996) viscosity model for the best-fit H₂O concentration. To do this, we use a least-squares minimization (Kemmer and Keller 2010). However, in order to capture the uncertainty associated with the shift factor c (see Section 5a), which impacts the viscosity values derived from DSC measurements, we take a Monte Carlo approach. First, we assume that the real value of c is given by a normal probability

distribution with the best estimate c as the mean, and the uncertainty on c as the standard deviation about the mean. Then we draw a value of c from this distribution and use it to locate the DSC data in a viscosity plot (**Fig. 6**). Finally, we fit for H₂O using Hess and Dingwell (1996) via Eq. 3. We then repeat this 10⁶ times, thereby capturing the effect of the uncertainty on c . With the results, we then take the mean and standard deviation of the H₂O concentrations so that the quoted global best-fit value is $C_{\text{H}_2\text{O}}$ and the uncertainty is given by the standard deviation of the best-fit values of H₂O. In the case of IDDP-1, this results in a global fit of $C_{\text{H}_2\text{O}} = 2.12 \pm 0.08$ wt.%. In the case of Hrafninnuhryggur, this results in $C_{\text{H}_2\text{O}} = 0.12 \pm 0.01$ wt.% (we note that ± 0.01 wt.% is the uncertainty on the fit across all data, which is larger than the uncertainty associated with randomly varying c as described above). Other viscosity models could have been used to perform this minimization (Romine and Whittington 2015).

d. Unrelaxed behavior and melt rupture

Here we explore the results of the high-load compression tests in which large 20 mm diameter samples of the Hrafninnuhryggur obsidian were deformed under high relative rates of axial strain. The experiments, which had either a measured force drop, a measured acoustic emission signal, or both, were denoted as brittle, whereas the rest were denoted as viscous. New results presented here are combined with published results using the same obsidian (Tuffen et al. 2008; Wadsworth et al. 2018) and other melts (Dingwell and Webb 1989) in order to explore a universal threshold for unrelaxed melt rupture (brittle) in response to stress.

To analyze our results, we use the framework given by Wadsworth et al. (2018). First, we constrain the melt relaxation timescale $\lambda = \mu/G$ and the deformation timescale $\lambda_d = \dot{\epsilon}^{-1}$, which can be combined in a dimensionless Weissenberg number $Wi = \lambda/\lambda_d = \mu\dot{\epsilon}/G$. Here, $Wi \ll 1$ is the case where the relaxation time is relatively short compared with the deformation time, such that there is sufficient time for relaxation of the melt during flow and bulk relaxed viscous behaviour is expected. By contrast, $Wi \gg 1$ is the case where the deformation time is short and unrelaxed behaviour can be expected. Because significant strain is reached in our tests, the high- Wi regime can result in substantial accumulation of stress and bulk brittle responses. As Wi exceeds a critical value, this can result in solid-like behavior and wholesale melt rupture (Cordonnier et al. 2012c; Coats et al. 2018; Wadsworth et al. 2018). We note that in Coats et al. (2018), Wi is given as a Deborah number De , which should be reserved for oscillatory deformation and is only equivalent to Wi when the Cox-Merz rule is assumed correct. The same brittle regime can be inferred from other work (e.g., via textural analysis and acoustic emission monitoring) even if Wi is not explicitly constrained (Lavallée et al. 2008, 2013; Kendrick et al. 2013). Wadsworth et al. (2018) found that across a wide range of sample compositions, including the Hrafninnuhryggur obsidian, $Wi = 0.04$ is the critical value above which melt will rupture, and that the window $0.01 \leq Wi \leq 0.04$ is the transition from viscous to brittle behavior for increasing Wi .

Our data for the deformation of Hrafninnuhryggur glass matches the prediction that $Wi \geq 0.04$ will result in a brittle response (**Fig. 7**) and push the validation of this viscoelastic theory to lower values of λ (i.e., higher temperatures) and lower values of λ_d (i.e., higher deformation rates) than tested previously.

For comparison we add data from Wadsworth et al. (2024) in which crystal-rich lavas with crystallinities up to 0.55 and low porosity (<0.01) were deformed in the same way. To analyze those samples, Wadsworth et al. (2024) adapt both the relaxation and the deformation timescales to accommodate the presence of crystals and pores. This framework is then compared with previous data for the deformation of natural, porous, crystal-bearing lavas (Lavallée et al. 2007, 2013; Kendrick et al. 2013; Coats et al. 2018), crystal-bearing synthetic glasses (Cordonnier et al. 2012a) and crystal-bearing synthetic glasses with nominally low porosity (Pistone et al. 2012). Here, all of these results are given as ‘Wadsworth et al. (2024)’ on the grounds that the re-calculation of the relaxation and deformation timescales (that locates them in Fig. 7) originates therein. Because these results provide a dimensionless framework for predicting the viscous-to-brittle transition in flowing rhyolites of variable crystallinity, they therefore also show that this deformation map (**Fig. 7**) should be valid for the crystal-bearing components of the sub-surface at Krafla, such as partially molten felsite, or Krafla rhyolite glass that undergoes rapid crystallization (Cáceres et al. 2021).

e. Additional H₂O concentration data for the Hrafninnuhryggur feeder dyke

The H₂O determinations found here for the feeder dyke system are 0.25–0.55 wt.% (see Supplementary Data). These supplement existing data from FTIR for the same feeder dyke rocks (Tuffen and Castro 2009; Foster et al. 2024), data for the surficial lavas (Tuffen and Castro 2009), data for KJ-39 retrieved glass (Rule 2020), and data for chips recovered from IDDP-1 (Zierenberg et al. 2013; Lowenstern and Pitcher 2013; Watson 2018; Bindeman et al. 2021; Saubin et al. 2021). In **Fig. 8** we show a histogram of these H₂O data which reveal the full spectrum of water concentration between the degassing conditions at the surface (at Hrafninnuhryggur) and the average ~1.73 wt.% quenched in during IDDP-1 drilling. Interestingly, the glass chips retrieved from drilling mud show quenched magma can ultimately hold a wide range of H₂O concentrations presumably as variable extents of degassing may take place due to drilling activities prior to quenching. Importantly, the continuum in water concentration in **Fig. 8** indicates that a spectrum of melt viscosity co-exists in the system perturbed by drilling activity.

6. Discussion

Our results constrain the viscosity and viscoelastic rheology (up to and including the brittle limit) of rhyolites at Krafla volcano including the first-order effects of temperature and H₂O concentration. We have exploited the fact that at Krafla, quenched samples of pristine rhyolitic magma are available from both the shallow storage reservoir and the surface, in order to examine how the rheology changes up through the shallow crust. Here, we explore these results in the context of the goals of the Krafla Magma Testbed (KMT) and outline how these results can be used in future work to prepare for new drilling campaigns at Krafla. The aim of the KMT is to pursue further drilling opportunities at Krafla volcano in order to cross a ‘last unexplored frontier’ (see <https://www.kmt.is/>) and monitor and explore our magma filled crust. Ultimately, endeavors such as these are potentially hazardous simply because the response of rhyolite to drilling is poorly understood. Magmas are increasingly considered as desirable environments to augment geothermal energy supply but ultimately, endeavors such as these require a robust quantification of magma rheology.

a. The viscosity and rheology of rhyolites from storage to the surface

Our results relate the H₂O concentrations to the viscosity via the model of Hess and Dingwell (1996) (**Fig. 6**). If we now take the bounds on the predicted IDDP-1 storage temperature of 1123–1193 K (Zierenberg et al. 2013) we can demonstrate how our validated model for the viscosity varies with H₂O concentration (**Fig. 8**). The lower bound on the viscosity at this temperature is the storage viscosity ~1.31 – 5.50 × 10⁵ Pa·s (constrained with the relaxation of IDDP-1 glass chips; **Fig. 6b**), whereas the upper bound on the viscosity at this temperature is the surface viscosity ~2.35 × 10⁹ Pa·s (constrained via relaxation and rheometry using the Hrafninnuhryggur glass; **Fig. 6b**). We can acknowledge that the eruption temperature of the Krafla rhyolites, leading to the emplacement of Hrafninnuhryggur, may be lower than the storage temperature of 1123–1193 K, such that the surface viscosity given in **Fig. 8** could be higher. For example, if we take the lower relative storage temperature estimate for the Chaitén 2008 rhyolite of 1098 K (Castro and Dingwell 2009), then the viscosity would be ~5.62 × 10⁹ Pa·s. Nevertheless, the model constraints provided herein allow this to be computed if the eruption temperature is known.

Here, we focus on the Hess and Dingwell (1996) model for viscosity, which is specifically calibrated for rhyolites. If instead we use a composition-dependent model (Giordano et al. 2008), we see that the differences associated with the small compositional variations between IDDP-1 and Hrafninnuhryggur glasses are minor compared with the effect of dissolved H₂O (**Fig. 8**).

Our results imply that future magma drilling efforts at Krafla as part of KMT must constrain the evolution of dissolved H₂O, due to perturbations in pressure and temperature associated with drilling, in order to predict the evolution of viscosity accurately. Given that these rhyolites have a propensity to

fracture when cooled and pushed to strain at an increased rate (**Fig. 7**), these parameters will be of importance to predict if and/or when brittle failure and fragmentation may occur in response to drilling.

The deformation map presented in Fig. 7 can be used to understand the conditions of strain rate required for failure to occur. However, the deformation map presupposes that the strains will be large (Wadsworth et al. 2018). In fact, it takes a finite time – and therefore strain – for the failure to onset and this time is not accounted for by the deformation map scaling given here. Instead, to find the time for failure we use Maxwell’s viscoelasticity which states

$$\sigma + \frac{\mu}{G} \frac{d\sigma}{dt} = \mu \dot{\epsilon} \quad \text{Eq. 7}$$

where σ is the shear stress in the melt. If $\dot{\epsilon}$ and μ are both constant, as is the case in our experiments, and if $\sigma = 0$ at $t = 0$, then Eq. 7 leads to a prediction of $\sigma(t)$ as

$$\sigma(t) = \mu \dot{\epsilon} \left[1 - \exp\left(-\frac{tG}{\mu}\right) \right]. \quad \text{Eq. 8}$$

Our experimental finding that failure occurs for $Wi \geq 0.04$ is akin to finding that the critical stress for failure is $\sigma_c = 0.04G \approx 4 \times 10^8$ Pa. Eq. 8 can then be used to find the critical time t_c it takes for σ to reach σ_c as

$$t_c = -\frac{\mu}{G} \ln\left(1 - \frac{\sigma_c}{\mu \dot{\epsilon}}\right) \quad \text{Eq. 9}$$

or, as a finite strain required for failure ϵ_c

$$\epsilon_c = -Wi \ln\left(1 - \frac{\sigma_c}{\mu \dot{\epsilon}}\right) \quad \text{Eq. 10}$$

Eqs 9 and 10 then acknowledge that there can be viscous deformation occurring for a finite time (or strain) prior to viscoelastic rupture, which has been confirmed experimentally (Dingwell and Webb 1989; Cordonnier et al. 2012c; Wadsworth et al. 2018; Namiki et al. 2023). Note that Eqs 8–10 are specific to the case where strain rate is held constant and in cases of variable strain rate, a numerical solution to Eq. 7 is required.

b. Potential rheological impact of microlites, nanolites, and iron oxidation

The viscosity of silicate magma is influenced by both melt chemistry and the presence of crystals. In the case of Krafla, the rhyolitic magma contains a high concentration of iron. In **Fig. 9** we report the average glass total iron (FeO_T) as a function of the silica (SiO_2) as compared with rhyolite glasses worldwide using a published database (Di Genova et al. 2017). This shows that the Hrafninnuhryggur obsidian and IDDP-1 glass are among the most iron-rich natural rhyolitic glasses known (Wadsworth et al. 2021a).

Iron can play a role in magma rheology due to changes in oxidation state, which impacts the configuration and role of iron in the melt structure (Dingwell 1991). Additionally, iron can promote crystallization, including the formation of iron-rich nanolites (Mujin et al. 2017; Di Genova et al. 2018, 2020; Cáceres et al. 2020, 2021, 2024; Okumura et al. 2022; Pereira et al. 2024). Interestingly, the

1 precipitation of iron-rich nanolites can have a knock-on effect on the melt viscosity which can, in some
2 cases, be substantial (Zandonà et al. 2023; Cáceres et al. 2024; Pereira et al. 2024). Having said that,
3 the volume fractions of nanolites tend to be small (Okumura et al. 2022), reducing their expected effect
4 on the bulk magma viscosity (Mader et al. 2013; Vasseur et al. 2023) and the direct compositional
5 effects involving the role of iron tends to be small relative to the effects of temperature and water
6 (Chevrel et al. 2014).

7 The formation and growth of Fe-oxide crystals in Krafla rhyolite can result from oxidation of the melt
8 (Cáceres et al. 2021). Contrastingly, Castro et al. (2009) showed that the formation of Fe-oxide crystals
9 can reduce the melt in an oxidation state buffered crystallization step associated with H₂O movement.
10 Casas et al. (2019) used titration methods to determine the iron oxidation ratio in the Hrafninnuhryggur
11 as-collected glass, and found that the ratio of Fe³⁺ to total Fe, termed Fe_T, was Fe³⁺/Fe_T = 0.167,
12 similar to the ‘clear glass’ in the spherulite-bearing samples (Fe³⁺/Fe_T = 0.165 ± 0.04) reported by
13 Castro et al. (2009). Other than these sparse measurements, the oxygen fugacity for each rhyolite body
14 at Krafla is poorly constrained and so this effect of iron on melt structure and rheology should be
15 investigated further in future.

16
17 Our deformation map (Fig. 7) suggests that this growth of any crystals will strongly affect the
18 viscoelastic properties if the crystallization reaches high volume fractions relative to a ‘maximum
19 packing’ fraction (Wadsworth et al. 2024). For example, if crystallinities were to reach ≈ 40 vol. %,
20 then the viscosity would increase by one log unit (Mader et al. 2013). Clearly, iron-bearing nanolites
21 cannot crystallize to such high volume fraction. However, if the rhyolite is stored hot for sufficient time
22 for further crystallization, or if another rhyolite which has crystallized is intersected by drilling at
23 Krafla, then our deformation map can be used to constrain the rheology (Fig. 7).

24
25 Future work should explore whether interactions with drilling fluids and/or drilling-induced
26 decompression and cooling could trigger sufficient oxidation of iron to induce nanolite or microlite
27 formation (Di Genova et al. 2018; Cáceres et al. 2021) before quenching. Importantly, the fact that the
28 clear-glass IDDP-1 glass chips (Saubin et al. 2021), such as the chips used here, conform to the Hess
29 and Dingwell (1996) viscosity model appears to demonstrate that nanolites did not form, based on the
30 assumption that their presence would influence the rheology measured. However, the so-called brown
31 glass explored by Saubin et al. (2021) and others may contain nanolites.

32 33 34 35 36 37 38 **c. The transport system from the source to surface and implications for KMT and** 39 **drilling**

40 We have direct access to rhyolite at the storage region (via IDDP-1) and the surface (via
41 Hrafninnuhryggur) or the near-surface (via the Hrafninnuhryggur feeder dyke system). The surface
42 Hrafninnuhryggur rhyolites appear texturally indistinguishable from effusive lavas (cf Fink 1983).
43 However, Foster et al. (2024) found evidence that these lavas are formed from welding of ash-sized
44 particles, similar to the processes that form welded and rheomorphic ignimbrites (cf Branney and
45 Kokelaar 1992), supporting the so-called ‘cryptic fragmentation’ rhyolite emplacement model
46 (Wadsworth et al. 2020, 2022b) as a basis for rhyolite dyke and lava emplacement. Weaver et al. (2023)
47 additionally showed that secondary vesiculation and sintering occurs in breccia zones. In this model,
48 magma fragmentation is vigorous and occurs at depth, producing pyroclasts that are transported up the
49 conduit where a fraction of the pyroclasts are ‘captured’ at shallow depths and weld to the conduit walls.
50 Those welded deposits are then advected out of the vent as lava. This is pertinent to the drilling scenarios
51 because it suggests that the Krafla rhyolites can readily fragment in vigorous explosive eruptions when
52 subjected to a decompression (Rooyackers et al. 2020).

53
54 The observation during the IDDP-1 drilling was that no catastrophic fragmentation occurred. That is,
55 drilling intercepting magma did not produce an eruption (Ilic et al. 2020). Nevertheless, understanding
56 the range of behaviors that are possible with this rhyolite or any other rhyolite is critical to understanding
57 the generalized suite of possible responses magma could exhibit during drilling.
58
59
60
61
62
63
64
65

1 Traditional conceptual models (those that do not invoke vigorous fragmentation) for silicic lava
2 formation invoke buoyant magma rise with outgassing during ascent (Eichelberger et al. 1986) Jaupart
3 and Allègre 1991; Westrich and Eichelberger 1994; Cassidy et al. 2018). If this is the case, then it is
4 clear how the H₂O concentrations – and associated viscosities at magmatic temperatures – measured
5 here, evolve through the crust. In these models, H₂O is lost through diffusion into nucleating and
6 growing bubbles, and/or into opening fractures (Eichelberger et al. 1986; Gonnermann and Manga
7 2003; Castro et al. 2012). Fracturing, shown to have been occurring in the shallow feeder system at
8 Hrafninnuhryggur during lava emplacement in the brittle field (cf. **Fig. 7**; Wadsworth et al. 2018),
9 would serve to further enhance gas escape (Yoshimura and Nakamura 2008; Sano et al. 2015; Lamur
10 et al. 2017). So the vesiculating, frothing, and fracturing rise of rhyolite during drilling is another
11 scenario that should be explored.

12 In the Wadsworth et al. (2020) model, the majority of H₂O loss from storage to the surface is likely to
13 occur into rapidly growing bubbles prior to and during explosive fragmentation. Upon fragmentation,
14 this H₂O is then liberated into the conduit gas, which separates from the magma and accelerates up and
15 out of the system. Wadsworth et al. (2020) predict that at the fragmentation level (a minimum of 1 km
16 depth), the melt H₂O concentration has already dropped to ~0.5 wt.%. Above this fragmentation point,
17 continued degassing to very low H₂O concentrations is driven by time-dependent diffusive outgassing
18 out of bubbly particles that were formed at fragmentation and which are transported through a relatively
19 low-pressure dusty gas (Wadsworth et al. 2020, 2022b; Weaver et al. 2022). Importantly, this degassing
20 impacts the timescale of sintering (welding) which ultimately shuts the permeable pathways and
21 controls the final concentration of dissolved volatiles in shallow systems (Wadsworth et al. 2021b;
22 Weaver et al. 2023).

25 We highlight here these different models for rhyolite ascent in the crust on the assumption that future
26 drilling into magma has some conceptual similarities to opening up a conduit to the Earth's surface. For
27 this reason, the general behaviour of rhyolite upon decompression and ascent to the surface requires
28 understanding. Our thermal analysis indicates that the IDDP-1 magma underwent the glass transition
29 (T_g) at ~793 K, and was likely quenched at a rate of 7-80 K.min⁻¹ (see **Fig 5**). Considering storage
30 temperatures of ca. 1123–1193 K, the interval between storage temperature and T_g , and the cooling rate
31 through T_g , we have constrained both a thermal window (of ~400 K), and a very abbreviated timescale
32 (~4–60 minutes) during which magma responds physically and chemically to pressure-temperature
33 perturbations imparted by drilling activity.

36 7. Closing remarks

37 We used thermal analysis and several rheological apparatuses to measure the glass transition interval,
38 the cooling rate, the viscosity and the viscoelastic rheological (brittle) limit of Krafla obsidian glass
39 sampled from surficial lava, a shallow dyke, and the drilling mud from IDDP-1. We find that the IDDP-
40 1 glass chips underwent the glass transition at ~793 K, by being quenched at a rate of 7–80 K.min⁻¹,
41 constraining a temperature-time window for physico-chemical perturbation by drilling activity.
42 Rheologically, we use the Hess and Dingwell (1996) model for rhyolites to reproduce the viscosity of
43 the variably hydrous (shallow and deep) rhyolitic magma and demonstrate the weak effect of water on
44 the shear modulus of rhyolitic melts. Our analysis surmises the importance of iron, whose concentration
45 is elevated in Krafla rhyolite, on the potential rheological response of magma to transport or drilling.
46 Finally, our rheological analysis indicates that deformation of aphyric Krafla magma at $Wi \geq 0.04$ will
47 favor a brittle response, and that if partially crystallized (e.g., the felsite capping the magma body) the
48 deformation map provided herein should be valid to model the conditions for viscous flow and
49 fragmentation. We conclude that these rheological constraints on the Krafla rhyolitic magmas at storage
50 and surface conditions should be used in conjunction with simulations of magmatic processes in
51 response to drilling scenarios to provide a scientific basis for hazard assessment and risk mitigation for
52 the KMT project.

1
2
3
4
5
6
7
8
9
10
11
12
13
14
15
16
17
18
19
20
21
22
23
24
25
26
27
28
29
30
31
32
33
34
35
36
37
38
39
40
41
42
43
44
45
46
47
48
49
50
51
52
53
54
55
56
57
58
59
60
61
62
63
64
65

Acknowledgments

We are grateful to the wider Krafla Magma Testbed team for their support and to Landsvirkjun in particular. Thanks to Julia Schunke, Francisco Caceres, Holly Unwin, Ed Llewellyn, and Marize Muniz da Silva for general discussion or field assistance. Funding was provided by the European Research Council (834225-EAVESDROP; 101001065-MODERATE) and by the Natural Environment Research Council of UKRI (grant number NE/T007796/1). Yan Lavallée, Jackie Kendrick, and Donald Dingwell acknowledge support from LMUexcellent, funded by the Federal Ministry of Education and Research (BMBF) and the Free State of Bavaria under the Excellence Strategy of the Federal Government and the Länder. BS acknowledges funding from the European Union's Horizon 2020 research and innovation programme under grant agreement No 858092 (MSCA-ETN IMPROVE). We thank the landowners at Hrafninnuhryggur. Two reviewers and the editor Shane Cronin all helped to improve the manuscript.

References cited

- Baker DR (1996) Granitic melt viscosities: Empirical and configurational entropy models for their calculation. *Am Mineral* 81:126–134. <https://doi.org/10.2138/AM-1996-1-216/PDF>
- Beyreuther M, Barsch R, Krischer L, et al (2010) ObsPy: A Python Toolbox for Seismology. *Seismol Res Lett* 81:530–533. <https://doi.org/10.1785/GSSRL.81.3.530>
- Bindeman IN, Hudak MR, Palandri JP, et al (2021) Rhyolitic and basaltic reference materials for TC/EA analysis: Investigation of water extraction and D/H ratios. *Chem Geol* 583:120486. <https://doi.org/https://doi.org/10.1016/j.chemgeo.2021.120486>
- Blower JD, Mader HM, Wilson SDR (2001) Coupling of viscous and diffusive controls on bubble growth during explosive volcanic eruptions. *Earth Planet Sci Lett* 193:47–56. [https://doi.org/https://doi.org/10.1016/S0012-821X\(01\)00488-5](https://doi.org/https://doi.org/10.1016/S0012-821X(01)00488-5)
- Blundy J, Cashman K, Humphreys M (2006) Magma heating by decompression-driven crystallization beneath andesite volcanoes. *Nature* 443:76–80. <https://doi.org/10.1038/nature05100>
- Branney MJ, Kokelaar P (1992) A reappraisal of ignimbrite emplacement: progressive aggradation and changes from particulate to non-particulate flow during emplacement of high-grade ignimbrite. *Bull Volcanol* 54:504–520. <https://doi.org/10.1007/BF00301396>
- Burnham CW (1964) Viscosity of a H₂O rich pegmatite melt at high pressure. *Geol Soc Am Spec Pap* 76:26
- Cáceres F, Hess K-U, Eitel M, et al (2024) Oxide nanolitisation-induced melt iron extraction causes viscosity jumps and enhanced explosivity in silicic magma. *Nat Commun* 15:604. <https://doi.org/10.1038/s41467-024-44850-x>
- Cáceres F, Scheu B, Hess K-U, et al (2021) From melt to crystals: The effects of cooling on FeTi oxide nanolites crystallisation and melt polymerisation at oxidising conditions. *Chem Geol* 563:120057. <https://doi.org/https://doi.org/10.1016/j.chemgeo.2021.120057>
- Cáceres F, Wadsworth FB, Scheu B, et al (2020) Can nanolites enhance eruption explosivity? *Geology* 48:997–1001. <https://doi.org/10.1130/G47317.1>
- Casas AS, Wadsworth FB, Ayris PM, et al (2019) SO₂ scrubbing during percolation through rhyolitic volcanic domes. *Geochim Cosmochim Acta*. <https://doi.org/10.1016/j.gca.2019.04.013>
- Cassidy M, Manga M, Cashman K, Bachmann O (2018) Controls on explosive-effusive volcanic eruption styles. *Nat Commun* 9:2839. <https://doi.org/10.1038/s41467-018-05293-3>
- Castro JM, Cordonnier B, Tuffen H, et al (2012) The role of melt-fracture degassing in defusing explosive rhyolite eruptions at volcán Chaitén. *Earth Planet Sci Lett* 333–334:63–69. <https://doi.org/https://doi.org/10.1016/j.epsl.2012.04.024>
- Castro JM, Cottrell E, Tuffen H, et al (2009) Spherulite crystallization induces Fe-redox redistribution in silicic melt. *Chem Geol* 268:272–280.

<https://doi.org/https://doi.org/10.1016/j.chemgeo.2009.09.006>

- 1
2 Castro JM, Dingwell DB (2009) Rapid ascent of rhyolitic magma at Chaitén volcano, Chile. *Nature*
3 461:780–783. <https://doi.org/10.1038/nature08458>
- 4 Chevrel MO, Baratoux D, Hess K-U, Dingwell DB (2014) Viscous flow behavior of tholeiitic and
5 alkaline Fe-rich martian basalts. *Geochim Cosmochim Acta* 124:348–365.
6 <https://doi.org/https://doi.org/10.1016/j.gca.2013.08.026>
- 7
8 Coats R, Kendrick JE, Wallace PA, et al (2018) Failure criteria for porous dome rocks and lavas: A
9 study of Mt. Unzen, Japan. *Solid Earth* 9:1299–1328. <https://doi.org/10.5194/se-9-1299-2018>
- 10
11 Cordonnier B, Caricchi L, Pistone M, et al (2012a) The viscous-brittle transition of crystal-bearing
12 silicic melt: Direct observation of magma rupture and healing. *Geology* 40:611–614.
13 <https://doi.org/10.1130/G3914.1>
- 14
15 Cordonnier B, Caricchi L, Pistone M, et al (2012b) The viscous-brittle transition of crystal-bearing
16 silicic melt: Direct observation of magma rupture and healing. *Geology* 40:611–614.
17 <https://doi.org/10.1130/G3914.1>
- 18
19 Cordonnier B, Schmalholz SM, Hess KU, Dingwell DB (2012c) Viscous heating in silicate melts: An
20 experimental and numerical comparison. *J Geophys Res Solid Earth* 117:B02203.
21 <https://doi.org/10.1029/2010JB007982>
- 22
23 Costa A, Melnik O, Vedeneva E (2007) Thermal effects during magma ascent in conduits. *J*
24 *Geophys Res Solid Earth* 112:B12205. <https://doi.org/10.1029/2007JB004985>
- 25
26 Coumans JPP, Llewellyn EWW, Wadsworth FBB, et al (2020) An experimentally validated numerical
27 model for bubble growth in magma. *J Volcanol Geotherm Res* 402:107002.
28 <https://doi.org/https://doi.org/10.1016/j.jvolgeores.2020.107002>
- 29
30 Debolt MA, Easteal AJ, Macedo PB, Moynihan CT (1976) Analysis of Structural Relaxation in Glass
31 Using Rate Heating Data. *J Am Ceram Soc* 59:16–21.
32 <https://doi.org/https://doi.org/10.1111/j.1151-2916.1976.tb09377.x>
- 33
34 Di Genova D, A. BR, M. MH, et al (2020) In situ observation of nanolite growth in volcanic melt: A
35 driving force for explosive eruptions. *Sci Adv* 6:eabb0413.
36 <https://doi.org/10.1126/sciadv.abb0413>
- 37
38 Di Genova D, Caracciolo A, Kolzenburg S (2018) Measuring the degree of “nanotilization” of
39 volcanic glasses: Understanding syn-eruptive processes recorded in melt inclusions. *Lithos* 318–
40 319:209–218. <https://doi.org/https://doi.org/10.1016/j.lithos.2018.08.011>
- 41
42 Di Genova D, Kolzenburg S, Wiesmaier S, et al (2017) A compositional tipping point governing the
43 mobilization and eruption style of rhyolitic magma. *Nature* 552:235–238.
44 <https://doi.org/10.1038/nature24488>
- 45
46 Dingwell DB (1989) Shear viscosities of ferrosilicate liquids. *Am Mineral* 74:1038–1044
- 47
48 Dingwell DB (1991) Redox viscometry of some Fe-bearing silicate melts. *Am Mineral* 76:1560–1562
- 49
50 Dingwell DB, Romano C, Hess KU (1996) The effect of water on the viscosity of a haplogranitic melt
51 under P-T-X conditions relevant to silicic volcanism. *Contrib to Mineral Petrol* 124:19–28.
52 <https://doi.org/10.1007/S004100050170>
- 53
54 Dingwell DB, Virgo D (1988) Viscosities of melts in the Na₂OFeOFe₂O₃SiO₂ system and factors
55 controlling relative viscosities of fully polymerized silicate melts. *Geochim Cosmochim Acta*
56 52:395–403. [https://doi.org/10.1016/0016-7037\(88\)90095-6](https://doi.org/10.1016/0016-7037(88)90095-6)
- 57
58 Dingwell DB, Webb SL (1989) Structural relaxation in silicate melts and non-Newtonian melt
59 rheology in geologic processes. *Phys Chem Miner* 16:508–516
- 60
61 Dorfman A, Hess K-U, Dingwell D (1996) Centrifuge-assisted falling-sphere viscometry. *Eur J*
62 *Mineral* 8:507–514
- 63
64 Eichelberger J (2019) Planning an International Magma Observatory. *Eos (Washington DC)* 100:.
65

<https://doi.org/10.1029/2019eo125255>

- 1 Eichelberger JC, Carrigan CR, Westrich HR, Price RH (1986) Non-explosive silicic volcanism.
2 Nature 323:598–602. <https://doi.org/10.1038/323598a0>
3
- 4 Elders WA, Friðleifsson GÓ, Zierenberg RA, et al (2011) Origin of a rhyolite that intruded a
5 geothermal well while drilling at the Krafla volcano, Iceland. *Geology* 39:231–234.
6 <https://doi.org/10.1130/G31393.1>
7
- 8 Fink JH (1983) Structure and emplacement of a rhyolitic obsidian flow: Little Glass Mountain,
9 Medicine Lake Highland, northern California. *Geol Soc Am Bull* 94:362–380
10
- 11 Foster A, Wadsworth FB, Tuffen H, et al (2024) Evidence for the formation of silicic lava by
12 pyroclast sintering. *Nat Commun* 15:5347. <https://doi.org/10.1038/s41467-024-49601-6>
- 13 Friðleifsson G, ... BP-P of the, 2010 undefined (2010) Iceland Deep Drilling Project. The first IDDP
14 drill hole drilled and completed in 2009. *geothermal-energy.org* 25–29
15
- 16 Friedman I, Long W, Smith RL (1963) Viscosity and water content of rhyolite glass. *J Geophys Res*
17 68:6523–6535
18
- 19 Gent AN (1960) Theory of the parallel plate viscometer. *Br J Appl Phys* 11:85
20
- 21 Giordano D, Russell JK, Dingwell DB (2008) Viscosity of magmatic liquids: a model. *Earth Planet*
22 *Sci Lett* 271:123–134
23
- 24 Gonnermann HM, Manga M (2003) Explosive volcanism may not be an inevitable consequence of
25 magma fragmentation. *Nature* 426:432–435
26
- 27 Gottsmann J, Giordano D, Dingwell DB (2002) Predicting shear viscosity during volcanic processes
28 at the glass transition: a calorimetric calibration. *Earth Planet Sci Lett* 198:417–427.
29 [https://doi.org/https://doi.org/10.1016/S0012-821X\(02\)00522-8](https://doi.org/https://doi.org/10.1016/S0012-821X(02)00522-8)
- 30 Hampton RL, Bindeman IN, Stern RA, et al (2021) A microanalytical oxygen isotopic and U-Th
31 geochronologic investigation and modeling of rhyolite petrogenesis at the Krafla Central
32 Volcano, Iceland. *J Volcanol Geotherm Res* 414:107229.
33 <https://doi.org/https://doi.org/10.1016/j.jvolgeores.2021.107229>
- 34 Hess K-U, Cordonnier B, Lavallée Y, Dingwell DB (2007) High-load, high-temperature deformation
35 apparatus for synthetic and natural silicate melts. *Rev Sci Instrum* 78:75102–75104.
36 <https://doi.org/10.1063/1.2751398>
37
- 38 Hess K-U, Dingwell DB, Webb SL (1995) The influence of excess alkalis on the viscosity of a
39 haplogranitic melt. *Am Mineral* 80:297–304. <https://doi.org/10.2138/AM-1995-3-412>
40
- 41 Hess K-UU, Dingwell DB (1996) Viscosities of hydrous leucogranitic melts: A non-Arrhenian model.
42 *Am Mineral* 81:1297–1300
43
- 44 Hodge IM (2008) A Personal Account of Developments in Enthalpy Relaxation: A Tribute to C. T.
45 Moynihan. *J Am Ceram Soc* 91:766–772. [https://doi.org/https://doi.org/10.1111/j.1551-
46 2916.2007.02127.x](https://doi.org/https://doi.org/10.1111/j.1551-2916.2007.02127.x)
- 47 Ilic O, Sigmundsson F, Lavallée Y, et al (2020) Geological Risk Associated with Drilling into Magma
48 at Krafla Caldera, Iceland: Preliminary Evaluation. In: *Proceedings World Geothermal Congress*
49 *2020*
50
- 51 Ingason K, Kristjánsson V, Einarsson K (2014) Design and development of the discharge system of
52 IDDP-1. *Geothermics* 49:58–65.
53 <https://doi.org/https://doi.org/10.1016/j.geothermics.2013.05.002>
54
- 55 Jaupart C, Allègre CJ (1991) Gas content, eruption rate and instabilities of eruption regime in silicic
56 volcanoes. *Earth Planet Sci Lett* 102:413–429. [https://doi.org/https://doi.org/10.1016/0012-
57 821X\(91\)90032-D](https://doi.org/https://doi.org/10.1016/0012-821X(91)90032-D)
- 58 Jónasson K (1994) Rhyolite volcanism in the Krafla central volcano, north-east Iceland. *Bull*
59 *Volcanol* 56:516–528. <https://doi.org/10.1007/BF00302832>
60
61
62
63
64
65

- 1 Kemmer G, Keller S (2010) Nonlinear least-squares data fitting in Excel spreadsheets. *Nat Protoc*
2 5:267–281. <https://doi.org/10.1038/nprot.2009.182>
- 3 Kenderes SM, Whittington AG (2021) Faster geospeedometry: A Monte Carlo approach to
4 relaxational geospeedometry for determining cooling rates of volcanic glasses. *Chem Geol*
5 581:120385. <https://doi.org/https://doi.org/10.1016/j.chemgeo.2021.120385>
- 6 Kendrick JE, Lavallée Y (2022) Frictional Melting in Magma and Lava. *Rev Mineral Geochemistry*
7 87:919–963. <https://doi.org/10.2138/rmg.2022.87.20>
- 8 Kendrick JE, Lavallée Y, Hess KU, et al (2013) Tracking the permeable porous network during
9 strain-dependent magmatic flow. *J Volcanol Geotherm Res* 260:117–126.
10 <https://doi.org/10.1016/j.jvolgeores.2013.05.012>
- 11 Kohlrausch R (1854) Theorie des elektrischen Rückstandes in der Leidener Flasche. *Ann Phys*
12 167:179–214
- 13 La Spina G, Arzilli F, Llewellyn EW, et al (2021) Explosivity of basaltic lava fountains is controlled
14 by magma rheology, ascent rate and outgassing. *Earth Planet Sci Lett* 553:116658.
15 <https://doi.org/https://doi.org/10.1016/j.epsl.2020.116658>
- 16 Lamur A, Kendrick JE, Eggertsson GH, et al (2017) The permeability of fractured rocks in
17 pressurised volcanic and geothermal systems. *Sci Rep* 7:6173. <https://doi.org/10.1038/s41598-017-05460-4>
- 18 Lavallée Y, Benson PM, Heap MJ, et al (2013) Reconstructing magma failure and the degassing
19 network of domebuilding eruptions. *Geology* 41:515–518. <https://doi.org/10.1130/G33948.1>
- 20 Lavallée Y, Dingwell DB, Johnson JB, et al (2015a) Thermal vesiculation during volcanic eruptions.
21 *Nature* 528:544–547. <https://doi.org/10.1038/nature16153>
- 22 Lavallée Y, Hess K-U, Cordonnier B, Dingwell DB (2007) Non-Newtonian rheological law for highly
23 crystalline dome lavas. *Geology* 35:843–846. <https://doi.org/10.1130/g23594a.1>
- 24 Lavallée Y, Kendrick JE, Eichelberger JC, et al Accessing magma: a necessary revolution in Earth
25 sciences and renewable energies. *Eur Rev*
- 26 Lavallée Y, Meredith PG, Dingwell DB, et al (2008) Seismogenic lavas and explosive eruption
27 forecasting. *Nature* 453:507–510. <https://doi.org/10.1038/nature06980>
- 28 Lavallée Y, Wadsworth FB, Vasseur J, et al (2015b) Eruption and emplacement timescales of
29 ignimbrite super-eruptions from thermo-kinetics of glass shards. *Front Earth Sci* 3:2.
30 <https://doi.org/10.3389/feart.2015.00002>
- 31 Lowenstern JB, Pitcher BW (2013) Analysis of H₂O in silicate glass using attenuated total reflectance
32 (ATR) micro-FTIR spectroscopy‡. *Am Mineral* 98:1660–1668.
33 <https://doi.org/10.2138/am.2013.4466>
- 34 Mader HM, Llewellyn EW, Mueller SP (2013) The rheology of two-phase magmas: A review and
35 analysis. *J Volcanol Geotherm Res* 257:135–158.
36 <https://doi.org/https://doi.org/10.1016/j.jvolgeores.2013.02.014>
- 37 Maier CG, Kelley KK (1932) An equation for the representation of high-temperature heat content
38 data. *J Am Chem Soc* 54:3243–3246. <https://doi.org/10.1021/ja01347a029>
- 39 Malfait WJ, Sanchez-Valle C, Ardia P, et al (2011) Compositional dependent compressibility of
40 dissolved water in silicate glasses. 96:1402–1409. <https://doi.org/doi:10.2138/am.2011.3718>
- 41 Masotta M, Mollo S, Nazzari M, et al (2018) Crystallization and partial melting of rhyolite and felsite
42 rocks at Krafla volcano: A comparative approach based on mineral and glass chemistry of
43 natural and experimental products. *Chem Geol* 483:603–618.
44 <https://doi.org/https://doi.org/10.1016/j.chemgeo.2018.03.031>
- 45 Mastin LG (2005) The controlling effect of viscous dissipation on magma flow in silicic conduits. *J*
46 *Volcanol Geotherm Res* 143:17–28.
47 <https://doi.org/https://doi.org/10.1016/j.jvolgeores.2004.09.008>
- 48
49
50
51
52
53
54
55
56
57
58
59
60
61
62
63
64
65

- 1 Mortensen AK, Grönvold K, Gudmundsson Á, et al (2010) Quenched silicic glass from well KJ-39 in
2 Krafla, North-Eastern Iceland. In: World Geothermal Congress. pp 1–6
- 3 Moussallam Y, Morizet Y, Gaillard F (2016) H₂O–CO₂ solubility in low SiO₂-melts and the unique
4 mode of kimberlite degassing and emplacement. *Earth Planet Sci Lett* 447:151–160.
5 <https://doi.org/https://doi.org/10.1016/j.epsl.2016.04.037>
- 6 Mujin M, Nakamura M, Miyake A (2017) Eruption style and crystal size distributions: Crystallization
7 of groundmass nanolites in the 2011 Shinmoedake eruption. *Am Mineral* 102:2367–2380.
8 <https://doi.org/10.2138/AM-2017-6052CCBYNCND>
- 9 Namiki A, Okumura S, Goto A, Yamada T (2023) In situ observation of glass-like fragmentation of
10 high-temperature silicate melts generating fine ashes. *Commun Earth Environ* 4:155.
11 <https://doi.org/10.1038/s43247-023-00816-3>
- 12 Okumura S, Uesugi K, Goto A, et al (2022) Rheology of nanocrystal-bearing andesite magma and its
13 roles in explosive volcanism. *Commun Earth Environ* 3:241. <https://doi.org/10.1038/s43247-022-00573-9>
- 14 Pálsson B, Hólmgeirsson S, Guðmundsson Á, et al (2014) Drilling of the well IDDP-1. *Geothermics*
15 49:23–30. <https://doi.org/https://doi.org/10.1016/j.geothermics.2013.08.010>
- 16 Pereira L, Linard Y, Wadsworth FB, et al (2024) The rheological response of magma to
17 nanolitisation. *J Volcanol Geotherm Res* 108039.
18 <https://doi.org/https://doi.org/10.1016/j.jvolgeores.2024.108039>
- 19 Persikov ES, Zharikov VA, Bukhtiyarov PG (1990) The effect of volatiles on the properties of
20 magmatic melts. *Eur J Mineral* 621–642. <https://doi.org/10.1127/EJM/2/5/0621>
- 21 Petcovic HL, Dufek JD (2005) Modeling magma flow and cooling in dikes: Implications for
22 emplacement of Columbia River flood basalts. *J Geophys Res Solid Earth* 110:.
23 <https://doi.org/https://doi.org/10.1029/2004JB003432>
- 24 Pistone M, Caricchi L, Ulmer P, et al (2012) Deformation experiments of bubble- and crystal-bearing
25 magmas: Rheological and microstructural analysis. *J Geophys Res Solid Earth* 117:.
26 <https://doi.org/https://doi.org/10.1029/2011JB008986>
- 27 Pocklington HC (1940) Rough measurement of high viscosities. *Math Proc Cambridge Philos Soc*
28 36:507–508. <https://doi.org/10.1017/S0305004100017564>
- 29 Romine WL, Whittington AG (2015) A simple model for the viscosity of rhyolites as a function of
30 temperature, pressure and water content. *Geochim Cosmochim Acta* 170:281–300.
31 <https://doi.org/https://doi.org/10.1016/j.gca.2015.08.009>
- 32 Rooyackers SM, Stix J, Berlo K, et al (2021a) Eruption risks from covert silicic magma bodies.
33 *Geology* 49:921–925. <https://doi.org/10.1130/G48697.1>
- 34 Rooyackers SM, Stix J, Berlo K, et al (2021b) The Origin of Rhyolitic Magmas at Krafla Central
35 Volcano (Iceland). *J Petrol* 62:.. <https://doi.org/10.1093/petrology/egab064>
- 36 Rooyackers SM, Stix J, Berlo K, Barker SJ (2020) Emplacement of unusual rhyolitic to basaltic
37 ignimbrites during collapse of a basalt-dominated caldera: The Halarauður eruption, Krafla
38 (Iceland). *GSA Bull* 132:1881–1902. <https://doi.org/10.1130/B35450.1>
- 39 Rule G (2020) The origin of magma encountered during drilling of geothermal well KJ-39, Krafla,
40 Iceland and the relationship with the nearby IDDP-1 magma. University of Canterbury (pp 127)
- 41 Ryan AG, Russell JK, Hess K-U, et al (2015a) Vesiculation in rhyolite at low H₂O contents: A
42 thermodynamic model. *Geochemistry, Geophys Geosystems* n/a-n/a.
43 <https://doi.org/10.1002/2015GC006024>
- 44 Ryan AG, Russell JK, Nichols ARL, et al (2015b) Experiments and models on H₂O retrograde
45 solubility in volcanic systems. *Am Mineral* 100:774–786. <https://doi.org/10.2138/AM-2015-5030>
- 46 Sæmundsson K, Hjartarson Á, Kaldal I, et al (2012) Geological map of the Northern volcanic zone,
47
48
49
50
51
52
53
54
55
56
57
58
59
60
61
62
63
64
65

Iceland, Northern part. Icel Geosurvey Landsvirkjun, scale 1:

- 1 Sæmundsson K, Pringle MS, Hardarson BS (2000) About the age of strata in the Krafla volcanic
2 system. In: Proceedings of the Geoscience Society of Iceland, Spring Meeting. pp 26–27
3
- 4 Sano K, Wada K, Sato E (2015) Rates of water exsolution and magma ascent inferred from
5 microstructures and chemical analyses of the Tokachi–Ishizawa obsidian lava, Shirataki,
6 northern Hokkaido, Japan. *J Volcanol Geotherm Res* 292:29–40.
7 <https://doi.org/https://doi.org/10.1016/j.jvolgeores.2014.11.015>
8
- 9 Saubin E, Kennedy B, Tuffen H, et al (2021) Textural and geochemical window into the IDDP-1
10 rhyolitic melt, Krafla, Iceland, and its reaction to drilling. 133:1815–1830.
11 <https://doi.org/10.1130/B35598.1>
12
- 13 Saubin E, Kennedy B, Tuffen H, et al (2019) Comparative field study of shallow rhyolite intrusions in
14 Iceland: emplacement mechanisms and impact on country rocks. *J Volcanol Geotherm Res*
15 388:106691. <https://doi.org/10.1016/j.jvolgeores.2019.106691>
16
- 17 Scaillet B, Holtz F, Pichavant M, Schmidt M (1996) Viscosity of Himalayan leucogranites:
18 Implications for mechanisms of granitic magma ascent. *J Geophys Res Solid Earth* 101:27691–
19 27699. <https://doi.org/https://doi.org/10.1029/96JB01631>
20
- 21 Schawe JEK, Hess K-U (2019) The kinetics of the glass transition of silicate glass measured by fast
22 scanning calorimetry. *Thermochim Acta* 677:85–90
23
- 24 Schulze F, Behrens H, Holtz F, et al (1996) The influence of H₂O on the viscosity of a haplogranitic
25 melt. *Am Mineral* 81:1155–1165. <https://doi.org/10.2138/AM-1996-9-1014/PDF>
26
- 27 Seropian G, Kennedy BM, Kendrick JE, et al (2022) Vesiculation of rhyolitic melts under oscillatory
28 pressure. *Front Earth Sci* 219. <https://doi.org/10.3389/FEART.2022.812311>
29
- 30 Shaw HR (1963) Obsidian-H₂O viscosities at 1000 and 2000 bars in the temperature range 700° to
31 900°C. *J Geophys Res* 68:6337–6343. <https://doi.org/https://doi.org/10.1029/JZ068i023p06337>
32
- 33 Sipp A, Richet P (2002) Equivalence of volume, enthalpy and viscosity relaxation kinetics in glass-
34 forming silicate liquids. *J Non Cryst Solids* 298:202–212.
35 [https://doi.org/https://doi.org/10.1016/S0022-3093\(02\)00948-1](https://doi.org/https://doi.org/10.1016/S0022-3093(02)00948-1)
36
- 37 Sparks RSJ (1978) The dynamics of bubble formation and growth in magmas: A review and analysis.
38 *J Volcanol Geotherm Res* 3:1–37. [https://doi.org/https://doi.org/10.1016/0377-0273\(78\)90002-1](https://doi.org/https://doi.org/10.1016/0377-0273(78)90002-1)
39
- 40 Tobolsky A V., Taylor RB (1963) VISCOELASTIC PROPERTIES OF A SIMPLE ORGANIC
41 GLASS. *J Phys Chem* 67:2439–2442. <https://doi.org/10.1021/j100805a044>
42
- 43 Tuffen H, Castro JM (2009) The emplacement of an obsidian dyke through thin ice:
44 Hrafninnuhryggur, Krafla Iceland. *J Volcanol Geotherm Res* 185:352–366
45
- 46 Tuffen H, Owen J, Denton J (2010) Magma degassing during subglacial eruptions and its use to
47 reconstruct palaeo-ice thicknesses. *Earth-Science Rev* 99:1–18.
48 <https://doi.org/https://doi.org/10.1016/j.earscirev.2010.01.001>
49
- 50 Tuffen H, Smith R, Sammonds PR (2008) Evidence for seismogenic fracture of silicic magma. *Nature*
51 453:511–514. <https://doi.org/10.1038/nature06989>
52
- 53 Vasseur J, Wadsworth FB, Dingwell DB (2018) Forecasting Multiphase Magma Failure at the
54 Laboratory Scale Using Acoustic Emission Data. *Front Earth Sci* 6:132.
55 <https://doi.org/10.3389/feart.2018.00132>
56
- 57 Vasseur J, Wadsworth FB, Lavallée Y, et al (2015) Heterogeneity: The key to failure forecasting. *Sci*
58 *Rep* 5:13259. <https://doi.org/10.1038/srep13259>
59
- 60 Wadsworth F Ben, Llewellyn E, Rennie C, et al (2022a) Using obsidian in glass art practice.
61
62
63
64
65

- 1 Wadsworth F, Vasseur J, Casas A, et al (2021a) A model for the kinetics of high temperature
2 reactions between polydisperse volcanic ash and SO₂ gas. *Am Mineral.*
3 <https://doi.org/10.2138/am-2021-7691>
4
- 5 Wadsworth FB, Llewellyn EW, Castro JM, et al (2022b) A reappraisal of explosive–effusive silicic
6 eruption dynamics: syn-eruptive assembly of lava from the products of cryptic fragmentation. *J*
7 *Volcanol Geotherm Res* 107672.
8 <https://doi.org/https://doi.org/10.1016/j.jvolgeores.2022.107672>
9
- 10 Wadsworth FB, Llewellyn EW, Vasseur J, et al (2020) Explosive-effusive volcanic eruption
11 transitions caused by sintering. *Sci Adv* 6:eaba7940. <https://doi.org/10.1126/sciadv.aba7940>
12
- 13 Wadsworth FB, Vasseur J, Heap MJ, et al (2024) A scaling for the viscous-brittle transition in flowing
14 crystal-bearing volcanic dome lavas with implications for the development of permeability
15 anisotropy. *J Volcanol Geotherm Res* (in Rev)
- 16 Wadsworth FB, Vasseur J, Llewellyn EW, et al (2021b) A model for permeability evolution during
17 volcanic welding. *J Volcanol Geotherm Res* 409:107118.
18 <https://doi.org/https://doi.org/10.1016/j.jvolgeores.2020.107118>
19
- 20 Wadsworth FB, Vasseur J, Schaubert J, et al (2019) A general model for welding of ash particles in
21 volcanic systems validated using in situ X-ray tomography. *Earth Planet Sci Lett* 525:115726.
22 <https://doi.org/https://doi.org/10.1016/j.epsl.2019.115726>
23
- 24 Wadsworth FB, Witcher T, Vossen CEJ, et al (2018) Combined effusive-explosive silicic volcanism
25 straddles the multiphase viscous-to-brittle transition. *Nat Commun* 9:1–8.
26 <https://doi.org/10.1038/s41467-018-07187-w>
27
- 28 Watson T (2018) Evolution of magmatic volatiles during drilling into a magma body, Krafla, Iceland.
29 University of Canterbury (pp 129)
- 30 Weaver J, Lamur A, Lea TD, et al (2023) Sintering of vesiculating pyroclasts. *Earth Planet Sci Lett*
31 623:118410. <https://doi.org/https://doi.org/10.1016/j.epsl.2023.118410>
32
- 33 Weaver J, Lavallée Y, Ashraf M, et al (2022) Vesiculation and densification of pyroclasts: A clast-
34 size dependent competition between bubble growth and diffusive outgassing. *J Volcanol*
35 *Geotherm Res* 107550. <https://doi.org/https://doi.org/10.1016/j.jvolgeores.2022.107550>
36
- 37 Webb SL, Dingwell DB (1990) Non-Newtonian rheology of igneous melts at high stresses and strain
38 rates: Experimental results for rhyolite, andesite, basalt, and nephelinite. *J Geophys Res*
39 95:15695–15701
40
- 41 Weidendorfer D, Hess K-U, Ruhekenya RM, et al (2023) Effect of water on the glass transition of a
42 potassium-magnesium carbonate melt. *Philos Trans R Soc A Math Phys Eng Sci* 381:20220355.
43 <https://doi.org/10.1098/rsta.2022.0355>
44
- 45 Westrich HR, Eichelberger JC (1994) Gas transport and bubble collapse in rhyolitic magma: an
46 experimental approach. *Bull Volcanol* 56:447–458. <https://doi.org/10.1007/BF00302826>
47
- 48 Whittington AG, Richet P, Polian A (2012) Amorphous materials: Properties, structure, and
49 durability. Water compressibility Silic Glas A Brillouin Spectrosc study 97:455–467.
50 <https://doi.org/doi:10.2138/am.2012.3891>
- 51 Wilding M, Webb S, Dingwell DB (1996) Tektite cooling rates: calorimetric relaxation
52 geospeedometry applied to a natural glass. *Geochim Cosmochim Acta* 60:1099–1103
53
- 54 Williams G, Watts DC (1970) Non-symmetrical dielectric relaxation behaviour arising from a simple
55 empirical decay function. *Trans Faraday Soc* 66:80–85
56
- 57 Wright FE (1915) Obsidian from Hrafninnuhryggur, Iceland: its lithopliysæ. and surface markings.
58 *GSA Bull* 26:255–286. <https://doi.org/10.1130/GSAB-26-255>
- 59 Yoshimura S, Nakamura M (2008) Diffusive dehydration and bubble resorption during open-system
60 degassing of rhyolitic melts. *J Volcanol Geotherm Res* 178:72–80.
61
62
63
64
65

<https://doi.org/https://doi.org/10.1016/j.jvolgeores.2008.01.017>

1 Zandonà A, Scarani A, Löschmann J, et al (2023) Non-stoichiometric crystal nucleation in a
2 spodumene glass containing TiO₂ as seed former: Effects on the viscosity of the residual melt. J
3 Non Cryst Solids 619:122563. <https://doi.org/https://doi.org/10.1016/j.jnoncrsol.2023.122563>
4

5 Zierenberg RA, Schiffman P, Barfod GH, et al (2013) Composition and origin of rhyolite melt
6 intersected by drilling in the Krafla geothermal field, Iceland. Contrib to Mineral Petrol
7 165:327–347. <https://doi.org/10.1007/s00410-012-0811-z>
8
9

10
11
12
13
14
15
16
17
18
19
20
21
22
23
24
25
26
27
28
29
30
31
32
33
34
35
36
37
38
39
40
41
42
43
44
45
46
47
48
49
50
51
52
53
54
55
56
57
58
59
60
61
62
63
64
65

Table 1 Average renormalized composition of IDDP-1 and Hraftinnuhryggur

Oxide*	IDDP-1 (n=295)	Standard deviation	Hraftinnuhryggur (n=15)	Standard deviation
SiO ₂	77.02	2.81	75.03	0.35
TiO ₂	0.3	0.07	0.24	0.02
Al ₂ O ₃	11.78	1.44	12.33	0.18
FeO _(T) **	2.68	0.56	3.25	0.19
MnO	0.07	0.03	0.14	0.04
MgO	0.19	0.07	0.09	0.02
CaO	1.32	0.44	1.69	0.06
Na ₂ O	3.33	0.43	4.48	0.19
K ₂ O	3.31	0.83	2.75	0.08
Mol. fraction excess cations [#]	0.0256		0.0387	
Anhydrous shift factor, <i>c</i> (Pa.K) ⁺	1.43×10^{10}		1.21×10^{10}	
Reference sources	Zierenberg et al. (2013); Masotta et al. (2018); Saubin et al. (2021)		Tuffen & Castro (2009); Rooyackers et al. (2021)	

*Composition is renormalized to 100% total on an anhydrous basis after taking the average for each oxide

**All iron is assumed to be FeO

[#]Cations excess to charge balancing roles

⁺Computed via Gottsmann et al. (2001)

Table 2. Viscometry data for Krafla rhyolites

Sample	Measurement type	Temperature (K)*	Viscosity (Pa.s)
IDDP-1	Differential scanning calorimetry	772	1.72E+11
IDDP-1	Differential scanning calorimetry	782	8.60E+10
IDDP-1	Differential scanning calorimetry	805	3.44E+10
Hrafn tinnuhryggur	Differential scanning calorimetry	1004	7.28E+10
Hrafn tinnuhryggur	Differential scanning calorimetry	1007	4.86E+10
Hrafn tinnuhryggur	Differential scanning calorimetry	1026	3.17E+10
Hrafn tinnuhryggur	Differential scanning calorimetry	1031	2.80E+10
Hrafn tinnuhryggur	Differential scanning calorimetry	1034	2.60E+10
Hrafn tinnuhryggur	Differential scanning calorimetry	1034	2.43E+10
Hrafn tinnuhryggur	Rotational rheometry	1724	5.13E+03
Hrafn tinnuhryggur	Rotational rheometry	1741	4.37E+03
Hrafn tinnuhryggur	Rotational rheometry	1758	3.24E+03
Hrafn tinnuhryggur	Rotational rheometry	1778	2.24E+03
Hrafn tinnuhryggur	Micropenetration	1053	1.58E+10
Hrafn tinnuhryggur	Micropenetration	1073	8.13E+09
Hrafn tinnuhryggur	Micropenetration	1093	3.47E+09
Hrafn tinnuhryggur	Micropenetration	1033	5.75E+10
Hrafn tinnuhryggur	Uniaxial compression	993	8.93E+10
Hrafn tinnuhryggur	Uniaxial compression	993	7.08E+11
Hrafn tinnuhryggur	Uniaxial compression	1013	4.31E+11
Hrafn tinnuhryggur	Uniaxial compression	1053	1.93E+10
Hrafn tinnuhryggur	Uniaxial compression	1053	4.46E+10
Hrafn tinnuhryggur	Uniaxial compression	1038	3.89E+10
Hrafn tinnuhryggur	Uniaxial compression	1094	3.55E+09
Hrafn tinnuhryggur	Uniaxial compression	1167	3.63E+08
Hrafn tinnuhryggur	Uniaxial compression	1238	4.79E+07

*The temperature values have an associated uncertainty of ± 1 K.

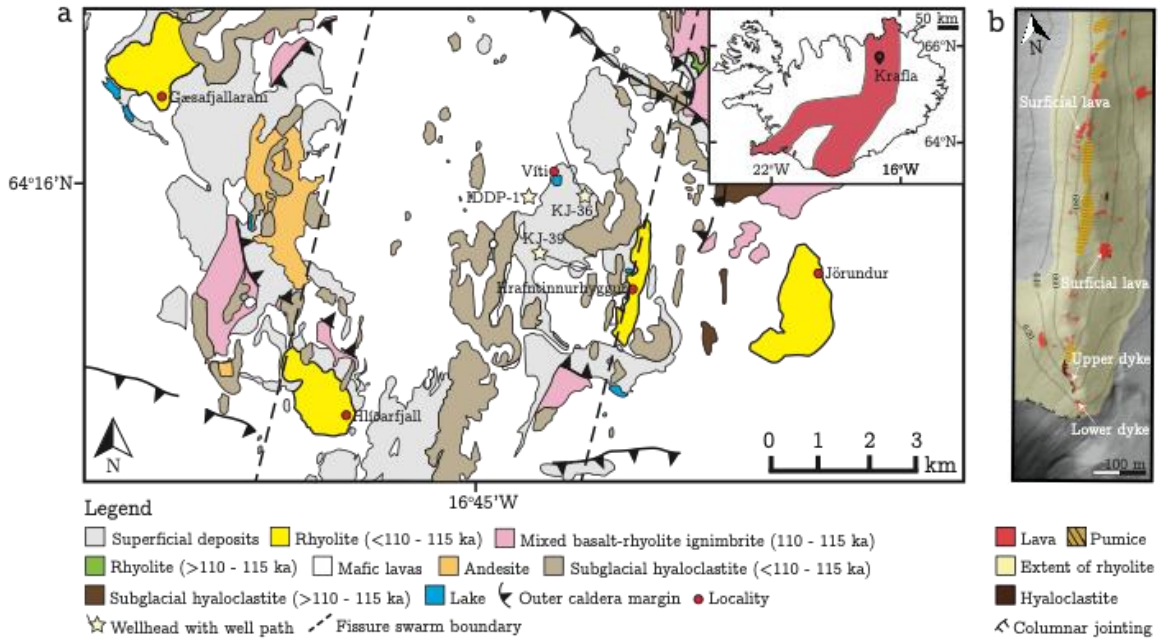


Figure 1. (a) Map of the Krafla volcanic field (Iceland) showing the location of the Hrafninnuhryggur rhyolite, the 2009 IDDP-1 borehole well head (drilled approximately vertically), and the KJ-39 borehole well head (including the slanted projection of the inclined borehole). Additionally shown are other Krafla rhyolites: Víti, Jörundur, Hlíðarfjall, and Gæsafjallaráni. *Inset:* the location of Krafla in the wider Icelandic rift zone(s). This map is simplified from a published source (Sæmundsson et al. 2012). (b) An annotated digital elevation model of the Hrafninnuhryggur ridgeline adapted from Foster et al. (2024) and showing the surficial lava, pumice, and hyaloclastite (country rock) outcrops.

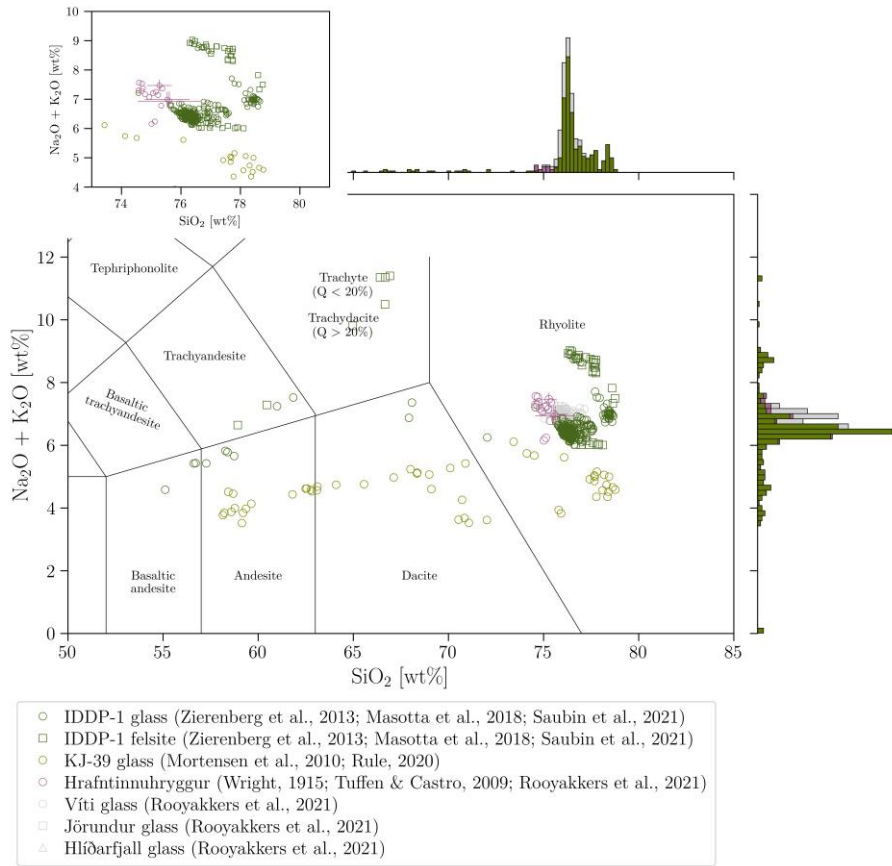


Figure 2. Total-alkali-silica (TAS) plot showing the glass and melt inclusion data available for the rhyolites and borehole glass chips relevant to this study from published sources (Wright 1915; Tuffen and Castro 2009; Mortensen et al. 2010; Zierenberg et al. 2013; Masotta et al. 2018; Rule 2020; Saubin et al. 2021; Rooyakkers et al. 2021b). *Inset:* a zoom-in of the main plot restricted to the rhyolite field and only showing the Hrafninnuhryggur and IDDP-1 datasets, for clarity.

[column width]

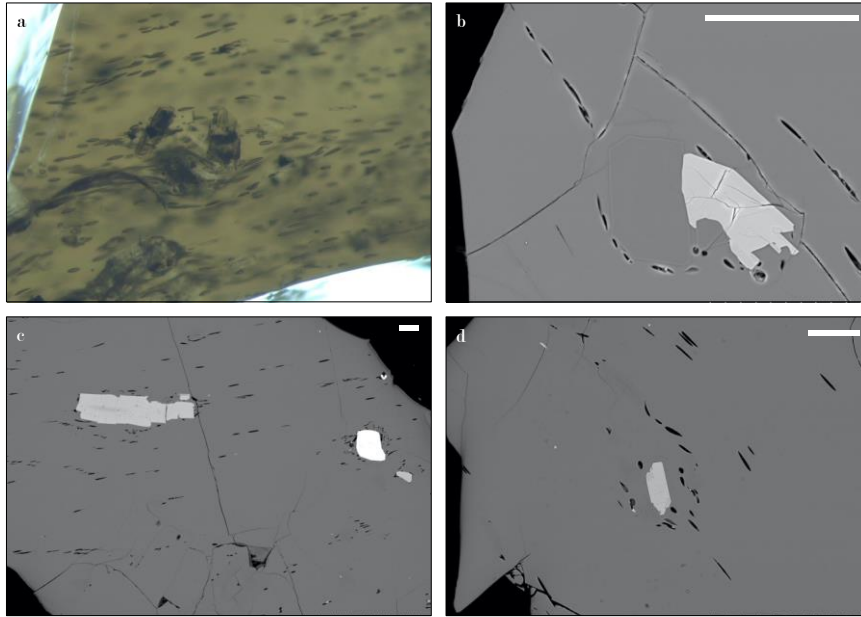


Figure 3. Images of the IDDP-1 glass chip textures. (a) A photomicrograph taken using a binocular microscope and showing deformed vesicles deflected around a local concentration of crystals with a horizontal field of view of 1.6 mm. (b-d) Backscattered electron images showing phenocrysts, groundmass glass, and deformed vesicles. The white scale bar represents 100 μm .

[column width]

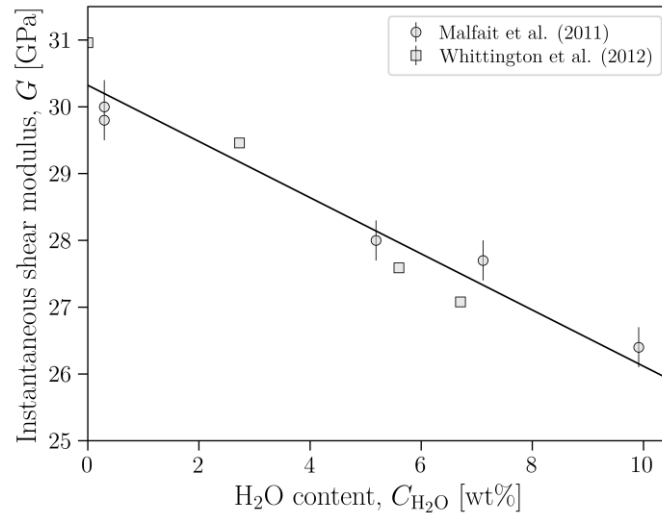


Figure 4. The dependence of the shear modulus of calc-alkaline metaluminous rhyolite melts on H₂O concentrations; circles (Malfait et al. 2011) and squares (Whittington et al. 2012). The linear regression is $G(C_{H_2O}) = b_1 - b_2 C_{H_2O}$ where $b_1 = 30.23$ GPa and $b_2 = 0.42$ and C_{H_2O} is the water content in wt.%.

[column width]

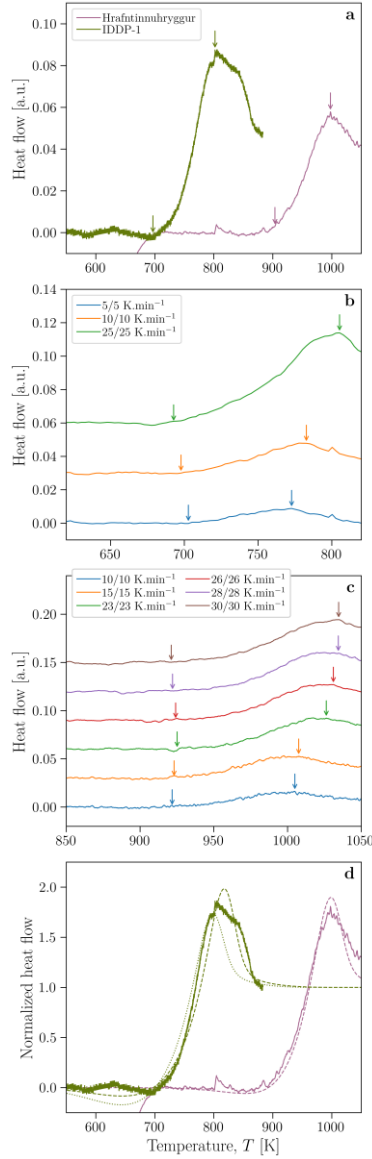


Figure 5. Structural relaxation of IDDP-1 and Hrafninnuhryggur glass chips cast as heat flow (arbitrary units) as a function of temperature as chips are heated at a constant rate. All datasets are baseline-subtracted. (a) The heat flow of an IDDP-1 and a Hrafninnuhryggur glass chip on first heating (heated at 25 K. min^{-1}). For the IDDP-1 signal, we note there is a ‘notch’ on the peak of the glass transition where the arrow is indicating (see panel d). (b) The same IDDP-1 glass chip as used for (a) but here cooled and then reheated at matching rates from 5 K. min^{-1} to 25 K. min^{-1} . In all cases, the onset and peak of the glass transition hump are marked with arrows, found by using a peak-finding algorithm (for the peak) and the intersection of two linear regressions through the curve (for the onset). (c) Heat flow of the same surficial obsidian glass chip from Hrafninnuhryggur as used for (a) at different cooling/heating rate cycles. (d) The same curves as in (a) but here normalized as $(\beta - \beta_g)/(\beta_l - \beta_g)$; see Section 4 for details. The dashed curve fits are the best-fit geospeedometry models (see Section 4b) for cooling rates of 7 K. min^{-1} , for IDDP-1 and Hrafninnuhryggur. The dotted curve on the IDDP-1 signal is the same model but for 80 K. min^{-1} which, by eye, matches the rising signal on the low temperature side of the glass transition peak and appears to better reproduce the ‘notch’ in the peak. This leads us to conclude that $7 - 80 \text{ K. min}^{-1}$ with $\mathcal{O}(50) \text{ K. min}^{-1}$ are reasonable constraints.

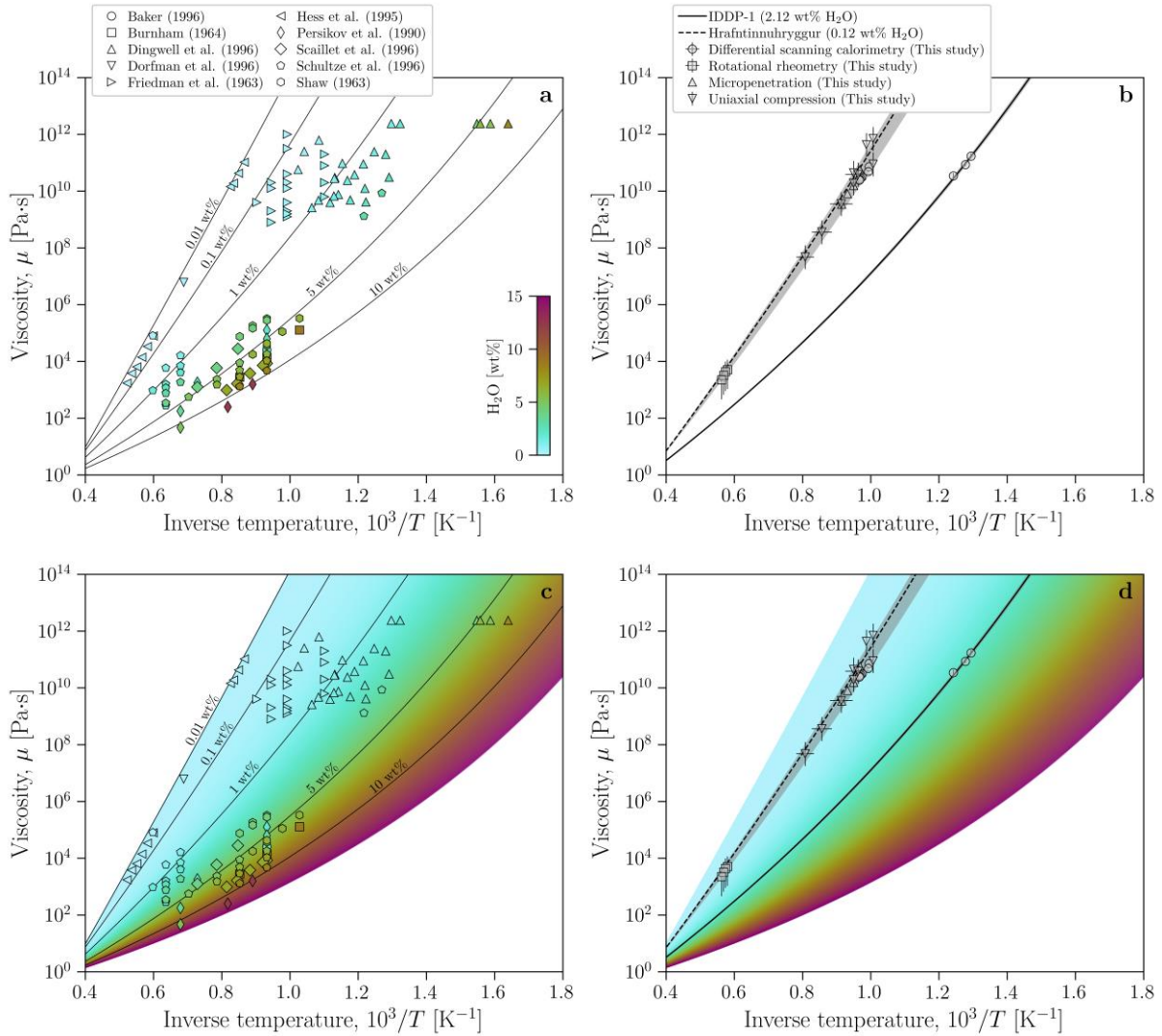


Figure 6. The viscosity of the model rhyolite ‘haplogranite’ system (color-coded) compared with the measured viscosity of the Hrafninnuhryggur rhyolite and IDDP-1 glass chips. (a) The model haplogranite system with data from direct viscometry measurements compiled from published sources (Friedman et al. 1963; Shaw 1963; Burnham 1964; Persikov et al. 1990; Hess et al. 1995; Baker 1996; Dingwell et al. 1996; Schulze et al. 1996; Dorfman et al. 1996; Scaillet et al. 1996) all used to underpin a widely-used rhyolite viscosity model (Hess and Dingwell 1996). Indicative solid curves at chosen water contents 0.01, 0.1, 1, 5, and 10 wt.% are given to help guide the reader. The data symbols are also color-coded in accordance with their measured water content. (b) The same H $_2$ O-dependent rhyolite model as given in (a) but here compared with data from Hrafninnuhryggur (Wadsworth et al. 2022a) and the differential scanning calorimetric constraints provided for IDDP-1 herein (see text). The dashed curve is the Hess and Dingwell (1996) model for 0.12 wt.% H $_2$ O and the solid black curve is the same model for 2.12 wt.% H $_2$ O. The grey band either side of the Hrafninnuhryggur data represents the range of H $_2$ O concentrations measured for Hrafninnuhryggur (upper bound 0.2 wt.%; lower bound 0.1 wt.%; Tuffen and Castro 2009); this band is wider than the uncertainty on the fit for H $_2$ O (± 0.01 wt.%). The grey band either side of the IDDP-1 data represents the Monte Carlo uncertainty (see text) on the best-fit H $_2$ O (± 0.08 wt.%). Panels (c) and (d) are the same as panels (a) and (b), respectively, but with the Hess & Dingwell (1996) model contoured in a continuous color map.

[page width]

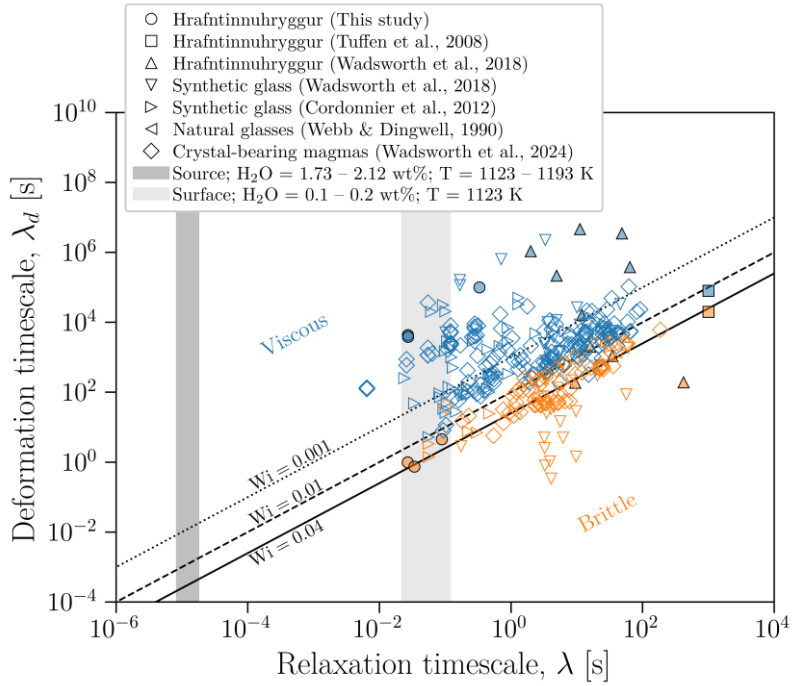


Figure 7. The viscoelastic rheology of rhyolite glass at Krafla, Iceland. We measure the response of samples to deformation at a constant rate of axial strain $\dot{\gamma}$: the response is viscous (blue points) if the evolution of the measured stress evolves smoothly toward an equilibrium value and is brittle (orange points) if there are drops in the stress that are associated with acoustic emissions or audible cracking. Here we compile existing data for synthetic glasses (Cordonnier et al. 2012c; Wadsworth et al. 2018), crystal-bearing glass (Pistone et al. 2012; Cordonnier et al. 2012b), natural glass compositions (Webb and Dingwell 1990), natural dome lavas (Lavallée et al. 2007, 2013; Kendrick et al. 2013; Coats et al. 2018), and Hrafninnuhryggur lavas (Tuffen et al. 2008; Wadsworth et al. 2018). The black curves represent a constant ratio (termed a Weissenberg number Wi) between the deformation timescale and the relaxation timescale of $Wi = 0.04$ (dotted line), $Wi = 0.01$ (dash line), and $Wi = 0.001$ (solid line) (see text). The vertical zones represent the estimated conditions of λ for lava emplacement (labelled ‘surface’) and IDDP-1 (labelled ‘source’ and informed by our rheology estimates; Figs 4 & 5).

[column width]

1
2
3
4
5
6
7
8
9
10
11
12
13
14
15
16
17
18
19
20
21
22
23
24
25
26
27
28
29
30
31
32
33
34
35
36
37
38
39
40
41
42
43
44
45
46
47
48
49
50
51
52
53
54
55
56
57
58
59
60
61
62
63
64
65

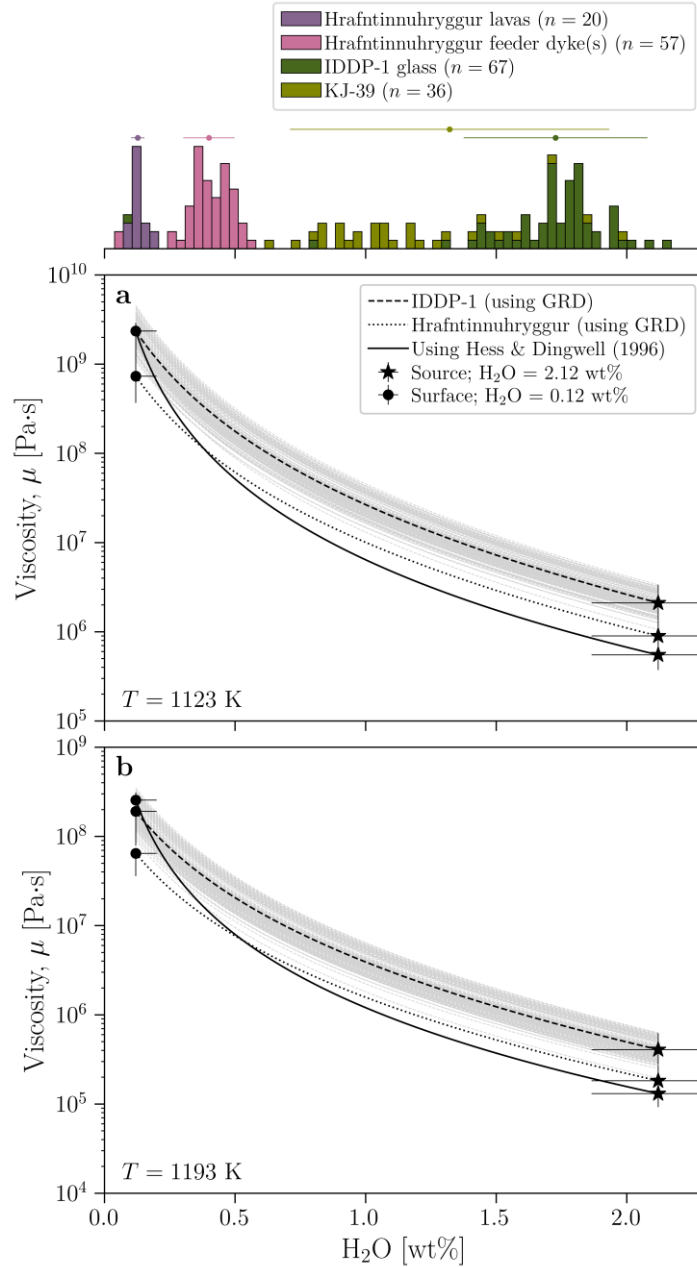


Figure 8. The relationship between the computed viscosity μ and the H_2O concentration in the glass ($C_{\text{H}_2\text{O}}$) showing the estimated source values (stars; derived from calorimetry) and the measured surface values (points) assuming the estimated storage temperature of (a) $T = 1123 \text{ K}$ and (b) $T = 1193 \text{ K}$ (Zierenberg et al. 2013; Masotta et al. 2018). The solid black curve is plotted using the Hess and Dingwell (1996) model (see Fig. 4), the dotted and dashed black curves are plotted using the Giordano et al. (2008) model and an average of the Hrafninnuhryggur and IDDP-1 glass compositions, respectively (see Fig. 1). The grey curves are plotted using the Giordano et al. (2008) model with all individual glass analyses from IDDP-1. Above the plot is a histogram of measured $C_{\text{H}_2\text{O}}$ values from: (1) Hrafninnuhryggur lavas $n = 20$ (Tuffen and Castro 2009; Ryan et al. 2015a; Wadsworth et al. 2019; Seropian et al. 2022); (2) Hrafninnuhryggur feeder dyke(s) approximately 35–50 and 90 m below the paleo-surface $n = 57$ (Tuffen and Castro 2009; Tuffen et al. 2010; Foster et al. 2024); and (3) KJ-39 $n = 36$ (Rule 2020) and IDDP-1 glass chips $n = 67$ (Zierenberg et al. 2013; Lowenstern and Pitcher 2013; Watson 2018; Bindeman et al. 2021; Saubin et al. 2021).

[column width]

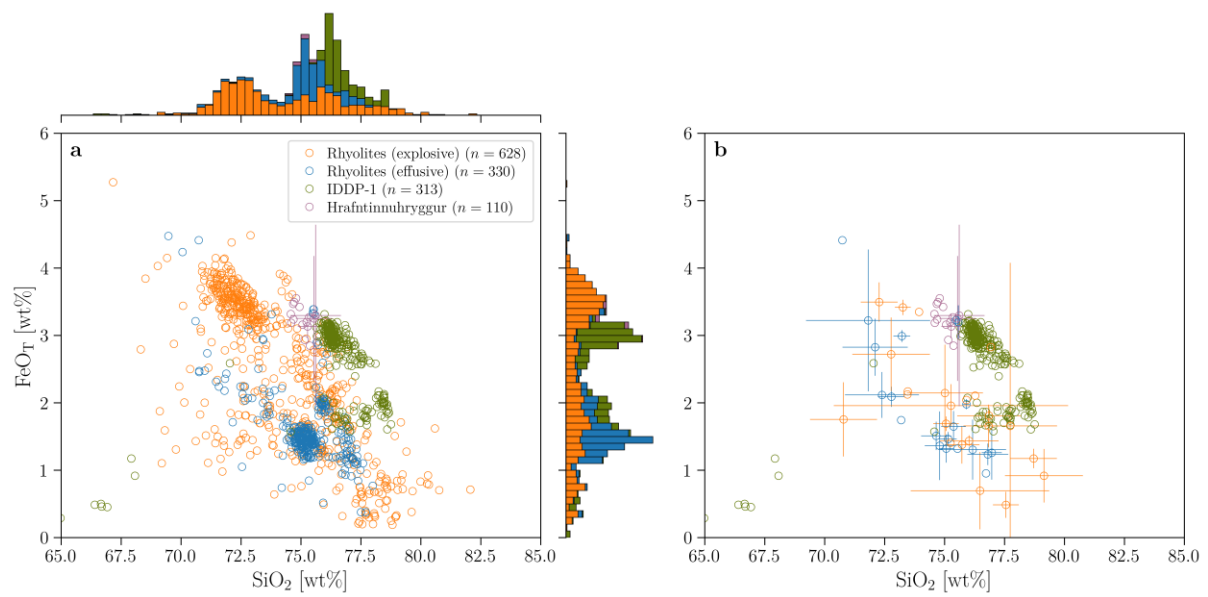


Figure 9. The major element composition of the Hrafninnuhryggur rhyolite glass (purple) and the IDDP-1 glass (green) using the published major element analysis with associated uncertainty (Tuffen and Castro 2009; Zierenberg et al. 2013; Masotta et al. 2018; Saubin et al. 2021). Here, we compare those compositions with rhyolite glass measurements split into the products of explosive eruptions and the products of effusive eruptions worldwide (Di Genova et al. 2017). The Hrafninnuhryggur and IDDP-1 rhyolites are especially iron-rich when compared with a global distribution of effusive lavas (see the histogram associated with the C_{FeO_T} data here) with implications for the propensity for nanolite formation. Compositions are re-normalized to anhydrous 100%. (a) All individual analyses. (b) Only the mean of any given eruption product. Note that (b) is more representative because it acknowledges that most of the high- FeO_T analyses in (a) come from a single eruption (Cordón Caulle 2011-12; Chile).

[page width]

1 Here we repeat the editor and reviewer comments in grey followed by our responses in black. Any
2 changes to the manuscript are copied into this file and are given in **bold black** for the editor's
3 convenience.
4

5 Editor
6

7 Dear Fabian and co-authors
8

9
10 I have received two thorough reviews of your manuscript and along with my own reading of the work,
11 we all agree that the content and topic are of relevance to readers of JVGR. Before it can be published
12 however, there are a series of issues that the reviewers raise, which range from minor corrections to
13 some questions of greater importance. Thus i urge you to carefully work your way through the two
14 review reports and undertake a thorough revision of the work. I am sure a revised presentation will be
15 of much greater value for readers of the journal and for your own benefit in maximising the impact
16 of the work. I note the concerns of R2 about the title of the paper, could you please address this in order
17 to more accurately outline your contribution and/or reduce the ambiguity in the title that R2 observed.
18 The reviewer also raised a few issues of more recent literature that needs to be taken into account.
19
20

21 I look forward to your revised manuscript in due course.
22

23 All best
24 Shane
25

26
27 We thank the editor for their handling of this work and we confirm that we have replied to all reviewer
28 comments, including comments associated with the title of the paper. In what follows our responses
29 and our changes to the manuscript are detailed in full.
30
31
32
33
34
35
36
37
38
39
40
41
42
43
44
45
46
47
48
49
50
51
52
53
54
55
56
57
58
59
60
61
62
63
64
65

1
2
3
4
5
6
7
8
9
10
11
12
13
14
15
16
17
18
19
20
21
22
23
24
25
26
27
28
29
30
31
32
33
34
35
36
37
38
39
40
41
42
43
44
45
46
47
48
49
50
51
52
53
54
55
56
57
58
59
60
61
62
63
64
65

Reviewer 1

This manuscript presents compositional, rheological and calorimetric data for samples from rhyolites at Krafla, including samples quenched on contact with a drill bit and recovered from their storage depth of only ~2.1 km. Cooling rates are extracted from the calorimetric data. Viscosity within the ductile regime fits the predictions of existing models. The brittle-ductile transition is mapped in temperature-time space. Some implications for geothermal drilling are tentatively explored.

This is an accurate summary of the work.

The manuscript is generally well written and contains useful new data. The methods section is long and could be abbreviated with judicious use of citations to previous work but it is actually nice to see detailed methods in the main body of a manuscript rather than having to poke around in supplementary material. In some cases the uncertainties on measurements or derived quantities (cooling rate, water content inferred from rheometry) need to be more clearly stated, or more clearly explained. The discussion could probably be condensed to two sections rather than three by focusing on the implications for geothermal drilling. It should be possible to expand these implications with only a little extra work by considering the strain rate at the drill bit, and the pressure change from rock to drill hole, both of which are likely to have been discussed in the engineering literature.

The reviewer's comments about the methods section length are valid. Indeed, we discussed this among the authorship. We reached the same conclusion as the reviewer that having all methods present in the main body of the text is a positive.

We now provide more detailed descriptions of the data uncertainties. These changes are indicated in response to later comments from this reviewer.

We are not sure how exactly to condense the discussion into just two sections and the reviewer does not suggest which two out of our three sections they think are most appropriate. For that reason, we choose to keep the existing discussion structure as it is. Instead, in keeping with the spirit of what the reviewer has said, we now include an additional discussion section "Implications for geothermal drilling".

The reviewer suggests that the pressure and strain rate near to the drill bit are "likely to have been discussed". We do wish that this were true. But unfortunately, this is not true. In fact, at a recent conference meeting dedicated to the issue of the IDDP1 drilling of Krafla volcano, this was identified as an urgent need for future work in this area. So, while we agree with the reviewer that we could and should have dedicated some analysis to applying our work to the local drill bit conditions, we are not able to at the present time.

Page 1 Abstract Line 7. Should this read "7 and 80" K/min? (c.f. Fig 5)

Yes the reviewer is correct. This has now been changed.

Page 1 Abstract Line 10. The uncertainty value given here is meaningless and confusing, because even if the water content was directly measured, e.g. by FTIR, the uncertainty would be greater than this. I suggest removing it. See comment below for page 9 Results section 5c lines 53-58

We have removed the uncertainties from the abstract, as suggested.

Page 1 Abstract Line 15-17. "In both cases - the rhyolite melt extracted from storage depths, and the surficial rhyolites - the H₂O concentrations inferred from rheometry corroborate direct measurements".

1 This sentence is unnecessary in the abstract - direct measurements of water content are provided,
2 and rheology data would not refute them even if they were not in general agreement.

3 This point is fair and we agree. This statement is removed from the abstract.
4
5

6 Page 2 introduction Line 3 what is the age (or age range) of the surface effusive rhyolites?
7

8 The age of the surface effusive rhyolite is 24 ka. This is given in Section 2a and is not relevant in the
9 introduction line 3. No change is made.
10
11

12 Page 2 introduction Line 33 please cite Table 1 so the reader knows where to look for the compositional
13 analyses.
14
15

16 We have made this addition as suggested although we have added it in Section 2 where the composition
17 of the rhyolites is first mentioned, and not in the introduction's line 33.
18
19
20

21 Page 3 Methods section 3 line 53. How is hydrogen detected by thermal conductivity? Presumably the
22 hydrogen has combusted with oxygen to make H₂O? If adding another sentence or two to explain this
23 technique would be too much of a digression, please provide a citation to the method instead. If glass
24 chips are only 2-5mg, what is the precision of the technique for water content? This is important
25 information, especially for comparison to the ± 0.01 wt% uncertainties being attached to water contents
26 derived from viscosity measurements - see comments below for page 9 Results section 5c lines 53-58.
27
28

29 After combustion, the produced gases are carried by a helium flow through the GC column, which
30 provides the separation of the combustion gases. After separating the gases they are detected by a
31 thermal conductivity method. In the routine analytical protocol all hydrogen is then recalculated to
32 weight percent H₂O relative to the initial sample mass. Oxygen determination has not been performed
33 with the prehydrated glass as the system requires operation in pyrolysis mode and a subsequent sample
34 batch would be required to analyse oxygen itself. The uncertainty on H₂O measurements is plus/minus
35 0.05 wt%. For details on the method we refer to Weidendorfer et al., (2023) and Moussallam et al.
36 (2016) both now cited in the manuscript. We thank the reviewer for this question.
37
38
39

40 Page 8 Results section 5a lines 26-27. How were the uncertainties on the c values from Gottsmann et
41 al. (2002) computed? They are quite different for the two compositions.
42
43

44 We now explain how these uncertainties are found using the following additional text:
45

46 **The uncertainties on these values of c computed using the Gottsmann et al. (2001) method**
47 **arise from taking $\pm 1\sigma$ standard deviation on the compositions given in Table 1 to**
48 **compute an upper and lower limit on c .**
49

50
51 Page 8 Results section 5a lines 42-49. It is unclear which sample is being referred to on line 45. To say
52 that c would be "reduced to $\approx 1.39 \pm 0.14 \times 10^{10}$ PaK" suggests it is IDDP-1. But the comparison with
53 the measured value implies it is Hrafninnuhryggur, for which measurements of c exist for both
54 ~anhydrous and 2 wt.% water content. In any case, the magnitude of this proposed effect of 2 wt.%
55 water on shear modulus (-3% relative) is smaller than the stated uncertainties in the shift factor of both
56 IDDP-1 (1.43 ± 0.29 or $\pm 20\%$ relative) and Hrafninnuhryggur (1.21 ± 0.05 or $\pm 4\%$ relative), so no
57 conclusions can be drawn.
58
59
60
61
62
63
64
65

1 We see the issue being raised by the reviewer. First, the ‘dry composition’ is now clarified to be
2 referring to the IDDP-1 composition but where c is being computed using Gottsmann et al. (2001) and
3 not including H₂O (as per the Gottsmann et al. 2001 methodology of only accounting for excess cations
4 and not volatiles). This is clarified in the main text with this addition:

5 “...we find our dry estimate (i.e. for IDDP-1 using the dry Gottsmann et al. 2001 method)
6 would be...”

7
8
9 Second, the statement made by the reviewer about the uncertainty on c quoted at the start of this section
10 ($\pm 0.29 \times 10^{10}$ Pa. K) is larger than the difference between the quoted value $c = 1.43 \times 10^{10}$ Pa. K and
11 the reduced value $c = 1.39 \times 10^{10}$ Pa. K. The reviewer concludes that this therefore means that no
12 conclusion can be drawn here about the effect of H₂O. We do agree. Our text now reads:

13
14 “...which is within error of both the measured value, and the original computed value.
15 This means that if there is an effect of H₂O on G that should be propagated to c , then it is
16 either small or it does not exist, and our measurements cannot distinguish these
17 possibilities. Therefore we do not directly account for H₂O in our determination and use
18 of c . This requires further dedicated investigation to confirm as a general rule for hydrous
19 silicate melts and further work should aim to reduce the uncertainties in the direct
20 determinations of c .”
21
22

23
24 Page 8 Results section 5b line 56. The values for IDDP-1 are repeated - please provide the correct
25 numbers for Hrafninnuhryggur
26

27 We thank the reviewer for catching this. This is now corrected.
28
29
30

31 Page 9 Results section 5b lines 11-16 / Fig 5d. The caption to Fig 5d says that the dotted curve, which
32 is the modeled heat flow for 80K/min, fits the data better than the dashed curve, which is the modeled
33 heat flow for 7K/min. This is not what visual inspection of the figure suggests, so please explain what
34 the basis for deciding a "better fit" was, e.g. statistical, or fitting only the first half of the peak, etc.
35
36

37 We have now edited the caption to this figure introducing the observation of the ‘notch’ on the peak of
38 the IDDP-1 signal. The higher cooling rate matches the signal to the left of this notch better and is
39 designed to represent the upper bound on the cooling rate. The caption now reads:
40

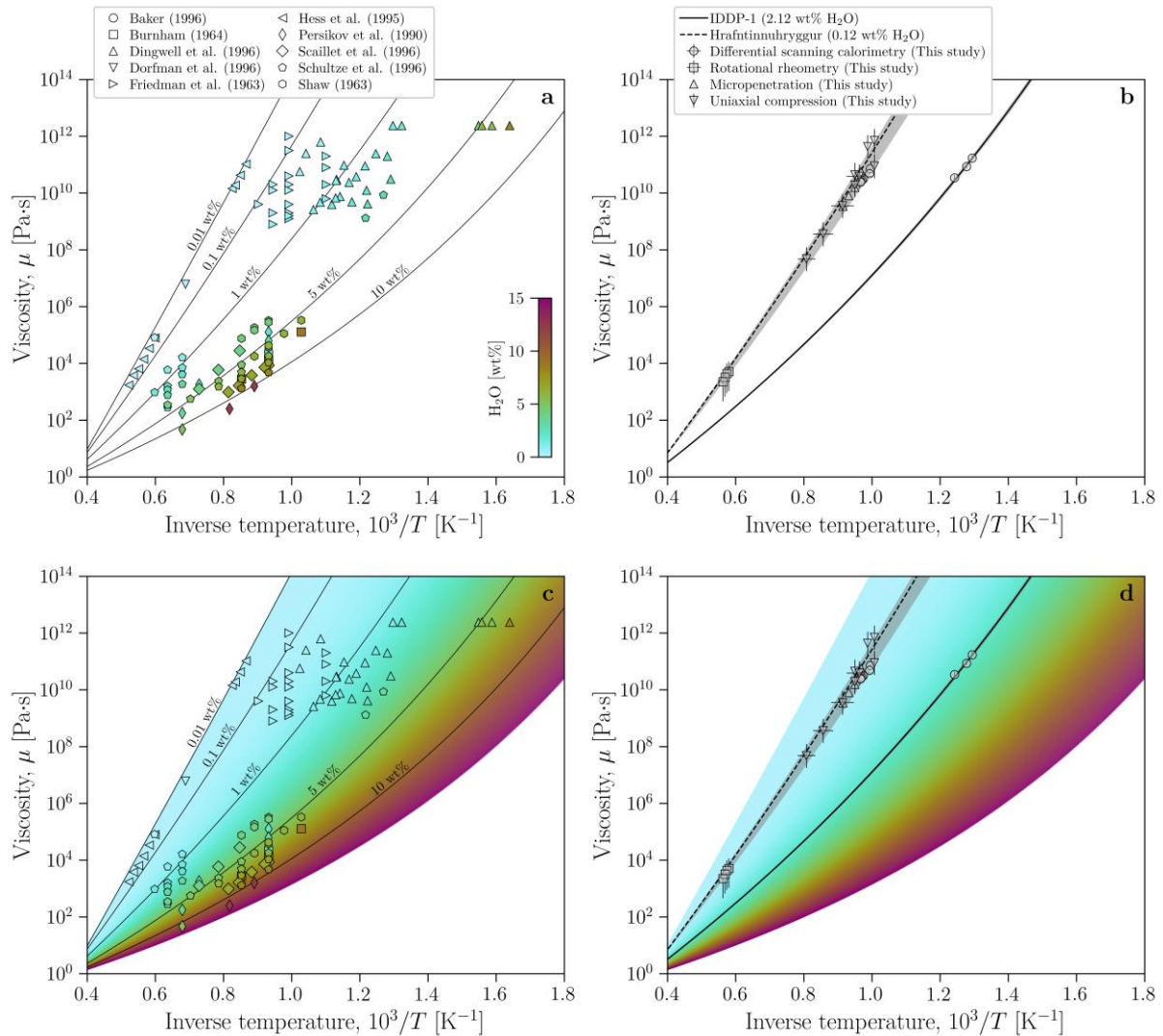
41 Structural relaxation of IDDP-1 and Hrafninnuhryggur glass chips cast as heat flow (arbitrary
42 units) as a function of temperature as chips are heated at a constant rate. All datasets are
43 baseline-subtracted. (a) The heat flow of an IDDP-1 and a Hrafninnuhryggur glass chip on first
44 heating (heated at 25 K. min⁻¹). **For the IDDP-1 signal, we note there is a ‘notch’ on the**
45 **peak of the glass transition where the arrow is indicating (see panel d).** (b) The same IDDP-
46 1 glass chip as used for (a) but here cooled and then reheated at matching rates from 5 K. min⁻¹
47 to 25 K. min⁻¹. In all cases, the onset and peak of the glass transition hump are marked with
48 arrows, found by using a peak-finding algorithm (for the peak) and the intersection of two linear
49 regressions through the curve (for the onset). (c) Heat flow of the same surficial obsidian glass
50 chip from Hrafninnuhryggur as used for (a) at different cooling/heating rate cycles. (d) The
51 same curves as in (a) but here normalized as $(\beta - \beta_g)/(\beta_l - \beta_g)$; see Section 4 for details. The
52 dashed curve fits are the best-fit geospeedometry models (see Section 4b) for cooling rates of
53 7 K. min⁻¹, for IDDP-1 and Hrafninnuhryggur. The dotted curve on the IDDP-1 signal is the
54 same model but for 80 K. min⁻¹ **which, by eye, matches the rising signal on the left-hand**
55 **side of the glass transition peak better and appears to match the ‘notch’ in the peak better.**
56 **This leads us to conclude that 7 – 80 K. min⁻¹ with $\mathcal{O}(50)$ K. min⁻¹ are reasonable**
57 **constraints.**
58
59
60
61
62
63
64
65

Page 9 Results section 5c. Please provide the new rheological data for the two Krafla samples that are plotted in Fig. 6, as a table. These are useful data for the community.

This is now provided as Table 2.

Page 9 Results section 5c lines 47-48. Fig 6 is not particularly helpful in assessing the quality of the fit, because the water contents of the literature data compilation are very hard to see based on the colors of the symbols. This is especially true for readers with imperfect color acuity, and a citation to the quality of fit obtained in the original Hess and Dingwell (1996) paper would suffice.

We now provide a new Figure 6 showing the data with and without the colour-mapped viscosity model of Hess & Dingwell (1996). We believe that this new plot is easier to read and understand. We thank the reviewer for this suggestion.



It would be more useful to compare the new viscosity data presented with the rhyolite viscosity model of Romine and Whittington (2015 <https://doi.org/10.1016/j.gca.2015.08.009>). This model was calibrated on a much larger dataset including hundreds of viscosity measurements on high-silica rhyolites at low water content, similar to the samples studied here. It also has the advantage of

1 incorporating the pressure-dependence of viscosity, which is a consideration when assessing the
2 behavior of magma intercepted at depth during drilling. Although the rhyolite-specific viscosity models
3 are likely to best predict the new data, it is also useful to compare the predictions of the Giordano et
4 al. (2008) model, because there are compositional differences between IDDP-1 and Hrafninnuhryggur.
5 This is presented in Fig 8 and addressed in section 6a but it might make more sense to include this in
6 section 5c, so all comparisons of results to published models are in the same place.

7 We agree with the reviewer that there is value in comparing our dataset with other viscosity models,
8 especially if they can be shown to have been calibrated on a wider range of rhyolite data. Doing this
9 was discussed by the authors during the preparation of this work. However, we decided that the main
10 point of our work here is to provide the determinations of the viscosity, rather than to undertake an
11 inter-comparison of viscosity models in general. Having said that, our acknowledgment that there are
12 other models available was what motivated the use of Giordano et al. (2008) in Figure 8, as noted by
13 the reviewer. Importantly, when applying Giordano et al. (2008), we used *every* compositional
14 measurement available for Hrafninnuhryggur and IDDP-1 (using the data that underpin Table 1 and
15 which are provided as a data supplement). Therefore, we believe that this visual analysis in Figure 8
16 serves the main job of acknowledging other models. We now cite the Romine & Whittington (2015)
17 paper. By not using Romine & Whittington (2015), we do not have to specify a pressure, which is an
18 advantage when we want to compare viscosities across a range of pressures.
19
20
21
22

23 Page 9 Results section 5c lines 53-58. The quoted uncertainties of ± 0.01 wt% H₂O appear unjustified
24 from Figure 6b, where measured viscosity data plot above and below the dashed line representing 0.12
25 wt%. There are only three points for IDDP-1 and they are all from calorimetry, for which the stated
26 uncertainty on the shift factor is enough to introduce more than this level of uncertainty. Bearing in
27 mind the stated weights of glass and water in the capsule (page 4 line 1), the water content should be
28 2.01 wt% not 2.12 wt%, which simply confirms that comparing viscosity data to models is not the best
29 way of assessing water content. Another consideration is that there are many other viscosity models
30 that could be used, and they would all produce slightly different best fit water contents - likely with
31 much more than a 0.01 wt.% variation in best-fit water content. These quoted uncertainties are
32 unnecessary and simply confuse the reader with numbers that apparently conflict (e.g. 2.01 vs 2.12) but
33 in reality do not.
34
35
36

37 This is an interesting point from the reviewer.

38
39 First, the 2.01 wt.% is correct. But that is for the calibration data point using a synthetic sample, and
40 not supposed to represent the exact H₂O concentration of the IDDP-1 rhyolite (which is 2.12 wt.%).

41
42 Second, the reviewer is correct that our uncertainty estimates required improvement. What we now do
43 is this: We take the uncertainty on the shift factor (which is relatively large) and we assume that the real
44 answer for the shift factor is given by a normal probability density function spread about the mean c
45 and with the variance given by the uncertainty on c . We then use a Monte Carlo approach to randomly
46 defining a viscosity from the DSC data using a randomly assigned c drawn from that distribution. For
47 each iteration of defining c , we fit the data in Fig. 6. Then, after repeating this one million times, we
48 take the standard deviation on the best-fit H₂O concentrations and assume that this is the error. This
49 results in an IDDP-1 H₂O content and uncertainty of 2.11 ± 0.08 wt. % and a Hrafninnuhryggur H₂O
50 content and uncertainty of 0.12 ± 0.01 wt. %. This is a significant improvement to our manuscript and
51 we thank the reviewer for this comment.
52
53
54
55

56 Page 10 Results section 5d line 32. To "additionally add" seems redundant. Wadsworth et al. (2024) is
57 missing from the reference list.
58

59 We have removed "additionally" and added Wadsworth et al. 2024 to the reference list.
60
61
62
63
64
65

1
2 Page 10 Results section 5d line 32. "Here, all of these results are given as in Wadsworth et al. (2024)
3 on the grounds that the analysis (that locates them in Fig. 6) originates therein". Does this mean that the
4 relaxation and deformation timescales for all of these experiments were calculated (or recalculated) by
5 Wadsworth et al. (2024)? It might be clearer to say it like that. This sentence should refer to Fig 7, not
6 Fig 6.
7

8
9 We have now adopted the suggested change in full.

10
11
12 Page 11 Discussion section 6b lines 57-58. "Iron can play a crucial role in magma rheology". For some
13 balance here, it is worth noting that changes in melt viscosity with variable Fe oxidation state tend to
14 be quite small (e.g. Dingwell 1991; Chevrel et al. 2014 <http://dx.doi.org/10.1016/j.gca.2013.08.026>),
15 especially compared to the effects of temperature and water content.
16

17
18 We have now acknowledged this and the sentence reads:

19
20 **“This direct compositional effect involving the role of iron tends to be small relative to the**
21 **effects of temperature and water (Chevrel et al. 2014). Perhaps more importantly,...”**
22

23
24 We have additionally re-written this section to better describe our thinking on the effect of crystals (see
25 below).
26

27
28 Page 12 Discussion section 6b lines 15-20. This paragraph jumps directly from magnetite nanolite
29 crystallization to crystallinities approaching the maximum packing fraction. For ≤ 3.3 wt% FeOT in the
30 melt, it would be impossible to crystallize more than ~ 2 vol.% magnetite (given its high density of
31 ~ 5500 kg/m³). Even though nanolites do appear to have a disproportionately large effect on viscosity,
32 they are still not going to approach anywhere near to the maximum packing fraction, or even 40
33 vol.%. There should be a citation for the statement that 40% crystals produces a 1 log unit viscosity
34 increase, and a suitable one would be Mader et al. (2013), cited in the introduction.
35

36
37 We now cite Mader et al. (2013) as suggested. We have additionally rewritten this section almost in full
38 with an aim to address these points about volume fractions from the reviewer. In short: we agree. The
39 new section is copied here (a lot has changed but we have put in bold the bits relevant to the reviewer's
40 points):
41

42
43 The viscosity of silicate magma is influenced by both melt chemistry and the presence of
44 crystals. In the case of Krafla, the rhyolitic magma contains a high concentration of iron. In
45 **Fig. 9** we report the average glass total iron FeO_T as a function of the silica SiO₂ as compared
46 with rhyolite glasses worldwide using a published database (Di Genova et al. 2017). This shows
47 that the Hrafninnuhryggur obsidian and IDDP-1 glass are among the most iron-rich natural
48 rhyolitic glasses known (Wadsworth et al. 2021a).
49

50
51 Iron can play a role in magma rheology due to changes in oxidation state, which impacts the
52 configuration and role of iron in the melt structure (Dingwell 1991). Additionally, iron can
53 promote crystallization include the formation of iron-rich nanolites (Mujin et al. 2017; Di
54 Genova et al. 2018, 2020; Cáceres et al. 2020, 2021, 2024; Pereira et al. 2024). Interestingly,
55 the precipitation of iron-rich nanolites can have a knock-on effect on the melt viscosity which
56 can, in some cases, be substantial (Zandonà et al. 2023; Cáceres et al. 2024; Pereira et al. 2024).
57 **Having said that, the volume fractions of nanolites tend to be small, reducing their**
58 **expected effect on the bulk magma viscosity (Mader et al. 2013; Vasseur et al. 2023) and**
59 **the direct compositional effects involving the role of iron tends to be small relative to the**
60 **effects of temperature and water (Chevrel et al. 2014).**
61
62
63
64
65

1 The formation and growth of Fe-oxide crystals in Krafla rhyolite can result from oxidation of
2 the melt (Cáceres et al. 2021). Contrastingly, Castro et al. (2009) showed that the formation of
3 Fe-oxide crystals and can reduce the melt in an oxidation state buffered crystallization step
4 associated with H₂O movement. Casas et al. (2019) used titration methods to determine the iron
5 oxidation ratio in the Hrafninnuhryggur glass as-collected, and found that the ratio of Fe³⁺ to
6 total Fe, termed Fe_T, was Fe³⁺/Fe_T = 0.167, similar to the ‘clear glass’ in the spherulite-
7 bearing samples (Fe³⁺/Fe_T = 0.165 ± 0.04) reported by Castro et al. (2009). Other than these
8 sparse measurements, the oxygen fugacity for each rhyolite body at Krafla is poorly constrained
9 and so this effect of iron on melt structure and rheology should be investigated further in future.

10
11
12 Our deformation map (**Fig. 7**) suggests that this growth of any crystals will strongly affect the
13 viscoelastic properties if the crystallization reaches high volume fractions relative to a
14 ‘maximum packing’ volume fraction (Wadsworth et al. 2024). For example, if crystallinities
15 were to reach ≈ 40 vol. %, then the viscosity would increase by one log unit (**Mader et al.**
16 **2013**). **Clearly, iron-bearing nanolites cannot crystallize to such high volume fraction.**
17 **However, if the rhyolite is stored hot for sufficient time for further crystallization, or if**
18 **another rhyolite which has crystallized is intersected by drilling at Krafla , then our**
19 **deformation map can be used to constrain the rheology (Fig. 7).**
20
21
22
23

24 Page 12 Discussion section 6b lines 26-28. Excellent point about future work needed to explore
25 "interactions with drilling fluids and/or drilling-induced decompression and cooling". This is
26 worth building on here, to the extent possible. Is there any literature on the effects of drilling on the P-
27 T path of the rock being drilled? Even a qualitative vector in P-T space would be helpful. If the drill hole
28 was under-pressured relative to the surrounding rock, the hole would probably close up quite quickly,
29 so presumably decompression occurs mostly on ascent of cuttings towards the surface. Likewise, what
30 are the typical strain rates associated with drilling? At what ranges of temperature and water content
31 would the drill just stir the lava? The petroleum engineering literature may be a good place to start.
32
33

34 While attending a recent meeting about the KMT project, it became clear that there simply is not enough
35 literature on this subject to provide the answers that the reviewer wants here. The P-T conditions,
36 saturation, and time-dependence of materials involved is in stark contrast to other drilling scenarios.
37 We completely agree with the reviewer that this topic must be explored, but it is beyond the scope of
38 our study. It is currently being tackled by novel experiments and numerical simulations, which will be
39 subject of upcoming studies.
40
41
42
43
44
45
46
47
48
49
50
51
52
53
54
55
56
57
58
59
60
61
62
63
64
65

Reviewer 2

1
2 This paper provides the rheology of rhyolite magma with various water content, motivated by the risk
3 mitigation for the KMT project. The authors performed a thermal analysis of the IDDP-1 sample and
4 estimated its viscosity using the previously known viscosity model, calibrating it
5 with Hrafninnuhryggur obsidian, whose water content differs from IDDP-1. In contrast, the
6 title/abstract/closing remarks make an impression that the authors have a sequence of samples from the
7 storage to the surface, and their results are deeply connected with geothermal drilling. This mismatch
8 between the impression and content of what was researched should be corrected. I also recognize that
9 this paper does not refer to the recent updates of the works on rhyolite rheology. I thus consider that
10 substantial revision is required. I describe the details below.
11
12

13 We have now revisited the title to avoid ambiguity. The title is now simply:
14

The rheology of rhyolite magma from the IDDP-1 borehole and Hrafninnuhryggur (Krafla, Iceland) with implications for geothermal drilling

15
16
17
18

19 Additionally, we now cite and acknowledge more recent ‘updates’ to rhyolite rheology. These are
20 detailed below in responses to other questions/comments from this reviewer.
21
22

23 Title: The title of this paper suggests that it aims to provide the depth-dependent rheology of rhyolite
24 magma. However, as the authors wrote, "While these rhyolites are not thought to be genetically linked,
25 they have similar compositions." The relation between the Hrafninnuhryggur obsidian and the IDDP-
26 1 is not clear. According to Fig.1, the location between the IDDP-1 well and Hrafninnuhryggur is quite
27 far. This work can be interpreted as a rheology estimate of rhyolites with various water content. Also,
28 this paper does not discuss the implications of geothermal drilling. Therefore, I believe the phrases in
29 the title "from storage to the surface" and "with implications for geothermal drilling" are inappropriate.
30 A clear and accurate title is crucial to represent the research effectively.
31
32

33 We have now changed the title (see previous comment). We discuss implications for geothermal drilling
34 and so we conclude that the part of the title that mentions implications for geothermal drilling is
35 appropriate and as such we retain that portion.
36
37

38 In Fig. 1, both Hrafninnuhryggur and IDDP-1 are given as location points.
39
40

41 - The drilling of IDDP-1 was intercepted by rhyolitic magma. This episode itself evidences that drilling
42 hot magma does not cause catastrophe. So, I wonder whether measuring the rheology of this magma
43 helps hazard assessment and risk mitigation for the KMT project.
44
45

46 The drilling of IDDP1 did not lead to catastrophe. But future KMT drilling efforts may not (and surely
47 will not) be identical to the IDDP1 attempt. The drill and borehole designs will all necessarily be
48 different. Therefore, the fundamental question remains: what is the rheology of the magma at depth and
49 how will magma respond to drilling? Similarly, it is important beyond KMT to generally understand
50 the response of rhyolite to drilling and decompression. We now expand on this in the discussion section
51 (which also further discussed the implications for geothermal drilling; see previous comment).
52
53

**In this model, magma fragmentation is vigorous and occurs at depth, producing
pyroclasts that are transported up the conduit where a fraction of the pyroclasts are
‘captured’ at shallow depths and weld to the conduit walls. Those welded deposits are
then advected out of the vent as lava. This is pertinent to the drilling scenarios because it
suggests that the Krafla rhyolites can readily fragment in vigorous explosive eruptions
when subjected to a decompression (Rooyackers et al. 2020).**

54
55
56
57
58
59
60
61
62
63
64
65

and

We highlight here these different models for rhyolite ascent in the crust on the assumption that future drilling into magma has some conceptual similarities to opening up a conduit to the Earth's surface. For this reason, the general behaviour of rhyolite upon decompression and ascent to the surface requires understanding.

- The importance of nanolite and rheology of nanolite-bearing magma are also reported by these papers. Mujin, M., and M. Nakamura; A nanolite record of eruption style transition. *Geology* 2014;; 42 (7): 611-614. doi: <https://doi.org/10.1130/G35553.1>. Okumura, S., Uesugi, K., Goto, A. et al. Rheology of nanocrystal-bearing andesite magma and its roles in explosive volcanism. *Commun Earth Environ* 3, 241 (2022). <https://doi.org/10.1038/s43247-022-00573-9>

We now cite both of those papers and thank the reviewer for pointing us to them.

- The authors use "high-enthalpy supercritical fluids," but it is unclear why they describe it as "high-enthalpy." An explanation is needed.

We now have removed 'high enthalpy'. Although we note that this term is used in the geothermal energy literature to denote higher-than-currently-common energy fluids.

- Wadsworth et al. (2024) is not listed in the reference. - The authors discuss fragmentation using Wi . However, recent papers show that the condition for fragmentation is not determined solely by Wi . The relaxation time scale is also complex. Including recent updates makes the discussion more meaningful. Namiki, A., Okumura, S., Goto, A. et al. In situ observation of glass-like fragmentation of high-temperature silicate melts generating fine ashes. *Commun Earth Environ* 4, 155 (2023). <https://doi.org/10.1038/s43247-023-00816-3>

Wadsworth et al. (2024) is now included.

We now cite this paper from Namiki et al. (2023). We additionally include a discussion of their findings in our paper as suggested and as follows:

The deformation map presented in Fig. 7 can be used to understand the conditions of strain rate required for failure to occur. However, the deformation map presupposes that the strains will be large (Wadsworth et al. 2018). It takes a finite time for the failure to onset and this time is not accounted for simply by the deformation map scaling given here. Instead, to find the time for failure we use Maxwell's viscoelasticity which states

$$\sigma + \frac{\mu}{G} \frac{d\sigma}{dt} = \mu \dot{\epsilon} \quad \text{Eq. 7}$$

where σ is the shear stress in the melt. If $\dot{\epsilon}$ is constant, as is the case in our experiments, and if $\sigma = 0$ at $t = 0$, then Eq. 7 leads to a prediction of $\sigma(t)$ as

$$\sigma(t) = \mu \dot{\epsilon} \left[1 - \exp\left(-\frac{tG}{\mu}\right) \right] \quad \text{Eq. 8}$$

Our experimental finding that failure occurs for $Wi \geq 0.04$ is akin to finding that the critical stress for failure is $\sigma_c = 0.04G \approx 4 \times 10^8$ Pa. Eq. 8 can then be used to find the critical time t_c it takes for σ to reach σ_c as

1
$$t_c = -\frac{\mu}{G} \ln\left(1 - \frac{\sigma_c}{\mu\dot{\epsilon}}\right) \quad \text{Eq. 9}$$

2
3
4 or, as a finite strain required for failure ϵ_c

5
6
$$\epsilon_c = -Wi \ln\left(1 - \frac{\sigma_c}{\mu\dot{\epsilon}}\right) \quad \text{Eq. 10}$$

7
8
9
10 **Eqs 9-10 then acknowledge that there can be viscous deformation occurring for a finite**
11 **time (or strain) prior to viscoelastic rupture, which has been confirmed experimentally**
12 **(Dingwell and Webb 1989; Cordonnier et al. 2012c; Wadsworth et al. 2018; Namiki et al.**
13 **2023).**

14
15 We note that by adding the above analysis, we have acknowledged that Namiki et al. (2023)'s result is
16 not really an 'update' to rhyolite rheology, but is simply highlighting the time-to-failure that is implicit
17 in Maxwell's rheology. We are grateful for the opportunity to include this addition.

18
19
20
21 - In the last paragraph, the authors mention the importance of cooling. Indeed, low-temperature magma
22 easily fragments. Possible temperature changes should be estimated. - Namiki, A., Tanaka, Y.,
23 Okumura, S., et al., Fragility and an extremely low shear modulus of high porosity silicic magma,
24 Journal of Volcanology and Geothermal Research, Volume 392,
25 2020, <https://doi.org/10.1016/j.jvolgeores.2019.106760>.

26
27 We have no way to estimate possible temperature changes during drilling or during eruption. This is
28 discussed in the manuscript. It is a real target for future work to understand this better. Unfortunately,
29 the temperature evolution near the drill bit is not reliable for reasons that are discussed elsewhere.

30
31
32
33 - Whether the gas escape occurs from the fracture surface is debated. Sano et al. (2015) suggest the
34 ductile deformation rather than brittle fracture. On the fragmented surface of the conduit, the magma
35 will heal, and the pathway will close. Yoshimura, S., and M. Nakamura (2010), Fracture healing in a
36 magma: An experimental approach and implications for volcanic seismicity and degassing, J. Geophys.
37 Res., 115, B09209, doi:10.1029/2009JB000834.

38
39 We now cite Sano et al. (2015) and the Yoshimura & Nakamura (2010) papers in our discussion of
40 fracture dynamics.

41
42
43
44 Fig.1: Please denote the details (lava and feeder dykes) of Hrafninnuhryggur obsidian. Readers are not
45 specialists in this area. The legend for rhyolites classified by years does not help.

46
47 We now provide a new Figure 1 which has an additional new panel associated with Hrafninnuhryggur
48 outcrops and labels the lava and the feeder dyke outcrops. This figure is pasted below for the editor's
49 convenience.
50
51
52
53
54
55
56
57
58
59
60
61
62
63
64
65

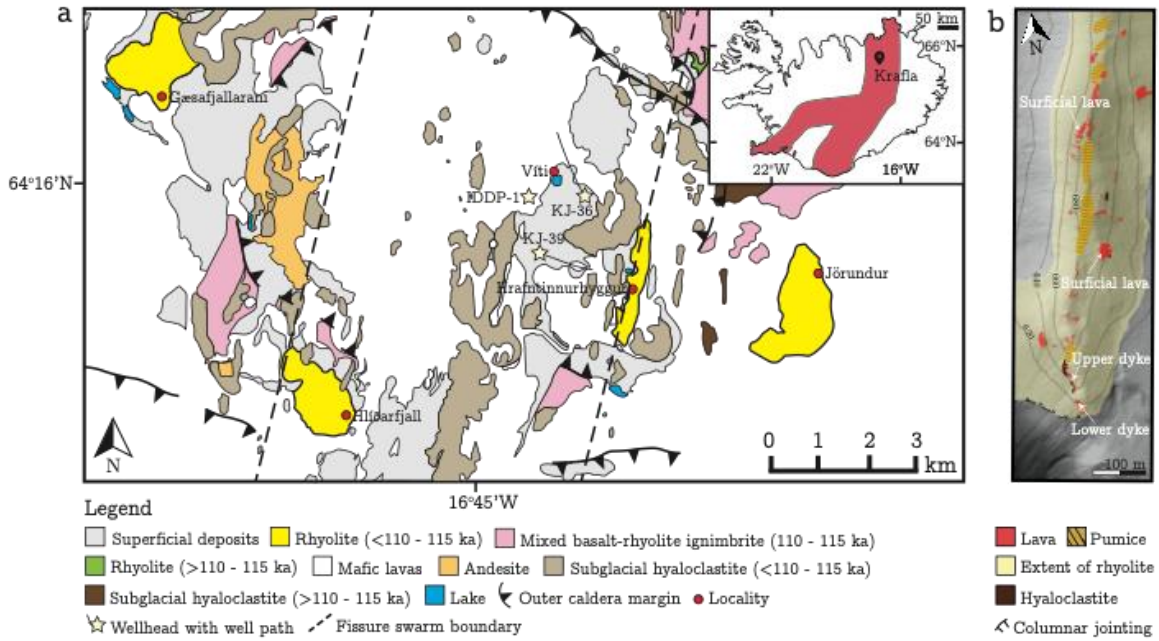


Fig.2: The low resolution makes it hard to recognize the marker color.

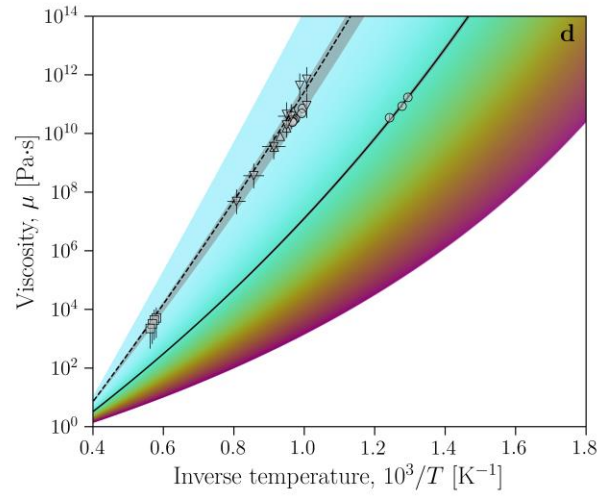
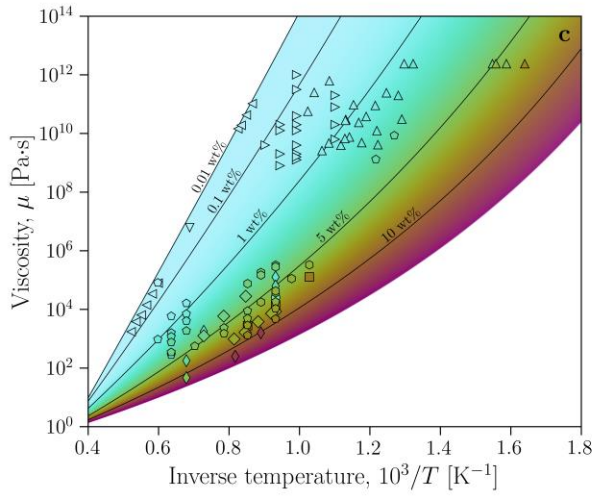
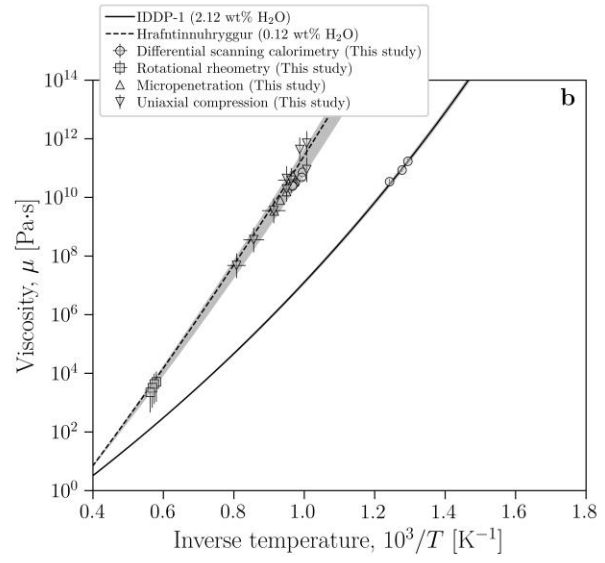
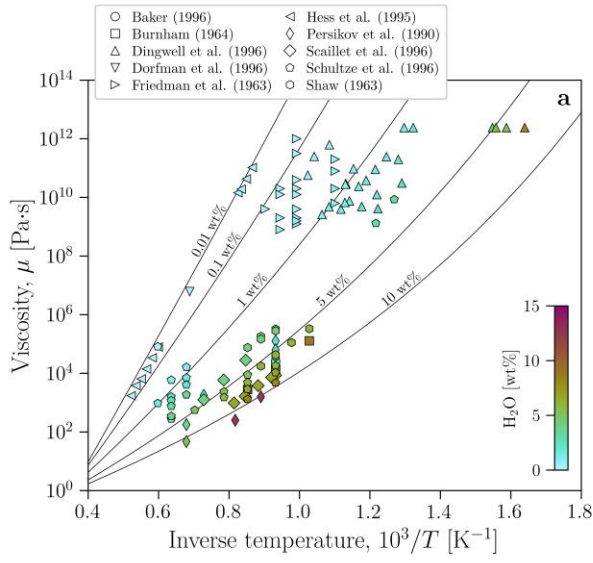
This is only low resolution in the submission package. It is high resolution in reality.

Fig.5: I would like to request that T' be added to this figure.

We are unable to add T' to this figure without confusing any reader who is unfamiliar with fictive temperatures and associated concepts. Given that our manuscript is not a dedicated study of the fictive temperature, and given that we simply apply models for the fictive temperature to our data, we opt not to add this.

Fig.6a: The markers are scattered, and the water content is not denoted for each group, so it is not obvious how this figure should be interpreted. Fig.6b: I infer that the authors use this diagram to show that viscosity can be measured by thermal analysis. In that case, the magma with the same water content as IDDP-1 should be used. The color difference between IDDP-1 and Hrafninnuhryggur obsidian is hard to tell.

We take this point on board and as a result we have re-jigged the entire figure to make it better understandable. The new figure is copied below. We hope that we have therefore addressed these points, as well as the points from the first reviewer on this same figure.

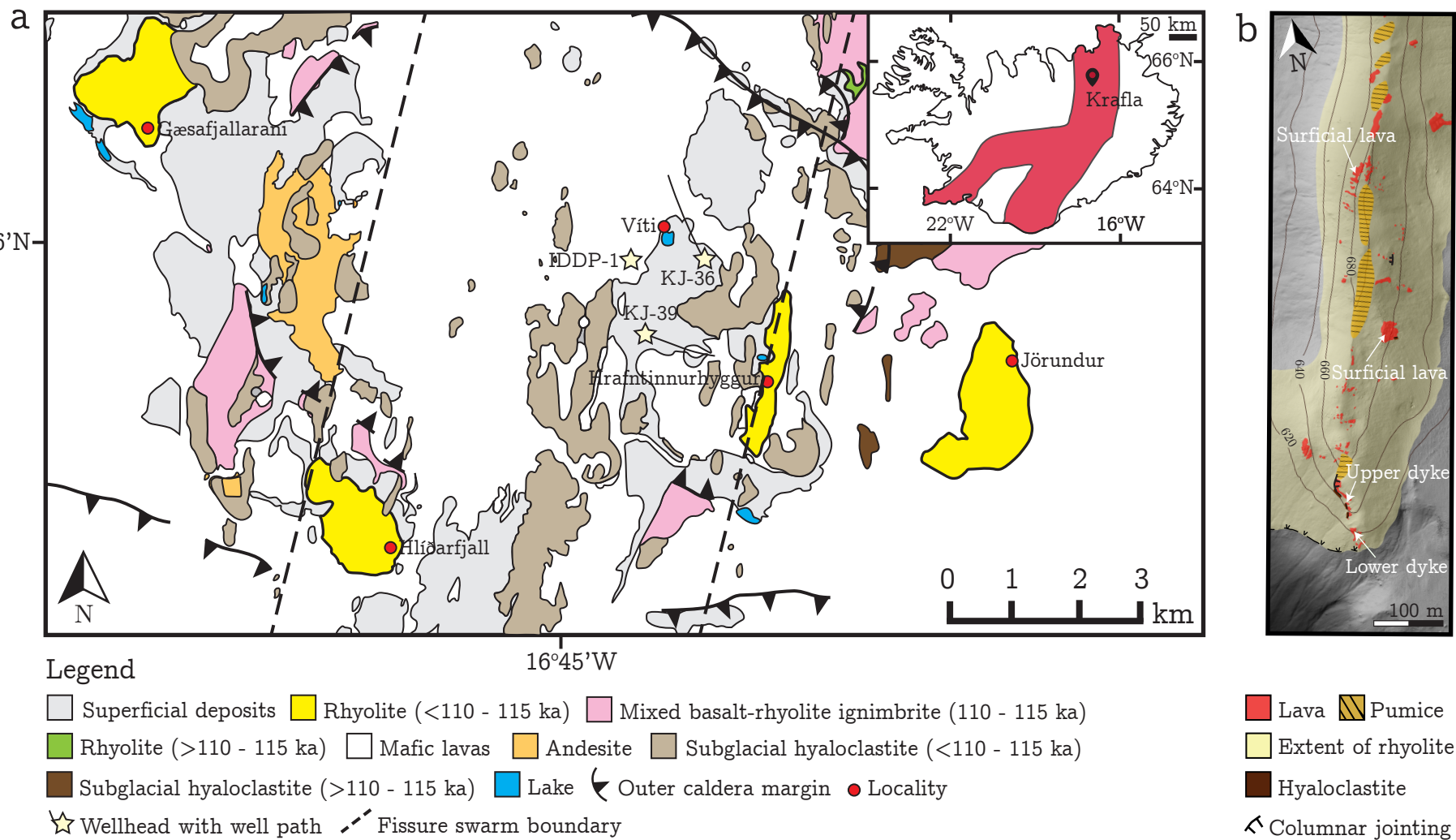


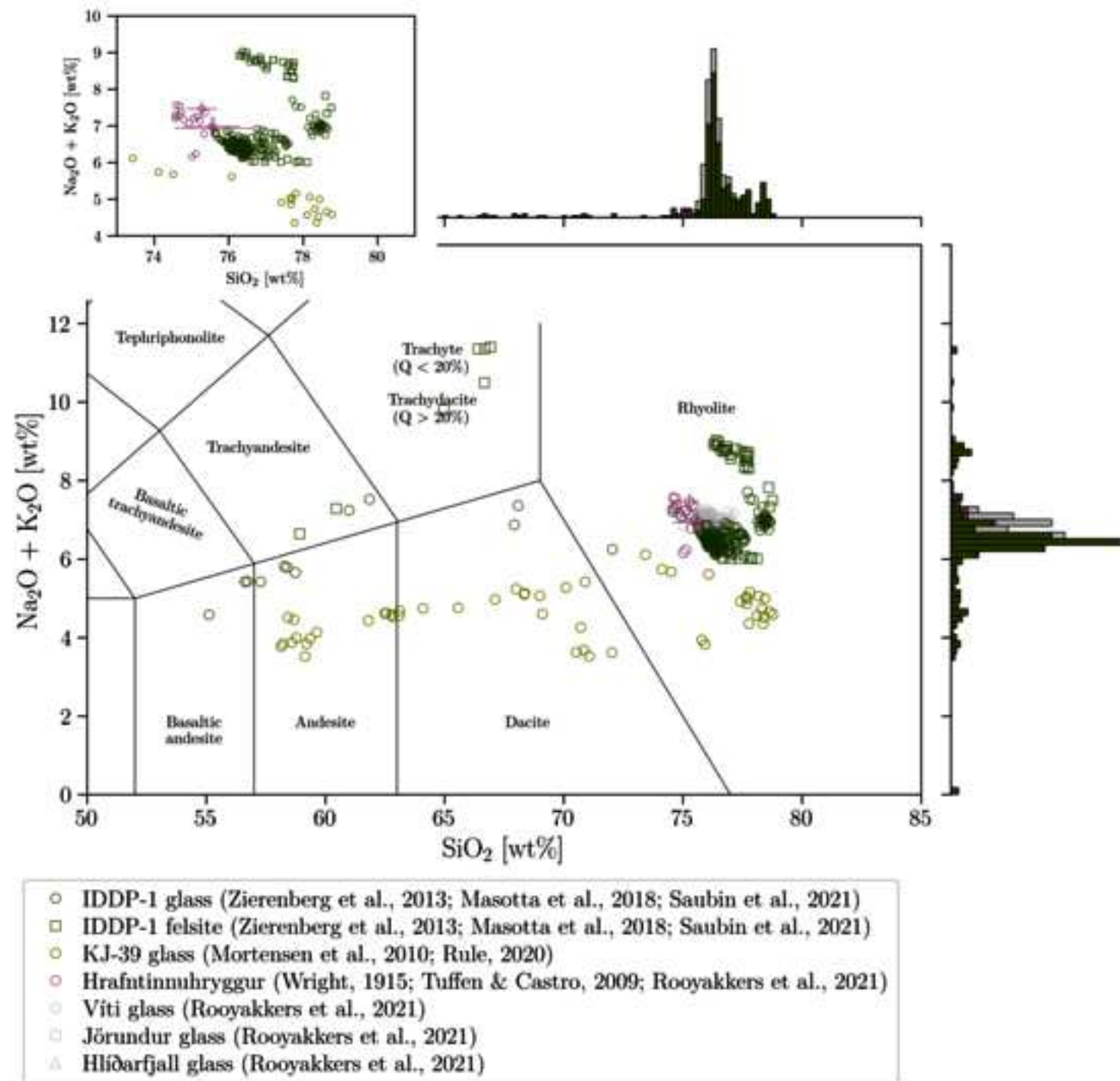
1
2
3
4
5
6
7
8
9
10
11
12
13
14
15
16
17
18
19
20
21
22
23
24
25
26
27
28
29
30
31
32
33
34
35
36
37
38
39
40
41
42
43
44
45
46
47
48
49
50
51
52
53
54
55
56
57
58
59
60
61
62
63
64
65

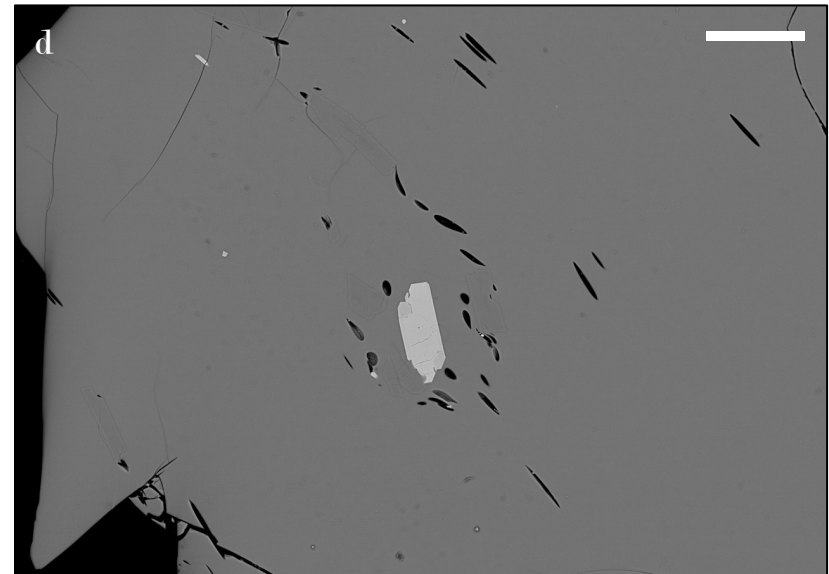
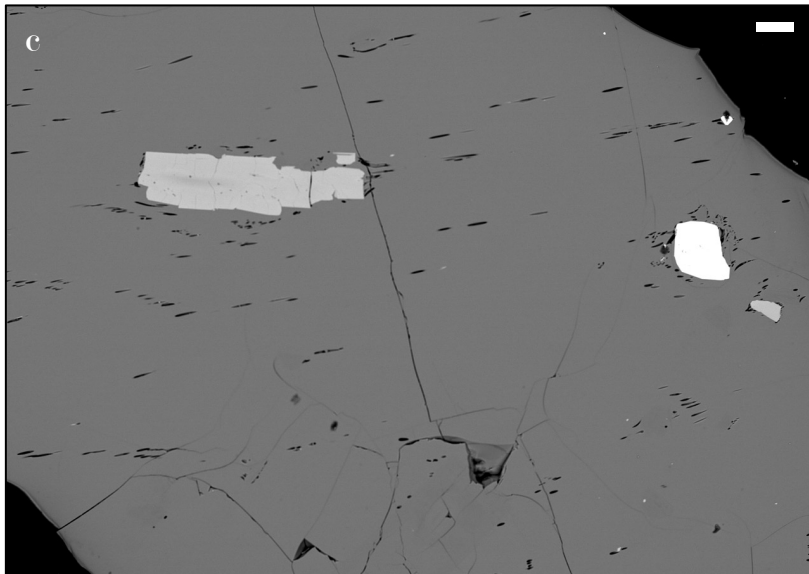
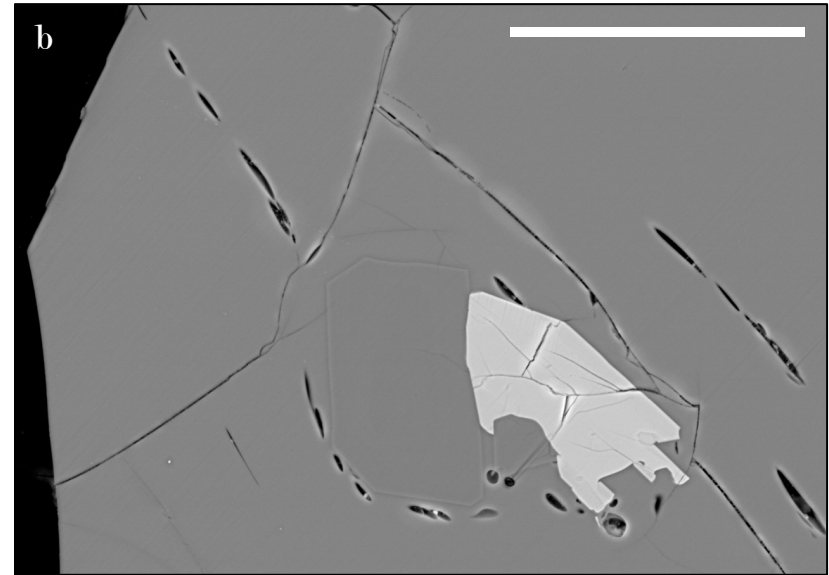
Highlights

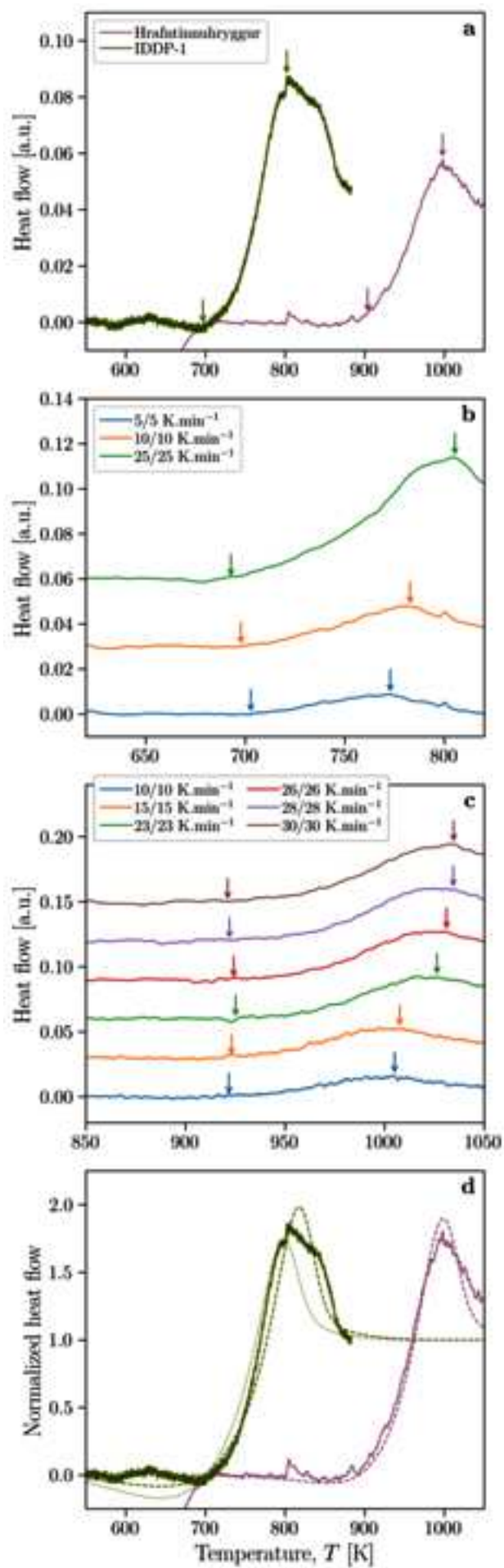
- A model is presented for the Krafla rhyolite H₂O- and temperature-dependent rheology.
- The Krafla rhyolites are viscoelastic and will respond in a brittle manner at high strain rates.
- Magma rheology models are crucial for future drilling goals at Krafla volcano.

Figure 1

[Click here to access/download;Figure;Figure_1.pdf](#)







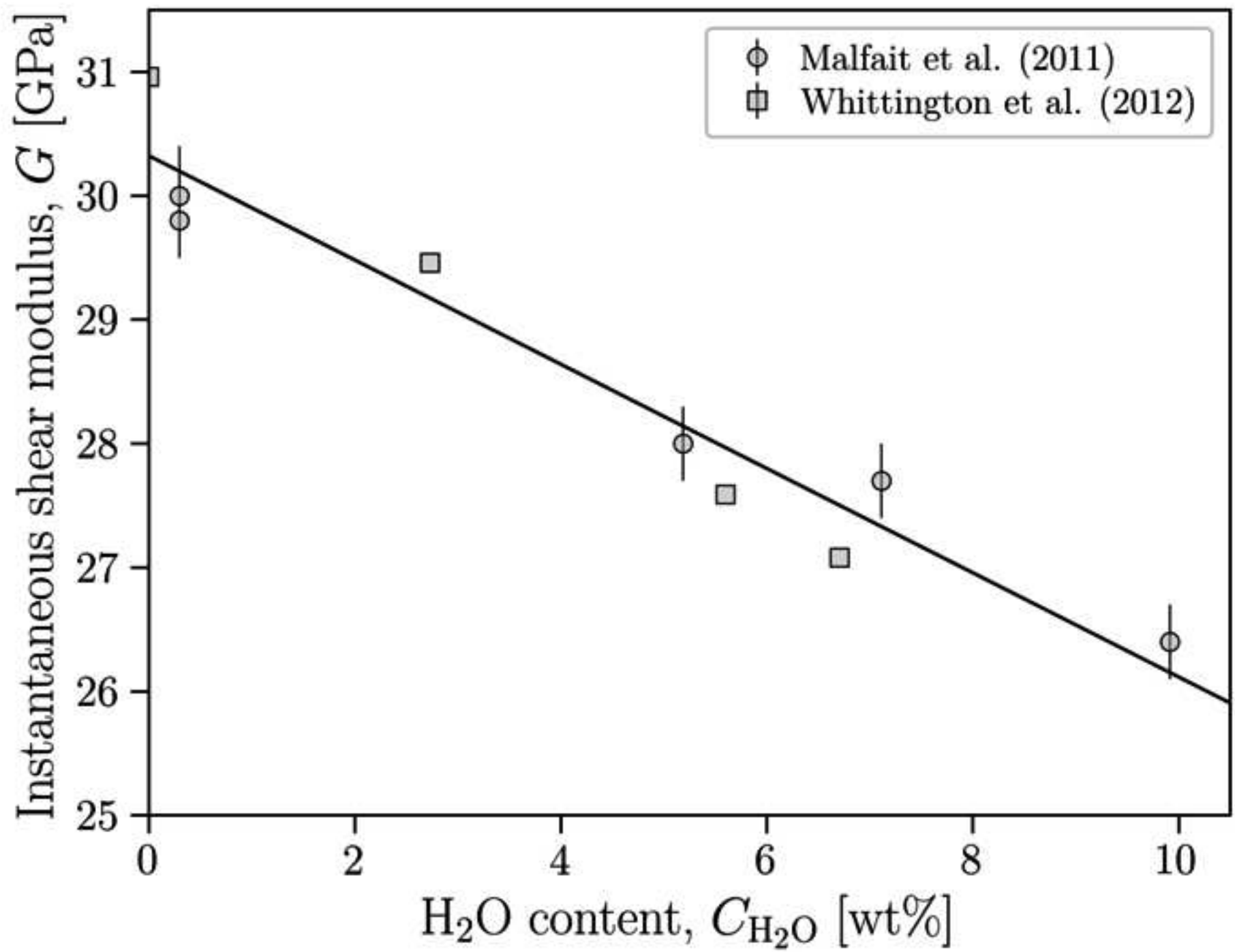
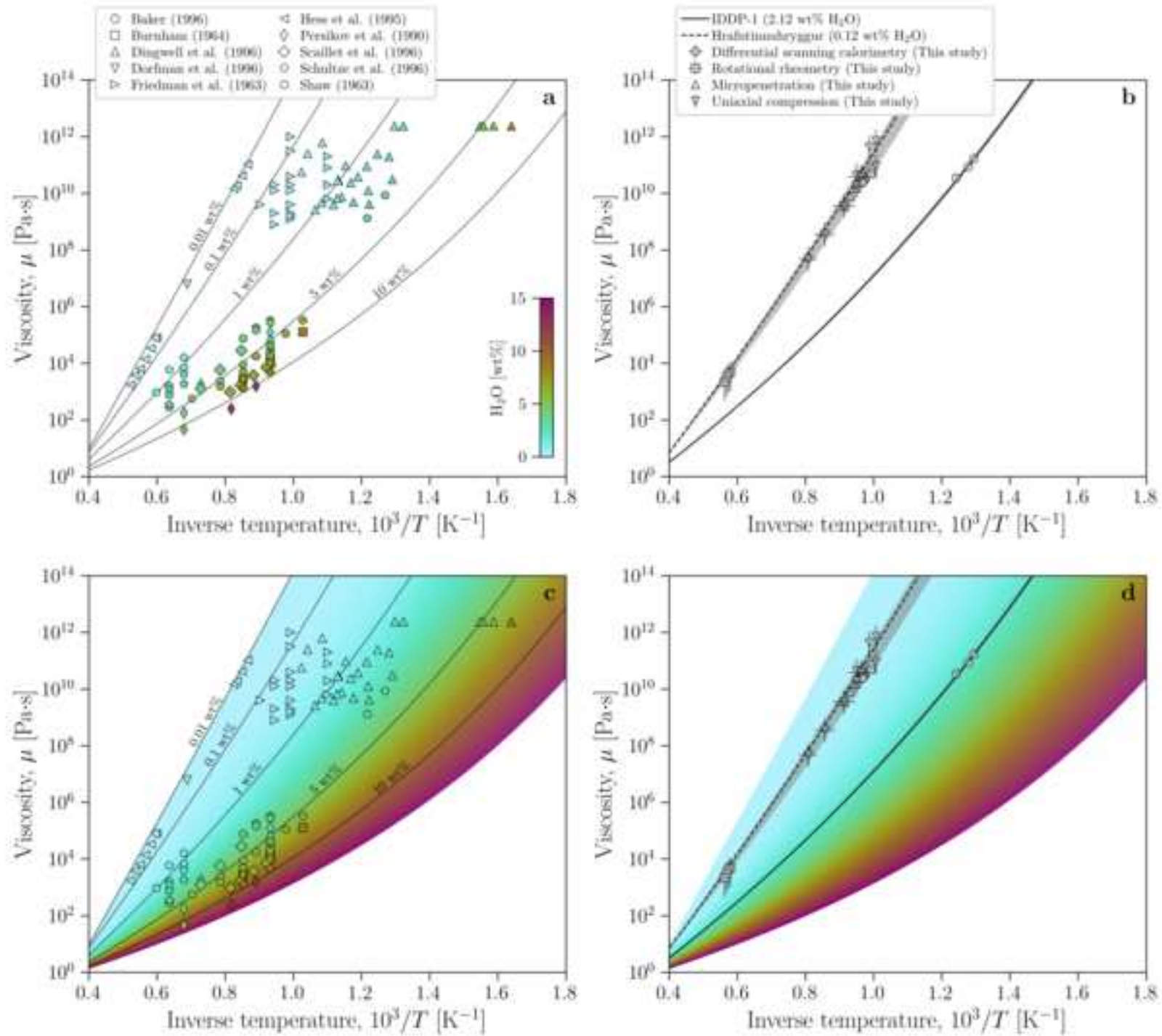
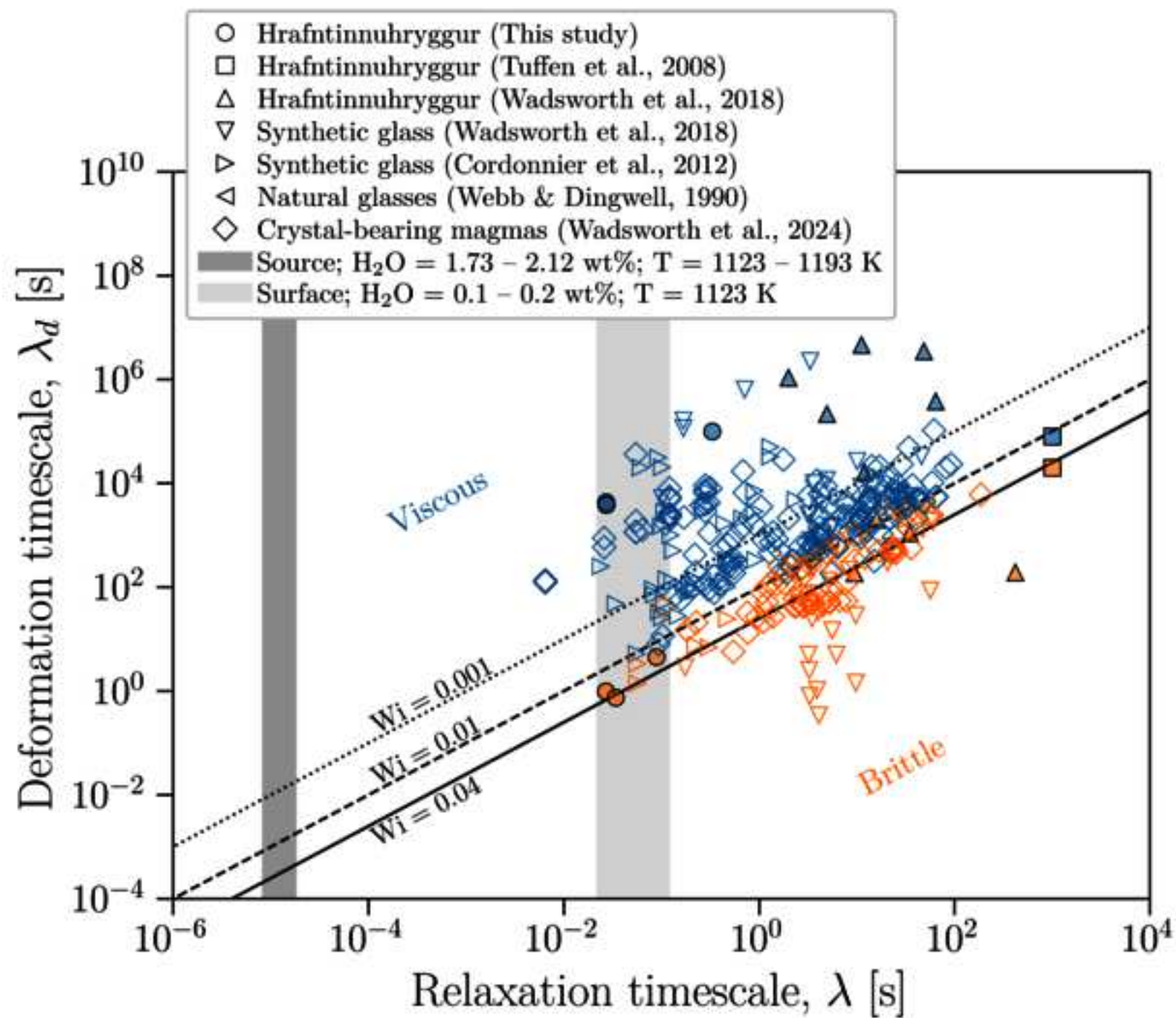
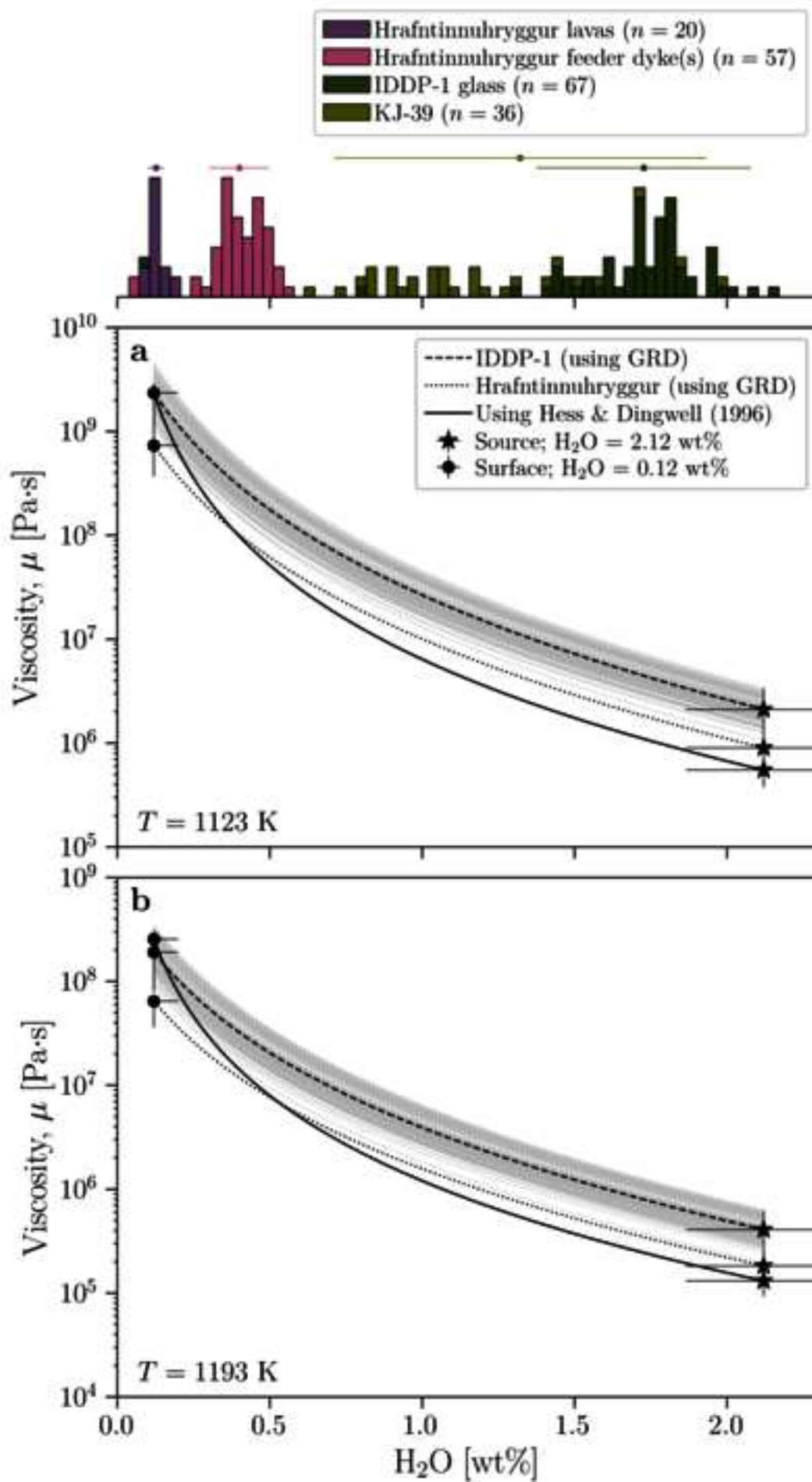
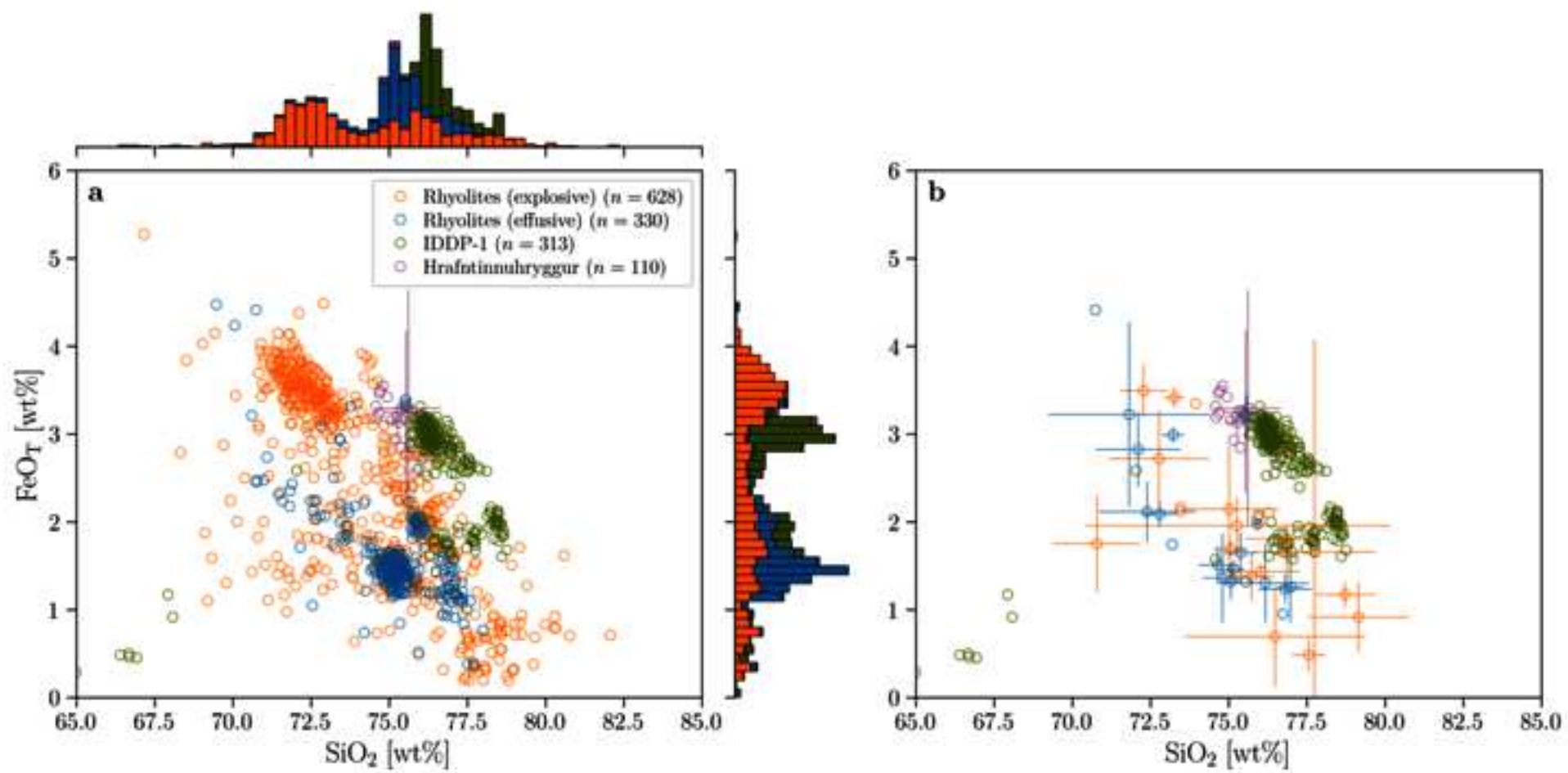


Figure 6

[Click here to access/download;Figure;figure_6_new.png](#)







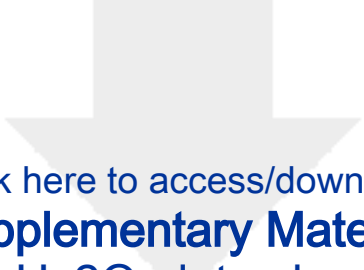
Declaration of interests

The authors declare that they have no known competing financial interests or personal relationships that could have appeared to influence the work reported in this paper.

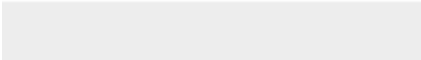

The authors declare the following financial interests/personal relationships which may be considered as potential competing interests:

Author statement

Fabian B. Wadsworth: conceptualization, methodology, formal analysis, visualization, writing-original draft. **J r mie Vasseur:** formal analysis, visualization. **Yan Lavall e:** conceptualization, funding acquisition, writing- review and editing. **Kai-Uwe Hess:** formal analysis, writing- review and editing. **Jackie E. Kendrick:** conceptualization, writing- review and editing. **Jonathan M. Castro:** formal analysis, visualization, writing- review and editing. **Daniel Weidendorfer:** formal analysis, writing- review and editing. **Shane M. Rooyakkers:** writing- review and editing. **Annabelle Foster:** visualization, writing- review and editing. **Lucy E. Jackson:** writing- review and editing. **Ben M. Kennedy:** writing- review and editing. **Alexander R. L. Nichols:** formal analysis, writing- review and editing. **C. Ian Schipper:** writing- review and editing. **Bettina Scheu:** funding acquisition, writing- review and editing. **Donald B. Dingwell:** funding acquisition, conceptualization, writing- review and editing. **Tamiko Watson:** formal analysis. **Georgina Rule:** formal analysis. **Taylor Witcher:** formal analysis. **Hugh Tuffen:** writing- review and editing.



Click here to access/download
Supplementary Material
H_2O_data.xlsx



The rheology of rhyolite magma from the IDDP-1 borehole and Hrafninnuhryggur (Krafla, Iceland) with implications for geothermal drilling

Fabian B. Wadsworth¹, Jérémie Vasseur², Yan Lavallée², Kai-Uwe Hess², Jackie E. Kendrick², Jonathan M. Castro³, Daniel Weidendorfer², Shane M. Rooyakkers⁴, Annabelle Foster¹, Lucy E. Jackson¹, Ben M. Kennedy⁵, Alexander R. L. Nichols⁵, C. Ian Schipper⁶, Bettina Scheu², Donald B. Dingwell², Tamiko Watson⁵, Georgina Rule⁵, Taylor Witcher⁷, Hugh Tuffen⁸

¹Department of Earth Sciences, Durham University, DH1 3LE, U.K.

²Earth and Environmental Sciences, Ludwig-Maximilians-Universität, 80333 Munich, Germany.

³Institute of Geosciences, Johannes Gutenberg University, Mainz, Germany.

⁴GNS Science, Lower Hutt 5011, New Zealand, Aotearoa.

⁵School of Earth and Environment, Te Kura Aronukurangi, University of Canterbury, Te Whare Wānanga o Waitaha, Private Bag 4800, Christchurch, Ōtautahi, 8140, New Zealand, Aotearoa.

⁶School of Geography, Environment, and Earth Sciences, Te Herenga Waka, Victoria University of Wellington, PO Box 600, Wellington, 6140 New Zealand, Aotearoa.

⁷Department of Earth Sciences, Uppsala University, Villavägen 16 75236 Uppsala, Sweden

⁸Lancaster Environment Centre, Lancaster University, Lancaster, United Kingdom.

Orcid IDs

Fabian B. Wadsworth	0000-0002-5341-208X
Jérémie Vasseur	0000-0002-0783-5065
Yan Lavallée	0000-0003-4766-5758
Kai-Uwe Hess	0000-0003-1860-8543
Jackie E. Kendrick	0000-0001-5106-3587
Jonathan M. Castro	0000-0003-4865-1737
Daniel Weidendorfer	0000-0002-6118-9287
Annabelle Foster	0000-0002-1578-5328
Lucy E. Jackson	0000-0002-5047-5982
Ben M. Kennedy	0000-0001-7235-6493
Alexander R. L. Nichols	0000-0002-8298-2882
C. Ian Schipper	0000-0002-9064-3370
Bettina Scheu	0000-0002-0478-1049
Donald B. Dingwell	0000-0002-3332-789X
Shane M. Rooyakkers	0000-0001-6876-0995
Tamiko Watson	
Georgina Rule	
Taylor Witcher	0000-0002-4326-3607
Hugh Tuffen	0000-0001-8829-1751

Changes in rhyolite melt viscosity during magma decompression and degassing exert a first order control on ascent through the crust and volcanic eruption style. These changes have as yet unknown hazard implications for geothermal drilling in pursuit of particularly hot fluids close to magma storage regions. Here, we exploit the situation at Krafla volcano in which rhyolite has both erupted at Earth's surface and been sampled at shallow storage depths via drilling of the 2009 IDDP-1 and 2008 KJ-39 boreholes. We use differential scanning calorimetry to constrain that the IDDP-1 magma quenched to glass at ~700 K, at a rate of between 7 and 80 K.min⁻¹. We measure the equilibrium viscosity of the IDDP-1 rhyolite at temperatures close to the glass transition interval and show that the rhyolite viscosity is consistent with generalized viscosity models assuming a dissolved H₂O concentration of 2.12 wt.%. We couple these results with micro-penetration and concentric cylinder rheometry over a range of potential magma storage temperatures to constrain the response of surficial Krafla rhyolites to stress. The surficial rhyolites at Krafla match the same viscosity model, assuming a lower dissolved H₂O concentration of 0.12 wt.%. Our results show that at a storage temperature of 1123-1193 K, the viscosity of the stored magma is $\sim 3 \times 10^5$ Pa. s. At the same temperature, the viscosity following degassing during ascent to the surface rises to $\sim 2 \times 10^9$ Pa. s. Finally, we use high-stress compression tests on the Hrafninnuhryggur surface obsidian to determine the onset of unrelaxed behavior and viscoelastic melt rupture or fragmentation pertinent to understanding the melt response to rapid pressure changes that may be associated with further (near-) magma exploration at Krafla. Taken together, we characterize the relaxation and viscosity of these magmas from source-to-surface.

viscosity; silicic eruption; obsidian; magma; volcanic eruption; rhyolite; relaxation

1. Introduction

The rheology of magmatic liquids exerts a first order control on whether or not a volcanic eruption will be explosive (e.g., Cassidy et al. 2018). Part of the challenge for Earth scientists is to decipher the ways in which rheology evolves during magma ascent through the crust. Physical and chemical processes such as bubble growth (Sparks 1978; Blower et al. 2001; Coumans et al. 2020), crystallization (e.g. La Spina et al., 2021), flash nanolitisation (Di Genova et al. 2020; Cáceres et al. 2020; Pereira et al. 2024), and temperature changes due to cooling (including latent heat effects; Blundy et al. 2006), viscous dissipation as heat, or friction (Mastin 2005; Petcovic and Dufek 2005; Costa et al. 2007; Lavallée et al. 2015a; Kendrick and Lavallée 2022), all lead to rheological changes in the melt phase and feedback with the variable development of multiphase suspension rheology (Mader et al. 2013). A standard approach to understanding melt rheology has been to determine the equilibrium viscosity of melts in the laboratory at relevant magmatic conditions and to use these measurements to calibrate empirical model fits. This approach is underpinned by the range of conditions over which the rheological determinations have now been made, encompassing much of the breadth of temperature and dissolved volatile concentrations extant in magmas in the upper crust (Hess and Dingwell 1996; Giordano et al. 2008), and exemplified by the low relative residuals between experimental observations and models. However, in most cases, only volcanic deposits at the Earth's surface are directly accessible, and so there remains a degree of uncertainty in the application of these constitutive rheological models to magma transport and eruption.

Drilling projects such as the Iceland Deep Drilling Project (IDDP) afford an opportunity to access and sample the sub-surface directly. The IDDP-1 borehole was drilled approximately vertically in 2009 at Krafla volcano and was designed to reach 4–5 km below the surface in pursuit of supercritical fluids associated with magmatic intrusions. However, at 2.1 km depth, the drill intercepted rhyolitic magma, evidenced by the appearance of quenched silicic glass chips in the drill cuttings (Friðleifsson et al. 2010; Elders et al. 2011). The borehole assembly was pushed upward for 4 minutes, before the melt was fully quenched by drilling fluid, and became stuck (Friðleifsson et al. 2010; Pálsson et al. 2014). This interception of rhyolitic melt and direct sampling of quenched silicic glass from depth provides a unique opportunity to study a shallow rhyolitic magma *in situ* (Eichelberger 2019; Saubin et al. 2021), as well

as demonstrating the production potential associated with high-temperature fluids (Ingason et al. 2014). Importantly, there are surface effusive rhyolites exposed within ~2 km of the IDDP-1 drill site (**Fig. 1**) at Krafla (Jónasson 1994; Tuffen and Castro 2009; Rooyakkers et al. 2021b), offering a chance to study compositionally similar rhyolites in both a pre- and post-eruptive state.

Prior to the well-known IDDP-1 borehole, the KJ-39 borehole was drilled in 2008, south of the Leibortnar-Vítismór field and ~2.5 km south of IDDP-1 (**Fig. 1**). This was drilled directionally to the east at an angle of 30° from vertical with the same aim as IDDP-1: to access supercritical fluids for geothermal purposes. The drill string reached a maximum down-hole distance of 2.865 km where it was stuck and, after being freed using explosives, the bottom hole assembly was found to contain drill cuttings including quenched silicic glass. This, together with the high down-hole temperatures in excess of the local geotherm, the silicic glass suggested that the hole had intersected magma (Mortensen et al. 2010; Rule 2020). Therefore, there are two candidate case studies of deep silicic glass extraction from shallow storage regions at Krafla volcano: KJ-39 and IDDP-1.

Here, motivated by the need to better understand magma properties and potential response to future (in-situ/near-) magma drilling efforts, such as envisaged in the Krafla Magma Testbed (KMT: see <https://www.kmt.is/>; Eichelberger, 2019; Lavallée et al. *in review*), we constrain the rheology of silicic magmatic liquids in a case-study location where both the stored magma and an erupted equivalent of the same rhyolitic magma can be studied in tandem. These rheological data will inform on-going and future efforts aiming at modelling the potential response of magma to drilling, thus supporting implementation plans and risk mitigation strategies for such endeavors.

2. Materials: Hrafninnuhryggur and IDDP-1

We use rhyolitic glass from two neighboring sites in the Krafla volcanic system: Hrafninnuhryggur ('obsidian ridge') and the IDDP-1 borehole (**Fig. 1**). In both cases the glass is taken to represent the melt phase typical of either system (surface and 2.1 km borehole depth, respectively). While these rhyolites are not thought to be genetically linked, they have similar compositions (**Table 1**; Tuffen and Castro 2009; Hampton et al. 2021; Saubin et al. 2021; Rooyakkers et al. 2021b), overlapping values of $\delta^{18}\text{O}$ (IDDP-1: 3.1‰, Hrafninnuhryggur: 2.92–3.28‰; Hampton et al., 2021), and a similar proposed petrogenesis. The differences in composition are subtle in the context of the influence of compositional differences on properties such as viscosity (Hess et al. 1995). In the context of rheological properties, the key difference between the two materials is the dissolved concentration of volatiles, predominantly H_2O . On petrogenetic grounds, a more appropriate direct choice for the surface expression material might have been the recent rhyolitic eruptive products from the Víti crater (Rooyakkers et al. 2021a), however, this material is not as readily available in large glassy chunks such as at Hrafninnuhryggur for large scale testing. The opportunity for sampling large, broadly homogeneous pieces of the Hrafninnuhryggur obsidian, facilitates the multi-method rheological tests that we deploy here. For these reasons, we use the Hrafninnuhryggur obsidian as a proxy for a surface expression of the IDDP-1 rhyolite encountered during drilling.

a. Hrafninnuhryggur obsidian

The ~24 ka Hrafninnuhryggur ridge (eruption age from Sæmundsson et al. 2000) represents a shallow intrusive-to-extrusive rhyolite exposure, extending down to a maximum of 95 m below the paleo-surface (Tuffen and Castro 2009; Tuffen et al. 2010; Saubin et al. 2019; Foster et al. 2024). The rhyolitic surface outcrops (not including the feeder dyke outcrops) at Hrafninnuhryggur include obsidian-dominated and devitrified-rhyolite-dominated facies (Castro et al. 2009; Tuffen and Castro 2009). We used the obsidian as our experimental material throughout (note that the devitrified rhyolite is thought to be the crystallized counterpart of the obsidian).

Across all lithofacies outcropping at Hrafninnuhryggur, the total dissolved H_2O concentration in the obsidian was measured previously by Fourier transform infrared spectroscopy (FTIR) to be between 0.11 ± 0.01 (sample OR1605) and 0.20 ± 0.01 (sample OR1705) in wt.% (Tuffen and Castro 2009), where we have converted standard deviation to standard error using the quoted number of analyses per

sample. Also using FTIR on obsidian from one section of the Hrafninnuhryggur site, Ryan et al. (2015) measured the H₂O concentration to be 0.11 ± 0.04 wt.%, Seropian et al. (2022) measured 0.11 ± 0.01 wt.%, and Weaver et al. (2023) measured 0.10 ± 0.01 wt.%. These ranges of H₂O concentrations are broadly consistent with constraints by thermo-gravimetric analysis in which the bulk mass loss up to a high temperature of 1375 K is assumed to represent a volatile concentration in excess of the solubility at those same temperatures at low partial H₂O pressures of laboratory conditions. Using this method and assuming the volatiles are dominated by H₂O, Wadsworth et al., (2018) and Wadsworth et al., (2019) found 0.14 ± 0.03 wt.%, and 0.15 ± 0.03 wt.% H₂O, respectively.

b. IDDP-1 borehole rhyolite

In the case of IDDP-1, chips of both obsidian and felsite were recovered during drilling. Following previous work, we interpret the obsidian chips as representing the quenched product of the melt stored at depth at Krafla. The obsidian chips were all rhyolitic (**Fig. 2**) and contained minor crystallinity (mostly <3 vol.%), consisting of small, <100 µm, crystals of pyroxene, titanomagnetite, and plagioclase (Elders et al. 2011; Zierenberg et al. 2013; Masotta et al. 2018; Saubin et al. 2021). Rare chips containing high crystallinity (55-100 vol.%) are inferred to reflect partial melting of the host felsite (Zierenberg et al., 2013; Masotta et al., 2018), so are not considered here in the context of magma rheology. Typical glass chip internal textures are shown in **Fig. 3**. The dissolved volatile fractions measured previously on these materials are 1.29–2.15 wt. % H₂O (with outlier individual analyses at 0.09 and 3.42 wt. %) and a CO₂ concentration on the order of 100 ppm (Elders et al. 2011; Zierenberg et al. 2013; Lowenstern and Pitcher 2013; Watson 2018; Bindeman et al. 2021; Saubin et al. 2021). There is no evidence of magma chemical interaction with the drilling fluids, such as hydration, because the measured OH/H₂O ratio is 1.46–2.53 (Zierenberg et al. 2013). Additionally, no evidence for hydrated margins of individual chips were found in FTIR transects (Watson, 2018). Two-pyroxene geothermometry and modelling of the crystallization sequence suggests in situ storage melt temperature of 1123-1193 K (Zierenberg et al. 2013).

c. The Hrafninnuhryggur feeder dyke system

The Hrafninnuhryggur lavas described briefly in Section 2a lie stratigraphically above an intrusive obsidian-dominated rhyolite dyke that is exposed at two depths below the paleo-surface: approximately 35–50 m and 95 m (Tuffen et al. 2010; Saubin et al. 2019; Foster et al. 2024). FTIR analyses show that these intrusions have variable H₂O concentrations in the range 0.32–0.53 wt.% (Tuffen and Castro 2009; Tuffen et al. 2010; Foster et al. 2024). These outcrops are inferred to represent a shallow conduit region that experienced less degassing than the surface outcrops.

3. Analytical and synthesis methods

We supplement the H₂O concentration analyses of those measured in the Hrafninnuhryggur feeder dyke system with new measurements using a ThermoScientific™ FlashSmart™ elemental analyser which employs a modified Dumas method. Glass chips (2–5 mg) are enclosed in tin containers and combusted in the presence of high purity oxygen with helium as a carrier gas. The combustion products in the gas stream are carried to a gas chromatograph where hydrogen is detected by thermal conductivity and then recalculated to a weight percentage of H₂O using the initial sample mass as a total, and the assumption of complete combustion. This device was calibrated using a BBOT standard and verified with secondary standards before and after measuring each sample. Further details pertaining to this method are provided elsewhere (Moussallam et al. 2016; Weidendorfer et al. 2023).

In order to calibrate our thermal analysis methods and the manner in which they can reveal information about the viscosity of melts (discussed in Section 4), we synthesize a small aliquot of obsidian with 2 wt.% H₂O. To do this, we place 151 mg of powdered obsidian from Hrafninnuhryggur along with 3.1 mg of distilled water into a 14 mm long Au capsule (4.0 mm outer diameter, 3.6 mm inner diameter) and seal it shut using a PUK micro-welding system. Then the capsule is loaded into a rapid-quench

molybdenum-hafnium-carbide (MHC) cold-seal apparatus. The sample is compressed to 150 MPa using Ar gas as pressure medium before heating the experimental charge to 1273.15 K at a constant heating rate of 15 °C / min. We hold the capsule at those pressure–temperature conditions for 17.5 hours before quenching the run isobarically. The resultant synthesized sample is a natural obsidian but hydrated with 2 wt.% H₂O. This sample is referred to later as the ‘hydrated obsidian’.

4. Experimental methods

Our experimental methods involved: (1) thermal analysis and (2) rheological determination. The aim of the first approach is to constrain the structural relaxation behavior of both the Hrafninnuhryggur glassy lavas and the IDDP-1 glass chips upon heating. The aim of the second approach is to constrain the rheology of the obsidian lavas at Hrafninnuhryggur. By using existing validated frameworks for silicate melt relaxation dynamics, we can then unify these two approaches and constrain the rheology of the glass at storage conditions intercepted by IDDP-1, and at the Earth’s surface. This workflow is described here.

a. Rheology via thermal analysis using differential scanning calorimetry

We use a Netzsch GmbH Pegasus 404c differential scanning calorimeter to constrain the glass transition temperature (as a function of heating or cooling rate) and gain an approximate constraint of the natural cooling rate of the glass samples (Wilding et al. 1996; Gottsmann et al. 2002). We use 30–50 mg chunks of glass loaded into a lidded platinum-rhodium crucible. The crucible is heated in argon or in air at constant rates of heating. The measurement consists of the heat flow (recorded as a voltage in a thermocouple array) at the base of the sample crucible relative to at the base of an empty reference crucible. We perform runs with new samples; first we heated them at 25 K.min⁻¹ to a temperature of 823 K (in the case of the IDDP-1 samples) and 1123 K (in the case of the Hrafninnuhryggur obsidian), causing relaxation of the glass and eradication of the thermal history associated with cooling in nature or during drilling. Subsequently we cool the sample at a given rate (e.g., 5, 10, 25 K.min⁻¹) to vitrify the melt and impose a given structural configuration of the glass at a known rate, before heating it again at the same rate to evaluate the glass transition under that matched pair of cooling/heating rates. Then this is repeated at different cooling/heating rate pairs to map shifts in the glass transition under a range of rates. This thermal analysis allows us to find the onset and the peak of the glass transition interval below which the glass is a solid and above which the glass can relax applied stresses viscously. In all cases, we subtract a best-fit baseline (applied to temperatures below the glass transition) from the heat flow data. To do this, we look by eye for the heat flow data that is clearly prior (in temperature) to the onset of the glass transition and fit a polynomial of the form $\beta = d_1 T^{-1} + d_2 T^{-2} + d_3$ (Maier and Kelley 1932) to the data, where β is the heat flow (in arbitrary units), T is the temperature, and d_1 , d_2 and d_3 are fit constants. We then subtract this best-fit function from the data in order to render the heat flow curve flat (‘baseline subtracted’) prior to the glass transition.

The technique of matched cooling-heating runs allows us to observe the dependence of the glass transition on the rate of temperature change (Wilding et al. 1996; Gottsmann et al. 2002), using the semi-empirical relation

$$\mu|_{T_g} = \frac{c}{|q|} \quad \text{Eq. 1}$$

where $\mu|_{T_g}$ is the viscosity assessed at the glass transition temperature T_g , $|q|$ is the absolute value of the heating or cooling rate q , and c is a constant (with units of Pa.K) that relates the viscosity to its imposed prior cooling and re-heating history (sometimes referred to as a ‘shift factor’). c is a weak function of glass composition, and there exists an empirical calibration that relates c to the mol.% cations in the melt that are excess to the charge balancing roles \mathcal{X} dictated by the network-forming cations (Gottsmann et al. 2002). This empirical model is $c = 10.321 - 0.175 \ln(\mathcal{X})$.

For the average of the Hrafninnuhryggur and IDDP-1 compositions given in **Fig. 2** (see **Table 1**), we find that $c \approx 1.21 \times 10^{10}$ Pa.K and $c \approx 1.43 \times 10^{10}$ Pa.K, respectively. These values are found via \mathcal{X} with zero H₂O accommodated in the calculation (i.e., anhydrous compositions); this is discussed later in Section 5). To arrive at these values, we assume that the net effect of iron is not substantial, given that whatever oxidation state we assume (partitioning iron into FeO and Fe₂O₃), the contribution of iron to \mathcal{X} is negligible.

b. Relaxation geospeedometry using differential scanning calorimetry

In silicate glasses, a given property p (such as shear stress) will relax with time proportional to a characteristic relaxation time λ . A common constitutive relaxation equation is the Kohlrausch-Williams-Watts function $p = p_0 \exp[-(t/\lambda)^\zeta]$ where p_0 is the initial value of p prior to relaxation (such as the applied stress), t is time since the onset of relaxation, and ζ is an exponent that, when $\zeta < 1$, stretches the relaxation function beyond a simple exponential, and which is often required to fit data (Kohlrausch 1854; Williams and Watts 1970; Debolt et al. 1976; Kenderes and Whittington 2021). The propensity for glasses to relax a given property underpins the idea behind relaxation geospeedometry in which the functional shape of the evolution of the heat capacity across the glass transition is dictated by the enthalpy relaxation path taken by the glass (Debolt et al. 1976). Because the heat capacity evolution at a given heating rate is dictated by the cooling rate at which the glass was formed, models for heat capacity evolution can be used to extract the cooling rate at which glass forms. The theoretical underpinning of this model is described elsewhere (Debolt et al. 1976; Hodge 2008) and so here we simply introduce the procedural methodology for extracting the cooling rate at which glass – including natural glass – forms.

The fictive temperature T' is the temperature at which the molecular structure of a glass was in equilibrium. At high temperatures far in excess of the glass transition T_g , the fictive temperature and the absolute temperature are equal $T' = T$. If a glass is cooled at a constant rate from the condition that $T' = T$, then at a certain temperature, the glass structure will cease to be in equilibrium because the structure becomes relaxation-limited. A functional model for T' is (Debolt et al. 1976)

$$T' = T_0 + \sum_{j=1}^m (T'_{(j-1)} - T_{(j)}) \left(1 - \exp \left[- \left(\sum_{k=j}^m \frac{T_{(k)} - T_{(k-1)}}{q \lambda_{(k)}} \right)^\zeta \right] \right) \quad \text{Eq. 2}$$

where T_0 is a temperature far from T_g , j is the index of the iteration being performed in Eq. 2, q is the cooling or heating rate, $\lambda_{(k)}$ is the relaxation timescale at index k (i.e., at a given temperature step) and m is the final step. In practice, this is a sum, as shown in Eq. 2, but more properly is an integration procedure. $\lambda_{(k)}$ is given by

$$\lambda_{(k)} = \lambda_0 \exp \left[s \frac{\Delta H}{RT_{(k)}} + (1 - s) \frac{\Delta H}{RT'_{(k-1)}} \right] \quad \text{Eq. 3}$$

where λ_0 and s are fit parameters with $0 < s < 1$ bounds. ΔH is the enthalpy of relaxation. Here R is the universal gas constant. In order to convert Eq. 2 to a heat flow signal, we use

$$\frac{dT'}{dT} = \frac{\beta - \beta_g}{\beta_l - \beta_g} \quad \text{Eq. 4}$$

where β is the heat flow signal, β_g is the heat flow signal in the glass (given by the baseline normalization introduced in Section 4a), and β_l is the constant high-temperature heat flow signal for the melt.

Procedurally, we use differential scanning calorimetry (introduced in Section 4a) to record the heat flow signal across the glass transition (which is a proxy for the heat capacity). First, we load a sample that was cooled at an unknown rate termed the ‘natural’ cooling rate, and heat it at a known heating rate. This produces a signal that we must model using Eqs 2 & 3 in order to predict the cooling rate at which the glass was originally formed in nature or during drilling. However, for a given glass, ζ , s , ΔH , and λ_0 are all unknowns that depend on glass composition only (Kenderes and Whittington 2021). Therefore, once the natural signal is obtained, we then heat and cool the samples at known matched cooling-heating rates, cycling through the glass transition window. By doing this, we set q in Eq. 2 to a given value that is the case on both the cooling and the subsequent heating cycle. We then minimize using a least-squares regression (Kemmer and Keller 2010) for the fit parameters ζ , s , and λ_0 . We find ΔH by acknowledging $-\ln q = -\ln q_0 + \Delta H/(RT_g)^*$, where q_0 is a fit parameter intercept[†] in a plot of the peak glass transition temperature T_g from the signal as a function of q . Once the fit parameters are determined, the ‘natural’ curve signal can then be fit with only one fit parameter that is q on cooling.

c. Rheological determination

We use a combination of methods to determine the rheology of natural obsidian from Hrafninnuhryggur that, taken together, cover a wide range of applied temperatures and shear stresses. The aim of this multi-method approach is to build a full picture of the melt behavior across all conditions extant in shallow magma transport and eruption.

First, to determine the viscosity at relatively high temperatures, we use a rotational rheometer in which crushed chips of each raw glass are loaded into thin-walled platinum crucibles and stirred at 1773 K for 24 hours, using a Pt₈₀Rh₂₀ spindle to homogenize and remove bubbles. The samples are then removed from the thin-walled synthesis crucible by drilling and hammering. The resulting chips are transferred to a thick walled Pt₈₀Rh₂₀ viscometry crucible of exact geometry and stirred again to ensure homogenization and an absence of bubbles. A Pt₈₀Rh₂₀ viscometry spindle (Dingwell and Virgo 1988) is immersed in the melt and controlled using a Brookfield viscometer which operated at rotation speeds of 0.1–40 rpm. The apparatus, technique, and data processing are described by Dingwell (1989). The technique involves a series of temperature reduction steps with dwells of 1 hour to ensure the system equilibrates thermally, yielding constant torque. The equilibrium torque is then proportional to the shear stress, which is used with the rotation rate to compute the shear viscosity.

At lower temperatures, just above the glass transition interval, we apply the micro-penetration technique (Hess et al. 1995). This involves determining the rate at which a hemispherical iridium indenter displaces the melt when a fixed load is applied. These measurements are applied to the obsidian, cut into 3 mm long plane-parallel discs 5 mm in diameter and polished on both surfaces. The sample is placed in a Netzsch GmbH 402 F1/F3 Hyperion thermo-mechanical analyzer under argon gas flow and the indenter is attached to the vertical push rod. The viscosity is then determined from $\mu = \gamma Ft(\xi\alpha^3)^{-1/2}$ where $\gamma = 0.1875$ is a dimensionless constant for a hemispherical indenter, F is the applied force, t is the time since contact of the indenter, ξ is the indenter radius (1 mm in this case) and α is the time dependent distance into the silicate liquid (Pocklington 1940; Tobolsky and Taylor 1963). The viscosity μ is taken at steady-state (high values of t at which $d\alpha/dt$ becomes constant).

In addition, we can access the relatively low-temperature end of the viscosity spectrum using cylinder compression rheometry, which involves the uniaxial compression of cylinders (Gent 1960; Hess et al.

* In some published work there is a 2.303 factor in this equation, which is incorporated when the logarithm to the base 10 is used in place of the natural logarithm (Kenderes and Whittington 2021) which otherwise is not required (Debolt et al. 1976).

[†] We note that in some published sources, what we denote as q_0 is erroneously equated to λ_0 (Kenderes and Whittington 2021), despite the discrepancy in dimensional units between those two parameters.

2007). We undertook these tests at two scales. At small scale we used a Netzsch GmbH Hyperion® TMA 402 F1 device in which a cylindrical sample 5 mm in diameter and 10 mm in length was set between two ceramic plates and compressed at known applied force (set at 0.1–3 N with 0.2 mN accuracy). The device is encased in a furnace with a maximum temperature of 1775 K and with accuracy (after temperature calibration) of ± 2 K. These measurements are performed in air and sample expansion during heating is subtracted as a baseline prior to deformation. The dependent variable is then the change in sample length with time during pressing. At large scale, compression tests were undertaken at high forces using a 300 kN uniaxial press (from Voggenreiter GmbH with an Instron® hydraulic control system upgrade) on cores of Hrafninnuhryggur obsidian 20 mm in diameter and 40 mm in length. The first iteration (pre-upgrade) of this device and calibration thereof is described in Hess et al. (2007). Linear variable differential transducers (LVDTs) with 10^{-6} m resolution and 150 mm travel range maxima are used with a hydraulic system to operate the position of the upper piston. Force is measured with a Lorenz Messtechnik GmbH K11 load cell with 300 kN working range and an approximate accuracy of 0.05%. While the press can operate in force control mode – wherein the position is the dependent variable of interest – we choose to use it in position control – wherein the force variation with time is the dependent variable of interest. In this position-control mode, the working range of piston velocity is $8.3 \times 10^{-7} \leq u \leq 1.0 \times 10^{-2} \text{ m}\cdot\text{s}^{-1}$ (Wadsworth et al. 2018). A Gero GmbH 3-zone split furnace surrounds the sample and the working pistons either side of the sample with a maximum temperature of 1375 K with a maximum temperature gradient ± 5 K on the sample scale in the hot zone. This furnace has a 0.12 m long uniform hot zone when insulated (Cordonnier et al. 2012c). Temperature is recorded using K-type thermocouples in the air, sample, and in contact with the pistons. Moreover, in these large-scale experiments, acoustic emissions (AEs), associated with potential cracking events during deformation (Vasseur et al. 2018), are tracked via two piezoelectric AE broadband transducers with 125 kHz frequency. The AE signals are fed to a 40 dB buffered pre-amplifier, and recorded in a Richter data acquisition system at 20 MHz from Applied Seismology Consultants. AE event onsets are triggered and recorded using continuous signals via an autoregressive-Akaike-Information-Criterion (AE-AIC) event picker (Beyreuther et al. 2010). The AE-AIC works by detecting a signal onset by using a short-term average/long-term average (STA-LTA) detector algorithm with a time-window of 1 and 20 ms respectively, with an STA/LTA threshold of 2. The signal is then denoised with an amplitude threshold of 68 dB, before picking the signal arrival time using the minimum of the computed AE-AIC signal (Vasseur et al. 2015).

In both the small- and large-scale compression experiments, we look for one of two responses of the samples to deformation. First, we look for a viscous response, which is found when the force F required to maintain a given axial deformation rate $\dot{\gamma}$ rises and equilibrates at a constant value in the absence of acoustic emissions above background. When this response is observed, we can use a well-known model for the viscosity of the cylindrical sample (Gent 1960).

$$\mu = \frac{2\pi F h(t)^5}{3V \dot{h} (2\pi h(t)^3 + V)}, \quad \dot{h} = \frac{dh}{dt} \quad \text{Eq. 5}$$

where V is the sample volume, $h(t)$ is the time-dependent sample height, F is the force applied at each instant of time, and \dot{h} is the velocity (the first-time derivative of the changing sample height) of the piston, where $\dot{\gamma} = \dot{h}/h_0$ with h_0 the initial height. The second possible response of a sample to deformation is a brittle one, recognized when the force value drops intermittently in sharp punctuated events which can be attributed to sample cracking. AEs are also indicative of brittle responses. Analysis of these deformation modes is discussed extensively elsewhere (Coats et al. 2018; Wadsworth et al. 2018) and applied here. Eq. 5 assumes no slip between the pistons and the sample cylinder contacts, which is visually confirmed post-experiment (i.e., the top and bottom end sample radius is within uncertainty of the initial radius). We apply the Trouton correction where the internal shear strain rate $\dot{\epsilon}$ is $\dot{\epsilon} \approx 3\dot{\gamma}$.

5. Results and analysis

Our results are divided into (1) the calibration of the shift factor for hydrous rhyolite melts (Section 5a), (2) the determination of the relaxation behavior and associated glass transition temperature intervals for the materials tested herein (Section 5b), (2) a constraint of the temperature-dependence of viscosity (Section 5c), and (3) unrelaxed viscoelastic effects using a universal melt deformation map (Section 5d). Taken together, these results represent characterization of the IDDP-1 and surface rhyolitic magma rheology.

a. Calibrating the shift factor for hydrous rhyolite

The shift factor c used in Eq. 1 is important for understanding the relationship between the relaxation temperature window and the viscosity at the glass transition. Gottsmann et al. (2001) showed that c relates to the excess cations \mathcal{X} but did not test the effect of H_2O . Therefore, we present a calibration test using the synthesized sample of Hrafninnuhryggur composition (remelted) but hydrated to 2 wt.% H_2O . Using a cooling and heating rate of $|q| = 10 \text{ K} \cdot \text{min}^{-1}$, we find that the glass transition peak temperature is $764 \pm 2 \text{ K}$. Measured using the micro-penetration technique (see Section 4), the viscosity at that exact temperature is $8.13 \times 10^{10} \text{ Pa} \cdot \text{s}$ (with an uncertainty of 0.1 log units). Using Eq. 1, this yields a direct determination of the shift factor by $c = \mu|q| = 1.35 \pm 0.31 \times 10^{10} \text{ Pa} \cdot \text{K}$.

The above determination of c is within error of the value computed using the anhydrous Hrafninnuhryggur composition $c \approx 1.21 \pm 0.05 \times 10^{10} \text{ Pa} \cdot \text{K}$ and the anhydrous IDDP-1 composition $c \approx 1.43 \pm 0.14 \times 10^{10} \text{ Pa} \cdot \text{K}$ (see Table 1). The uncertainties on these values of c computed using the Gottsmann et al. (2001) method arise from taking $\pm 1\sigma$ standard deviation on the compositions given in Table 1 to compute an upper and lower limit on c . We find that H_2O does not have the same effect on the shift factor as the effect of the mol.% excess cations, and we neglect the effect of H_2O on c when c is computed using Gottsmann et al. (2001). To illustrate this further, if we were to compute c using the Gottsmann et al. (2001) model and assuming that the dissolved H_2O is to be incorporated in the mol.% excess cations (\mathcal{X}), then for 2 wt.% H_2O , we would arrive at $c \approx 8.57 \pm 0.40 \times 10^9 \text{ Pa} \cdot \text{K}$ for the Hrafninnuhryggur base composition (Table 1). This is clearly far lower than the measured value.

The shift factor c relates directly to the shear modulus of the melt G (Schawe and Hess 2019) such that $c = G\omega$, where ω has units of K^{-1} and is approximately of order unity (Sipp and Richet 2002). Given that the shear modulus also depends on the dissolved H_2O concentration in rhyolites (Malfait et al. 2011; Whittington et al. 2012), we can account for this possible effect. We compile data for $G(C_{\text{H}_2\text{O}})$ for rhyolitic melts and demonstrate the weak effect of water on the shear modulus, which can be accounted for by $G(C_{\text{H}_2\text{O}}) = b_1 - b_2 C_{\text{H}_2\text{O}}$ where $b_1 = 30.32 \text{ GPa}$ and $b_2 = 0.42$ (Fig. 4). If we assume that this $G(C_{\text{H}_2\text{O}})$ effect contributes to c by the same factor, then using 2 wt.% H_2O as the approximate nominal value, then we find that the factor by which c would be modified from a dry composition would be 0.97. Applying this to the dry value of c , we find our dry estimate (i.e., for IDDP-1 using the dry Gottsmann et al. 2001 method) would be reduced to $c \approx 1.39 \pm 0.14 \times 10^{10} \text{ Pa} \cdot \text{K}$, which is within error of both the measured value, and the original computed value. This means that if there is an effect of H_2O on G that should be propagated to c , then it is either small or it does not exist, and our measurements cannot distinguish these possibilities. Therefore, we do not directly account for H_2O in our determination and use of c . This requires further dedicated investigation to confirm as a general rule for hydrous silicate melts and further work should aim to reduce the uncertainties in the direct determinations of c .

b. The glass transition of the IDDP-1 and Hrafninnuhryggur rhyolitic magma

We find that the IDDP-1 chips have a glass transition onset of $697 \pm 3 \text{ K}$ and peak of $802 \pm 1 \text{ K}$ when analyzed as-collected (Fig. 5a); that is, on ‘first heating’ of the glass chips. Similarly, the Hrafninnuhryggur obsidian has a glass transition onset of $904 \pm 5 \text{ K}$ and peak of $998 \pm 1 \text{ K}$ when analyzed as-collected (Fig. 5a). When we cool the chips and re-heat them at the same rate, we find that the onset remains around $698 \pm 5 \text{ K}$, but the peak is a function of the imposed cooling and heating rate

combination (**Fig. 5b**). The measured peak temperatures on cooling-heating cycles are 773 K (at 5 K.min⁻¹), 783 K (at 10 K.min⁻¹), and 805 K (at 25 K.min⁻¹) (**Fig. 5b**). When we apply the same method to the Hrafninnuhryggur obsidian, we find again that the onset is relatively stable at 923 ± 1.4 K for all heating-cooling cycle rates, but that the peak temperature shifts from 1005 K at 10 K.min⁻¹, up to 1035 K at 30 K.min⁻¹ (**Fig. 5c**). This relative constancy of the onset temperature as well as the dependence of the peak temperature on the imposed thermal history is well documented and underpins the semi-empirical models that aim to convert these temperatures and rate information into equilibrium viscosities (Wilding et al. 1996; Gottsmann et al. 2002). As expected, the glass transition temperature shifts to higher values for higher rates of matched cooling/heating cycles. Interestingly, following geospeedometry interpretations (Wilding et al. 1996; Lavallée et al. 2015b), the similarity of the first-heating heat flow data (**Fig. 5a**) to the 25 K.min⁻¹ matched heating-cooling data (**Fig. 5b**) suggests that the glass chips were quenched during drilling at around 25 K.min⁻¹. The natural quench rate of the Hrafninnuhryggur surface obsidian is slower than 25 K.min⁻¹. In **Fig. 5d** we formally apply the geospeedometry methodology (see Eqs 2–4; Wilding et al. 1996; Lavallée et al. 2015b) to give the computed natural cooling rate for both IDDP-1 and Hrafninnuhryggur. We find that the cooling rate was likely to be between 7 ± 1 and 80 ± 31 K.min⁻¹ for IDDP-1 and around 7 ± 1 K.min⁻¹ for Hrafninnuhryggur.

c. Relaxed melt viscosity

The rheological measurements undertaken at low loads – that is all results obtained from the micro-penetration measurements, the thermo-mechanical analysis, and the uniaxial press under low strain rates – provide a constant ‘relaxed’ value of viscosity and a single value of viscosity for a given temperature, irrespective of the applied conditions. No vesiculation occurred during these tests. Thus, we deem the viscosity obtained to represent the viscosity of a Newtonian system at these conditions. Moreover, the results from the thermal analysis (**Fig. 5**) can be used to estimate the relaxed melt viscosity at the glass transition temperature (**Section 4b**). In order to understand these viscosity values, together with the viscosity values from our rheological study (**Section 4a**), we use the empirical non-Arrhenian Vogel-Fulcher-Tammann (VFT) viscosity law in functional form

$$\mu(T) = \mu_0 \exp\left(\frac{B}{T - T_0}\right) \quad \text{Eq. 6}$$

where μ_0 , B , and T_0 are constants to be determined. As discussed (**Section 1**) the primary difference between the IDDP-1 rhyolite and the surface Hrafninnuhryggur rhyolite is the dissolved H₂O concentration in the melt, which in turn has a first-order control on the viscosity (Hess and Dingwell 1996; Giordano et al. 2008). Hess and Dingwell (1996) used a parameterization via $\mu_0 = a_1 + a_2 \ln(C_{\text{H}_2\text{O}})$, $B = a_3 + a_4 \ln(C_{\text{H}_2\text{O}})$, and $T_0 = a_5 + a_6 \ln(C_{\text{H}_2\text{O}})$ for which $a_1 = -8.163$, $a_2 = 1.918$, $a_3 = 22107$, $a_4 = 5453$, $a_5 = 195.7$ and $a_6 = 32.25$. These constants are found by performing a global minimization of Eq. 3 to experimental test data from published sources (Friedman et al. 1963; Shaw 1963; Burnham 1964; Persikov et al. 1990; Hess et al. 1995; Baker 1996; Dingwell et al. 1996; Schulze et al. 1996; Dorfman et al. 1996; Scaillet et al. 1996) that were collected using similar techniques to those employed herein. Here, we compile those same data in order to visually assess the quality of the minimized model (**Figs 6a & 6c**). We find that the fit is reliable at predicting the data with particular efficacy at $C_{\text{H}_2\text{O}} \leq 4$ wt.% (**Fig. 6a**) which encompasses the values found for IDDP-1 and other Krafla rhyolites (Tuffen and Castro 2009; Zierenberg et al. 2013; Watson 2018; Saubin et al. 2021).

Using our data for Hrafninnuhryggur and for IDDP-1, we can fit the Hess and Dingwell (1996) viscosity model for the best-fit H₂O concentration. To do this, we use a least-squares minimization (Kemmer and Keller 2010). However, in order to capture the uncertainty associated with the shift factor c (see Section 5a), which impacts the viscosity values derived from DSC measurements, we take a Monte Carlo approach. First, we assume that the real value of c is given by a normal probability

distribution with the best estimate c as the mean, and the uncertainty on c as the standard deviation about the mean. Then we draw a value of c from this distribution and use it to locate the DSC data in a viscosity plot (**Fig. 6**). Finally, we fit for H₂O using Hess and Dingwell (1996) via Eq. 3. We then repeat this 10⁶ times, thereby capturing the effect of the uncertainty on c . With the results, we then take the mean and standard deviation of the H₂O concentrations so that the quoted global best-fit value is $C_{\text{H}_2\text{O}}$ and the uncertainty is given by the standard deviation of the best-fit values of H₂O. In the case of IDDP-1, this results in a global fit of $C_{\text{H}_2\text{O}} = 2.12 \pm 0.08$ wt.%. In the case of Hrafninnuhryggur, this results in $C_{\text{H}_2\text{O}} = 0.12 \pm 0.01$ wt.% (we note that ± 0.01 wt.% is the uncertainty on the fit across all data, which is larger than the uncertainty associated with randomly varying c as described above). Other viscosity models could have been used to perform this minimization (Romine and Whittington 2015).

d. Unrelaxed behavior and melt rupture

Here we explore the results of the high-load compression tests in which large 20 mm diameter samples of the Hrafninnuhryggur obsidian were deformed under high relative rates of axial strain. The experiments, which had either a measured force drop, a measured acoustic emission signal, or both, were denoted as brittle, whereas the rest were denoted as viscous. New results presented here are combined with published results using the same obsidian (Tuffen et al. 2008; Wadsworth et al. 2018) and other melts (Dingwell and Webb 1989) in order to explore a universal threshold for unrelaxed melt rupture (brittle) in response to stress.

To analyze our results, we use the framework given by Wadsworth et al. (2018). First, we constrain the melt relaxation timescale $\lambda = \mu/G$ and the deformation timescale $\lambda_d = \dot{\epsilon}^{-1}$, which can be combined in a dimensionless Weissenberg number $Wi = \lambda/\lambda_d = \mu\dot{\epsilon}/G$. Here, $Wi \ll 1$ is the case where the relaxation time is relatively short compared with the deformation time, such that there is sufficient time for relaxation of the melt during flow and bulk relaxed viscous behaviour is expected. By contrast, $Wi \gg 1$ is the case where the deformation time is short and unrelaxed behaviour can be expected. Because significant strain is reached in our tests, the high- Wi regime can result in substantial accumulation of stress and bulk brittle responses. As Wi exceeds a critical value, this can result in solid-like behavior and wholesale melt rupture (Cordonnier et al. 2012c; Coats et al. 2018; Wadsworth et al. 2018). We note that in Coats et al. (2018), Wi is given as a Deborah number De , which should be reserved for oscillatory deformation and is only equivalent to Wi when the Cox-Merz rule is assumed correct. The same brittle regime can be inferred from other work (e.g., via textural analysis and acoustic emission monitoring) even if Wi is not explicitly constrained (Lavallée et al. 2008, 2013; Kendrick et al. 2013). Wadsworth et al. (2018) found that across a wide range of sample compositions, including the Hrafninnuhryggur obsidian, $Wi = 0.04$ is the critical value above which melt will rupture, and that the window $0.01 \leq Wi \leq 0.04$ is the transition from viscous to brittle behavior for increasing Wi .

Our data for the deformation of Hrafninnuhryggur glass matches the prediction that $Wi \geq 0.04$ will result in a brittle response (**Fig. 7**) and push the validation of this viscoelastic theory to lower values of λ (i.e., higher temperatures) and lower values of λ_d (i.e., higher deformation rates) than tested previously.

For comparison we add data from Wadsworth et al. (2024) in which crystal-rich lavas with crystallinities up to 0.55 and low porosity (<0.01) were deformed in the same way. To analyze those samples, Wadsworth et al. (2024) adapt both the relaxation and the deformation timescales to accommodate the presence of crystals and pores. This framework is then compared with previous data for the deformation of natural, porous, crystal-bearing lavas (Lavallée et al. 2007, 2013; Kendrick et al. 2013; Coats et al. 2018), crystal-bearing synthetic glasses (Cordonnier et al. 2012a) and crystal-bearing synthetic glasses with nominally low porosity (Pistone et al. 2012). Here, all of these results are given as ‘Wadsworth et al. (2024)’ on the grounds that the re-calculation of the relaxation and deformation timescales (that locates them in Fig. 7) originates therein. Because these results provide a dimensionless framework for predicting the viscous-to-brittle transition in flowing rhyolites of variable crystallinity, they therefore also show that this deformation map (**Fig. 7**) should be valid for the crystal-bearing components of the sub-surface at Krafla, such as partially molten felsite, or Krafla rhyolite glass that undergoes rapid crystallization (Cáceres et al. 2021).

e. Additional H₂O concentration data for the Hrafninnuhryggur feeder dyke

The H₂O determinations found here for the feeder dyke system are 0.25–0.55 wt.% (see Supplementary Data). These supplement existing data from FTIR for the same feeder dyke rocks (Tuffen and Castro 2009; Foster et al. 2024), data for the surficial lavas (Tuffen and Castro 2009), data for KJ-39 retrieved glass (Rule 2020), and data for chips recovered from IDDP-1 (Zierenberg et al. 2013; Lowenstern and Pitcher 2013; Watson 2018; Bindeman et al. 2021; Saubin et al. 2021). In **Fig. 8** we show a histogram of these H₂O data which reveal the full spectrum of water concentration between the degassing conditions at the surface (at Hrafninnuhryggur) and the average ~1.73 wt.% quenched in during IDDP-1 drilling. Interestingly, the glass chips retrieved from drilling mud show quenched magma can ultimately hold a wide range of H₂O concentrations presumably as variable extents of degassing may take place due to drilling activities prior to quenching. Importantly, the continuum in water concentration in **Fig. 8** indicates that a spectrum of melt viscosity co-exists in the system perturbed by drilling activity.

6. Discussion

Our results constrain the viscosity and viscoelastic rheology (up to and including the brittle limit) of rhyolites at Krafla volcano including the first-order effects of temperature and H₂O concentration. We have exploited the fact that at Krafla, quenched samples of pristine rhyolitic magma are available from both the shallow storage reservoir and the surface, in order to examine how the rheology changes up through the shallow crust. Here, we explore these results in the context of the goals of the Krafla Magma Testbed (KMT) and outline how these results can be used in future work to prepare for new drilling campaigns at Krafla. The aim of the KMT is to pursue further drilling opportunities at Krafla volcano in order to cross a ‘last unexplored frontier’ (see <https://www.kmt.is/>) and monitor and explore our magma filled crust. Ultimately, endeavors such as these are potentially hazardous simply because the response of rhyolite to drilling is poorly understood. Magmas are increasingly considered as desirable environments to augment geothermal energy supply but ultimately, endeavors such as these require a robust quantification of magma rheology.

a. The viscosity and rheology of rhyolites from storage to the surface

Our results relate the H₂O concentrations to the viscosity via the model of Hess and Dingwell (1996) (**Fig. 6**). If we now take the bounds on the predicted IDDP-1 storage temperature of 1123–1193 K (Zierenberg et al. 2013) we can demonstrate how our validated model for the viscosity varies with H₂O concentration (**Fig. 8**). The lower bound on the viscosity at this temperature is the storage viscosity ~1.31 – 5.50 × 10⁵ Pa.s (constrained with the relaxation of IDDP-1 glass chips; **Fig. 6b**), whereas the upper bound on the viscosity at this temperature is the surface viscosity ~2.35 × 10⁹ Pa.s (constrained via relaxation and rheometry using the Hrafninnuhryggur glass; **Fig. 6b**). We can acknowledge that the eruption temperature of the Krafla rhyolites, leading to the emplacement of Hrafninnuhryggur, may be lower than the storage temperature of 1123–1193 K, such that the surface viscosity given in **Fig. 8** could be higher. For example, if we take the lower relative storage temperature estimate for the Chaitén 2008 rhyolite of 1098 K (Castro and Dingwell 2009), then the viscosity would be ~5.62 × 10⁹ Pa.s. Nevertheless, the model constraints provided herein allow this to be computed if the eruption temperature is known.

Here, we focus on the Hess and Dingwell (1996) model for viscosity, which is specifically calibrated for rhyolites. If instead we use a composition-dependent model (Giordano et al. 2008), we see that the differences associated with the small compositional variations between IDDP-1 and Hrafninnuhryggur glasses are minor compared with the effect of dissolved H₂O (**Fig. 8**).

Our results imply that future magma drilling efforts at Krafla as part of KMT must constrain the evolution of dissolved H₂O, due to perturbations in pressure and temperature associated with drilling, in order to predict the evolution of viscosity accurately. Given that these rhyolites have a propensity to

fracture when cooled and pushed to strain at an increased rate (**Fig. 7**), these parameters will be of importance to predict if and/or when brittle failure and fragmentation may occur in response to drilling.

The deformation map presented in Fig. 7 can be used to understand the conditions of strain rate required for failure to occur. However, the deformation map presupposes that the strains will be large (Wadsworth et al. 2018). In fact, it takes a finite time – and therefore strain – for the failure to onset and this time is not accounted for by the deformation map scaling given here. Instead, to find the time for failure we use Maxwell’s viscoelasticity which states

$$\sigma + \frac{\mu}{G} \frac{d\sigma}{dt} = \mu \dot{\epsilon} \quad \text{Eq. 7}$$

where σ is the shear stress in the melt. If $\dot{\epsilon}$ and μ are both constant, as is the case in our experiments, and if $\sigma = 0$ at $t = 0$, then Eq. 7 leads to a prediction of $\sigma(t)$ as

$$\sigma(t) = \mu \dot{\epsilon} \left[1 - \exp\left(-\frac{tG}{\mu}\right) \right]. \quad \text{Eq. 8}$$

Our experimental finding that failure occurs for $Wi \geq 0.04$ is akin to finding that the critical stress for failure is $\sigma_c = 0.04G \approx 4 \times 10^8$ Pa. Eq. 8 can then be used to find the critical time t_c it takes for σ to reach σ_c as

$$t_c = -\frac{\mu}{G} \ln\left(1 - \frac{\sigma_c}{\mu \dot{\epsilon}}\right) \quad \text{Eq. 9}$$

or, as a finite strain required for failure ϵ_c

$$\epsilon_c = -Wi \ln\left(1 - \frac{\sigma_c}{\mu \dot{\epsilon}}\right) \quad \text{Eq. 10}$$

Eqs 9 and 10 then acknowledge that there can be viscous deformation occurring for a finite time (or strain) prior to viscoelastic rupture, which has been confirmed experimentally (Dingwell and Webb 1989; Cordonnier et al. 2012c; Wadsworth et al. 2018; Namiki et al. 2023). Note that Eqs 8–10 are specific to the case where strain rate is held constant and in cases of variable strain rate, a numerical solution to Eq. 7 is required.

b. Potential rheological impact of microlites, nanolites, and iron oxidation

The viscosity of silicate magma is influenced by both melt chemistry and the presence of crystals. In the case of Krafla, the rhyolitic magma contains a high concentration of iron. In **Fig. 9** we report the average glass total iron (FeO_T) as a function of the silica (SiO_2) as compared with rhyolite glasses worldwide using a published database (Di Genova et al. 2017). This shows that the Hrafninnuhryggur obsidian and IDDP-1 glass are among the most iron-rich natural rhyolitic glasses known (Wadsworth et al. 2021a).

Iron can play a role in magma rheology due to changes in oxidation state, which impacts the configuration and role of iron in the melt structure (Dingwell 1991). Additionally, iron can promote crystallization, including the formation of iron-rich nanolites (Mujin et al. 2017; Di Genova et al. 2018, 2020; Cáceres et al. 2020, 2021, 2024; Okumura et al. 2022; Pereira et al. 2024). Interestingly, the

precipitation of iron-rich nanolites can have a knock-on effect on the melt viscosity which can, in some cases, be substantial (Zandonà et al. 2023; Cáceres et al. 2024; Pereira et al. 2024). Having said that, the volume fractions of nanolites tend to be small (Okumura et al. 2022), reducing their expected effect on the bulk magma viscosity (Mader et al. 2013; Vasseur et al. 2023) and the direct compositional effects involving the role of iron tends to be small relative to the effects of temperature and water (Chevrel et al. 2014).

The formation and growth of Fe-oxide crystals in Krafla rhyolite can result from oxidation of the melt (Cáceres et al. 2021). Contrastingly, Castro et al. (2009) showed that the formation of Fe-oxide crystals can reduce the melt in an oxidation state buffered crystallization step associated with H₂O movement. Casas et al. (2019) used titration methods to determine the iron oxidation ratio in the Hrafnatinnuhryggur as-collected glass, and found that the ratio of Fe³⁺ to total Fe, termed Fe_T, was Fe³⁺/Fe_T = 0.167, similar to the ‘clear glass’ in the spherulite-bearing samples (Fe³⁺/Fe_T = 0.165 ± 0.04) reported by Castro et al. (2009). Other than these sparse measurements, the oxygen fugacity for each rhyolite body at Krafla is poorly constrained and so this effect of iron on melt structure and rheology should be investigated further in future.

Our deformation map (Fig. 7) suggests that this growth of any crystals will strongly affect the viscoelastic properties if the crystallization reaches high volume fractions relative to a ‘maximum packing’ fraction (Wadsworth et al. 2024). For example, if crystallinities were to reach ≈ 40 vol. %, then the viscosity would increase by one log unit (Mader et al. 2013). Clearly, iron-bearing nanolites cannot crystallize to such high volume fraction. However, if the rhyolite is stored hot for sufficient time for further crystallization, or if another rhyolite which has crystallized is intersected by drilling at Krafla, then our deformation map can be used to constrain the rheology (Fig. 7).

Future work should explore whether interactions with drilling fluids and/or drilling-induced decompression and cooling could trigger sufficient oxidation of iron to induce nanolite or microlite formation (Di Genova et al. 2018; Cáceres et al. 2021) before quenching. Importantly, the fact that the clear-glass IDDP-1 glass chips (Saubin et al. 2021), such as the chips used here, conform to the Hess and Dingwell (1996) viscosity model appears to demonstrate that nanolites did not form, based on the assumption that their presence would influence the rheology measured. However, the so-called brown glass explored by Saubin et al. (2021) and others may contain nanolites.

c. The transport system from the source to surface and implications for KMT and drilling

We have direct access to rhyolite at the storage region (via IDDP-1) and the surface (via Hrafnatinnuhryggur) or the near-surface (via the Hrafnatinnuhryggur feeder dyke system). The surface Hrafnatinnuhryggur rhyolites appear texturally indistinguishable from effusive lavas (cf Fink 1983). However, Foster et al. (2024) found evidence that these lavas are formed from welding of ash-sized particles, similar to the processes that form welded and rheomorphic ignimbrites (cf Branney and Kokelaar 1992), supporting the so-called ‘cryptic fragmentation’ rhyolite emplacement model (Wadsworth et al. 2020, 2022b) as a basis for rhyolite dyke and lava emplacement. Weaver et al. (2023) additionally showed that secondary vesiculation and sintering occurs in breccia zones. In this model, magma fragmentation is vigorous and occurs at depth, producing pyroclasts that are transported up the conduit where a fraction of the pyroclasts are ‘captured’ at shallow depths and weld to the conduit walls. Those welded deposits are then advected out of the vent as lava. This is pertinent to the drilling scenarios because it suggests that the Krafla rhyolites can readily fragment in vigorous explosive eruptions when subjected to a decompression (Rooyackers et al. 2020).

The observation during the IDDP-1 drilling was that no catastrophic fragmentation occurred. That is, drilling intercepting magma did not produce an eruption (Ilic et al. 2020). Nevertheless, understanding the range of behaviors that are possible with this rhyolite or any other rhyolite is critical to understanding the generalized suite of possible responses magma could exhibit during drilling.

Traditional conceptual models (those that do not invoke vigorous fragmentation) for silicic lava formation invoke buoyant magma rise with outgassing during ascent (Eichelberger et al. 1986) Jaupart and Allègre 1991; Westrich and Eichelberger 1994; Cassidy et al. 2018). If this is the case, then it is clear how the H₂O concentrations – and associated viscosities at magmatic temperatures – measured here, evolve through the crust. In these models, H₂O is lost through diffusion into nucleating and growing bubbles, and/or into opening fractures (Eichelberger et al. 1986; Gonnermann and Manga 2003; Castro et al. 2012). Fracturing, shown to have been occurring in the shallow feeder system at Hrafninnuhryggur during lava emplacement in the brittle field (cf. **Fig. 7**; Wadsworth et al. 2018), would serve to further enhance gas escape (Yoshimura and Nakamura 2008; Sano et al. 2015; Lamur et al. 2017). So the vesiculating, frothing, and fracturing rise of rhyolite during drilling is another scenario that should be explored.

In the Wadsworth et al. (2020) model, the majority of H₂O loss from storage to the surface is likely to occur into rapidly growing bubbles prior to and during explosive fragmentation. Upon fragmentation, this H₂O is then liberated into the conduit gas, which separates from the magma and accelerates up and out of the system. Wadsworth et al. (2020) predict that at the fragmentation level (a minimum of 1 km depth), the melt H₂O concentration has already dropped to ~0.5 wt.%. Above this fragmentation point, continued degassing to very low H₂O concentrations is driven by time-dependent diffusive outgassing out of bubbly particles that were formed at fragmentation and which are transported through a relatively low-pressure dusty gas (Wadsworth et al. 2020, 2022b; Weaver et al. 2022). Importantly, this degassing impacts the timescale of sintering (welding) which ultimately shuts the permeable pathways and controls the final concentration of dissolved volatiles in shallow systems (Wadsworth et al. 2021b; Weaver et al. 2023).

We highlight here these different models for rhyolite ascent in the crust on the assumption that future drilling into magma has some conceptual similarities to opening up a conduit to the Earth's surface. For this reason, the general behaviour of rhyolite upon decompression and ascent to the surface requires understanding. Our thermal analysis indicates that the IDDP-1 magma underwent the glass transition (T_g) at ~793 K, and was likely quenched at a rate of 7-80 K.min⁻¹ (see **Fig 5**). Considering storage temperatures of ca. 1123–1193 K, the interval between storage temperature and T_g , and the cooling rate through T_g , we have constrained both a thermal window (of ~400 K), and a very abbreviated timescale (~4–60 minutes) during which magma responds physically and chemically to pressure-temperature perturbations imparted by drilling activity.

7. Closing remarks

We used thermal analysis and several rheological apparatuses to measure the glass transition interval, the cooling rate, the viscosity and the viscoelastic rheological (brittle) limit of Krafla obsidian glass sampled from surficial lava, a shallow dyke, and the drilling mud from IDDP-1. We find that the IDDP-1 glass chips underwent the glass transition at ~793 K, by being quenched at a rate of 7–80 K.min⁻¹, constraining a temperature-time window for physico-chemical perturbation by drilling activity. Rheologically, we use the Hess and Dingwell (1996) model for rhyolites to reproduce the viscosity of the variably hydrous (shallow and deep) rhyolitic magma and demonstrate the weak effect of water on the shear modulus of rhyolitic melts. Our analysis surmises the importance of iron, whose concentration is elevated in Krafla rhyolite, on the potential rheological response of magma to transport or drilling. Finally, our rheological analysis indicates that deformation of aphyric Krafla magma at $Wi \geq 0.04$ will favor a brittle response, and that if partially crystallized (e.g., the felsite capping the magma body) the deformation map provided herein should be valid to model the conditions for viscous flow and fragmentation. We conclude that these rheological constraints on the Krafla rhyolitic magmas at storage and surface conditions should be used in conjunction with simulations of magmatic processes in response to drilling scenarios to provide a scientific basis for hazard assessment and risk mitigation for the KMT project.

Acknowledgments

We are grateful to the wider Krafla Magma Testbed team for their support and to Landsvirkjun in particular. Thanks to Julia Schunke, Francisco Caceres, Holly Unwin, Ed Llewellyn, and Marize Muniz da Silva for general discussion or field assistance. Funding was provided by the European Research Council (834225-EAVESDROP; 101001065-MODERATE) and by the Natural Environment Research Council of UKRI (grant number NE/T007796/1). Yan Lavallée, Jackie Kendrick, and Donald Dingwell acknowledge support from LMUexcellent, funded by the Federal Ministry of Education and Research (BMBF) and the Free State of Bavaria under the Excellence Strategy of the Federal Government and the Länder. BS acknowledges funding from the European Union's Horizon 2020 research and innovation programme under grant agreement No 858092 (MSCA-ETN IMPROVE). We thank the landowners at Hrafninnuhryggur. Two reviewers and the editor Shane Cronin all helped to improve the manuscript.

References cited

- Baker DR (1996) Granitic melt viscosities: Empirical and configurational entropy models for their calculation. *Am Mineral* 81:126–134. <https://doi.org/10.2138/AM-1996-1-216/PDF>
- Beyreuther M, Barsch R, Krischer L, et al (2010) ObsPy: A Python Toolbox for Seismology. *Seismol Res Lett* 81:530–533. <https://doi.org/10.1785/GSSRL.81.3.530>
- Bindeman IN, Hudak MR, Palandri JP, et al (2021) Rhyolitic and basaltic reference materials for TC/EA analysis: Investigation of water extraction and D/H ratios. *Chem Geol* 583:120486. <https://doi.org/https://doi.org/10.1016/j.chemgeo.2021.120486>
- Blower JD, Mader HM, Wilson SDR (2001) Coupling of viscous and diffusive controls on bubble growth during explosive volcanic eruptions. *Earth Planet Sci Lett* 193:47–56. [https://doi.org/https://doi.org/10.1016/S0012-821X\(01\)00488-5](https://doi.org/https://doi.org/10.1016/S0012-821X(01)00488-5)
- Blundy J, Cashman K, Humphreys M (2006) Magma heating by decompression-driven crystallization beneath andesite volcanoes. *Nature* 443:76–80. <https://doi.org/10.1038/nature05100>
- Branney MJ, Kokelaar P (1992) A reappraisal of ignimbrite emplacement: progressive aggradation and changes from particulate to non-particulate flow during emplacement of high-grade ignimbrite. *Bull Volcanol* 54:504–520. <https://doi.org/10.1007/BF00301396>
- Burnham CW (1964) Viscosity of a H₂O rich pegmatite melt at high pressure. *Geol Soc Am Spec Pap* 76:26
- Cáceres F, Hess K-U, Eitel M, et al (2024) Oxide nanolitisation-induced melt iron extraction causes viscosity jumps and enhanced explosivity in silicic magma. *Nat Commun* 15:604. <https://doi.org/10.1038/s41467-024-44850-x>
- Cáceres F, Scheu B, Hess K-U, et al (2021) From melt to crystals: The effects of cooling on FeTi oxide nanolites crystallisation and melt polymerisation at oxidising conditions. *Chem Geol* 563:120057. <https://doi.org/https://doi.org/10.1016/j.chemgeo.2021.120057>
- Cáceres F, Wadsworth FB, Scheu B, et al (2020) Can nanolites enhance eruption explosivity? *Geology* 48:997–1001. <https://doi.org/10.1130/G47317.1>
- Casas AS, Wadsworth FB, Ayris PM, et al (2019) SO₂ scrubbing during percolation through rhyolitic volcanic domes. *Geochim Cosmochim Acta*. <https://doi.org/10.1016/j.gca.2019.04.013>
- Cassidy M, Manga M, Cashman K, Bachmann O (2018) Controls on explosive-effusive volcanic eruption styles. *Nat Commun* 9:2839. <https://doi.org/10.1038/s41467-018-05293-3>
- Castro JM, Cordonnier B, Tuffen H, et al (2012) The role of melt-fracture degassing in defusing explosive rhyolite eruptions at volcán Chaitén. *Earth Planet Sci Lett* 333–334:63–69. <https://doi.org/https://doi.org/10.1016/j.epsl.2012.04.024>
- Castro JM, Cottrell E, Tuffen H, et al (2009) Spherulite crystallization induces Fe-redox redistribution in silicic melt. *Chem Geol* 268:272–280.

<https://doi.org/https://doi.org/10.1016/j.chemgeo.2009.09.006>

- Castro JM, Dingwell DB (2009) Rapid ascent of rhyolitic magma at Chaitén volcano, Chile. *Nature* 461:780–783. <https://doi.org/10.1038/nature08458>
- Chevrel MO, Baratoux D, Hess K-U, Dingwell DB (2014) Viscous flow behavior of tholeiitic and alkaline Fe-rich martian basalts. *Geochim Cosmochim Acta* 124:348–365. <https://doi.org/https://doi.org/10.1016/j.gca.2013.08.026>
- Coats R, Kendrick JE, Wallace PA, et al (2018) Failure criteria for porous dome rocks and lavas: A study of Mt. Unzen, Japan. *Solid Earth* 9:1299–1328. <https://doi.org/10.5194/se-9-1299-2018>
- Cordonnier B, Caricchi L, Pistone M, et al (2012a) The viscous-brittle transition of crystal-bearing silicic melt: Direct observation of magma rupture and healing. *Geology* 40:611–614. <https://doi.org/10.1130/G3914.1>
- Cordonnier B, Caricchi L, Pistone M, et al (2012b) The viscous-brittle transition of crystal-bearing silicic melt: Direct observation of magma rupture and healing. *Geology* 40:611–614. <https://doi.org/10.1130/G3914.1>
- Cordonnier B, Schmalholz SM, Hess KU, Dingwell DB (2012c) Viscous heating in silicate melts: An experimental and numerical comparison. *J Geophys Res Solid Earth* 117:B02203. <https://doi.org/10.1029/2010JB007982>
- Costa A, Melnik O, Vedeneva E (2007) Thermal effects during magma ascent in conduits. *J Geophys Res Solid Earth* 112:B12205. <https://doi.org/10.1029/2007JB004985>
- Coumans JPP, Llewellyn EWW, Wadsworth FBB, et al (2020) An experimentally validated numerical model for bubble growth in magma. *J Volcanol Geotherm Res* 402:107002. <https://doi.org/https://doi.org/10.1016/j.jvolgeores.2020.107002>
- Debolt MA, Easteal AJ, Macedo PB, Moynihan CT (1976) Analysis of Structural Relaxation in Glass Using Rate Heating Data. *J Am Ceram Soc* 59:16–21. <https://doi.org/https://doi.org/10.1111/j.1151-2916.1976.tb09377.x>
- Di Genova D, A. BR, M. MH, et al (2020) In situ observation of nanolite growth in volcanic melt: A driving force for explosive eruptions. *Sci Adv* 6:eabb0413. <https://doi.org/10.1126/sciadv.abb0413>
- Di Genova D, Caracciolo A, Kolzenburg S (2018) Measuring the degree of “nanotilization” of volcanic glasses: Understanding syn-eruptive processes recorded in melt inclusions. *Lithos* 318–319:209–218. <https://doi.org/https://doi.org/10.1016/j.lithos.2018.08.011>
- Di Genova D, Kolzenburg S, Wiesmaier S, et al (2017) A compositional tipping point governing the mobilization and eruption style of rhyolitic magma. *Nature* 552:235–238. <https://doi.org/10.1038/nature24488>
- Dingwell DB (1989) Shear viscosities of ferrosilicate liquids. *Am Mineral* 74:1038–1044
- Dingwell DB (1991) Redox viscometry of some Fe-bearing silicate melts. *Am Mineral* 76:1560–1562
- Dingwell DB, Romano C, Hess KU (1996) The effect of water on the viscosity of a haplogranitic melt under P-T-X conditions relevant to silicic volcanism. *Contrib to Mineral Petrol* 124:19–28. <https://doi.org/10.1007/S004100050170>
- Dingwell DB, Virgo D (1988) Viscosities of melts in the Na₂OFeOFe₂O₃SiO₂ system and factors controlling relative viscosities of fully polymerized silicate melts. *Geochim Cosmochim Acta* 52:395–403. [https://doi.org/10.1016/0016-7037\(88\)90095-6](https://doi.org/10.1016/0016-7037(88)90095-6)
- Dingwell DB, Webb SL (1989) Structural relaxation in silicate melts and non-Newtonian melt rheology in geologic processes. *Phys Chem Miner* 16:508–516
- Dorfman A, Hess K-U, Dingwell D (1996) Centrifuge-assisted falling-sphere viscometry. *Eur J Mineral* 8:507–514
- Eichelberger J (2019) Planning an International Magma Observatory. *Eos (Washington DC)* 100:.

<https://doi.org/10.1029/2019eo125255>

- Eichelberger JC, Carrigan CR, Westrich HR, Price RH (1986) Non-explosive silicic volcanism. *Nature* 323:598–602. <https://doi.org/10.1038/323598a0>
- Elders WA, Friðleifsson GÓ, Zierenberg RA, et al (2011) Origin of a rhyolite that intruded a geothermal well while drilling at the Krafla volcano, Iceland. *Geology* 39:231–234. <https://doi.org/10.1130/G31393.1>
- Fink JH (1983) Structure and emplacement of a rhyolitic obsidian flow: Little Glass Mountain, Medicine Lake Highland, northern California. *Geol Soc Am Bull* 94:362–380
- Foster A, Wadsworth FB, Tuffen H, et al (2024) Evidence for the formation of silicic lava by pyroclast sintering. *Nat Commun* 15:5347. <https://doi.org/10.1038/s41467-024-49601-6>
- Friðleifsson G, ... BP-P of the, 2010 undefined (2010) Iceland Deep Drilling Project. The first IDDP drill hole drilled and completed in 2009. *geothermal-energy.org* 25–29
- Friedman I, Long W, Smith RL (1963) Viscosity and water content of rhyolite glass. *J Geophys Res* 68:6523–6535
- Gent AN (1960) Theory of the parallel plate viscometer. *Br J Appl Phys* 11:85
- Giordano D, Russell JK, Dingwell DB (2008) Viscosity of magmatic liquids: a model. *Earth Planet Sci Lett* 271:123–134
- Gonnermann HM, Manga M (2003) Explosive volcanism may not be an inevitable consequence of magma fragmentation. *Nature* 426:432–435
- Gottsmann J, Giordano D, Dingwell DB (2002) Predicting shear viscosity during volcanic processes at the glass transition: a calorimetric calibration. *Earth Planet Sci Lett* 198:417–427. [https://doi.org/https://doi.org/10.1016/S0012-821X\(02\)00522-8](https://doi.org/https://doi.org/10.1016/S0012-821X(02)00522-8)
- Hampton RL, Bindeman IN, Stern RA, et al (2021) A microanalytical oxygen isotopic and U-Th geochronologic investigation and modeling of rhyolite petrogenesis at the Krafla Central Volcano, Iceland. *J Volcanol Geotherm Res* 414:107229. <https://doi.org/https://doi.org/10.1016/j.jvolgeores.2021.107229>
- Hess K-U, Cordonnier B, Lavallée Y, Dingwell DB (2007) High-load, high-temperature deformation apparatus for synthetic and natural silicate melts. *Rev Sci Instrum* 78:75102–75104. <https://doi.org/10.1063/1.2751398>
- Hess K-U, Dingwell DB, Webb SL (1995) The influence of excess alkalis on the viscosity of a haplogranitic melt. *Am Mineral* 80:297–304. <https://doi.org/10.2138/AM-1995-3-412>
- Hess K-UU, Dingwell DB (1996) Viscosities of hydrous leucogranitic melts: A non-Arrhenian model. *Am Mineral* 81:1297–1300
- Hodge IM (2008) A Personal Account of Developments in Enthalpy Relaxation: A Tribute to C. T. Moynihan. *J Am Ceram Soc* 91:766–772. <https://doi.org/https://doi.org/10.1111/j.1551-2916.2007.02127.x>
- Ilic O, Sigmundsson F, Lavallée Y, et al (2020) Geological Risk Associated with Drilling into Magma at Krafla Caldera, Iceland: Preliminary Evaluation. In: *Proceedings World Geothermal Congress 2020*
- Ingason K, Kristjánsson V, Einarsson K (2014) Design and development of the discharge system of IDDP-1. *Geothermics* 49:58–65. <https://doi.org/https://doi.org/10.1016/j.geothermics.2013.05.002>
- Jaupart C, Allègre CJ (1991) Gas content, eruption rate and instabilities of eruption regime in silicic volcanoes. *Earth Planet Sci Lett* 102:413–429. [https://doi.org/https://doi.org/10.1016/0012-821X\(91\)90032-D](https://doi.org/https://doi.org/10.1016/0012-821X(91)90032-D)
- Jónasson K (1994) Rhyolite volcanism in the Krafla central volcano, north-east Iceland. *Bull Volcanol* 56:516–528. <https://doi.org/10.1007/BF00302832>

- Kemmer G, Keller S (2010) Nonlinear least-squares data fitting in Excel spreadsheets. *Nat Protoc* 5:267–281. <https://doi.org/10.1038/nprot.2009.182>
- Kenderes SM, Whittington AG (2021) Faster geospeedometry: A Monte Carlo approach to relaxational geospeedometry for determining cooling rates of volcanic glasses. *Chem Geol* 581:120385. <https://doi.org/https://doi.org/10.1016/j.chemgeo.2021.120385>
- Kendrick JE, Lavallée Y (2022) Frictional Melting in Magma and Lava. *Rev Mineral Geochemistry* 87:919–963. <https://doi.org/10.2138/rmg.2022.87.20>
- Kendrick JE, Lavallée Y, Hess KU, et al (2013) Tracking the permeable porous network during strain-dependent magmatic flow. *J Volcanol Geotherm Res* 260:117–126. <https://doi.org/10.1016/j.jvolgeores.2013.05.012>
- Kohlrausch R (1854) Theorie des elektrischen Rückstandes in der Leidener Flasche. *Ann Phys* 167:179–214
- La Spina G, Arzilli F, Llewellyn EW, et al (2021) Explosivity of basaltic lava fountains is controlled by magma rheology, ascent rate and outgassing. *Earth Planet Sci Lett* 553:116658. <https://doi.org/https://doi.org/10.1016/j.epsl.2020.116658>
- Lamur A, Kendrick JE, Eggertsson GH, et al (2017) The permeability of fractured rocks in pressurised volcanic and geothermal systems. *Sci Rep* 7:6173. <https://doi.org/10.1038/s41598-017-05460-4>
- Lavallée Y, Benson PM, Heap MJ, et al (2013) Reconstructing magma failure and the degassing network of domebuilding eruptions. *Geology* 41:515–518. <https://doi.org/10.1130/G33948.1>
- Lavallée Y, Dingwell DB, Johnson JB, et al (2015a) Thermal vesiculation during volcanic eruptions. *Nature* 528:544–547. <https://doi.org/10.1038/nature16153>
- Lavallée Y, Hess K-U, Cordonnier B, Dingwell DB (2007) Non-Newtonian rheological law for highly crystalline dome lavas. *Geology* 35:843–846. <https://doi.org/10.1130/g23594a.1>
- Lavallée Y, Kendrick JE, Eichelberger JC, et al Accessing magma: a necessary revolution in Earth sciences and renewable energies. *Eur Rev*
- Lavallée Y, Meredith PG, Dingwell DB, et al (2008) Seismogenic lavas and explosive eruption forecasting. *Nature* 453:507–510. <https://doi.org/10.1038/nature06980>
- Lavallée Y, Wadsworth FB, Vasseur J, et al (2015b) Eruption and emplacement timescales of ignimbrite super-eruptions from thermo-kinetics of glass shards. *Front Earth Sci* 3:2. <https://doi.org/10.3389/feart.2015.00002>
- Lowenstern JB, Pitcher BW (2013) Analysis of H₂O in silicate glass using attenuated total reflectance (ATR) micro-FTIR spectroscopy‡. *Am Mineral* 98:1660–1668. <https://doi.org/10.2138/am.2013.4466>
- Mader HM, Llewellyn EW, Mueller SP (2013) The rheology of two-phase magmas: A review and analysis. *J Volcanol Geotherm Res* 257:135–158. <https://doi.org/https://doi.org/10.1016/j.jvolgeores.2013.02.014>
- Maier CG, Kelley KK (1932) An equation for the representation of high-temperature heat content data. *J Am Chem Soc* 54:3243–3246. <https://doi.org/10.1021/ja01347a029>
- Malfait WJ, Sanchez-Valle C, Ardia P, et al (2011) Compositional dependent compressibility of dissolved water in silicate glasses. 96:1402–1409. <https://doi.org/doi:10.2138/am.2011.3718>
- Masotta M, Mollo S, Nazzari M, et al (2018) Crystallization and partial melting of rhyolite and felsite rocks at Krafla volcano: A comparative approach based on mineral and glass chemistry of natural and experimental products. *Chem Geol* 483:603–618. <https://doi.org/https://doi.org/10.1016/j.chemgeo.2018.03.031>
- Mastin LG (2005) The controlling effect of viscous dissipation on magma flow in silicic conduits. *J Volcanol Geotherm Res* 143:17–28. <https://doi.org/https://doi.org/10.1016/j.jvolgeores.2004.09.008>

- Mortensen AK, Grönvold K, Gudmundsson Á, et al (2010) Quenched silicic glass from well KJ-39 in Krafla, North-Eastern Iceland. In: World Geothermal Congress. pp 1–6
- Moussallam Y, Morizet Y, Gaillard F (2016) H₂O–CO₂ solubility in low SiO₂-melts and the unique mode of kimberlite degassing and emplacement. *Earth Planet Sci Lett* 447:151–160. <https://doi.org/https://doi.org/10.1016/j.epsl.2016.04.037>
- Mujin M, Nakamura M, Miyake A (2017) Eruption style and crystal size distributions: Crystallization of groundmass nanolites in the 2011 Shinmoedake eruption. *Am Mineral* 102:2367–2380. <https://doi.org/10.2138/AM-2017-6052CCBYNCND>
- Namiki A, Okumura S, Goto A, Yamada T (2023) In situ observation of glass-like fragmentation of high-temperature silicate melts generating fine ashes. *Commun Earth Environ* 4:155. <https://doi.org/10.1038/s43247-023-00816-3>
- Okumura S, Uesugi K, Goto A, et al (2022) Rheology of nanocrystal-bearing andesite magma and its roles in explosive volcanism. *Commun Earth Environ* 3:241. <https://doi.org/10.1038/s43247-022-00573-9>
- Pálsson B, Hólmgeirsson S, Guðmundsson Á, et al (2014) Drilling of the well IDDP-1. *Geothermics* 49:23–30. <https://doi.org/https://doi.org/10.1016/j.geothermics.2013.08.010>
- Pereira L, Linard Y, Wadsworth FB, et al (2024) The rheological response of magma to nanolitisation. *J Volcanol Geotherm Res* 108039. <https://doi.org/https://doi.org/10.1016/j.jvolgeores.2024.108039>
- Persikov ES, Zharikov VA, Bukhtiyarov PG (1990) The effect of volatiles on the properties of magmatic melts. *Eur J Mineral* 621–642. <https://doi.org/10.1127/EJM/2/5/0621>
- Petcovic HL, Dufek JD (2005) Modeling magma flow and cooling in dikes: Implications for emplacement of Columbia River flood basalts. *J Geophys Res Solid Earth* 110:. <https://doi.org/https://doi.org/10.1029/2004JB003432>
- Pistone M, Caricchi L, Ulmer P, et al (2012) Deformation experiments of bubble- and crystal-bearing magmas: Rheological and microstructural analysis. *J Geophys Res Solid Earth* 117:. <https://doi.org/https://doi.org/10.1029/2011JB008986>
- Pocklington HC (1940) Rough measurement of high viscosities. *Math Proc Cambridge Philos Soc* 36:507–508. <https://doi.org/10.1017/S0305004100017564>
- Romine WL, Whittington AG (2015) A simple model for the viscosity of rhyolites as a function of temperature, pressure and water content. *Geochim Cosmochim Acta* 170:281–300. <https://doi.org/https://doi.org/10.1016/j.gca.2015.08.009>
- Rooyackers SM, Stix J, Berlo K, et al (2021a) Eruption risks from covert silicic magma bodies. *Geology* 49:921–925. <https://doi.org/10.1130/G48697.1>
- Rooyackers SM, Stix J, Berlo K, et al (2021b) The Origin of Rhyolitic Magmas at Krafla Central Volcano (Iceland). *J Petrol* 62:. <https://doi.org/10.1093/petrology/egab064>
- Rooyackers SM, Stix J, Berlo K, Barker SJ (2020) Emplacement of unusual rhyolitic to basaltic ignimbrites during collapse of a basalt-dominated caldera: The Halarauður eruption, Krafla (Iceland). *GSA Bull* 132:1881–1902. <https://doi.org/10.1130/B35450.1>
- Rule G (2020) The origin of magma encountered during drilling of geothermal well KJ-39, Krafla, Iceland and the relationship with the nearby IDDP-1 magma. University of Canterbury (pp 127)
- Ryan AG, Russell JK, Hess K-U, et al (2015a) Vesiculation in rhyolite at low H₂O contents: A thermodynamic model. *Geochemistry, Geophys Geosystems* n/a-n/a. <https://doi.org/10.1002/2015GC006024>
- Ryan AG, Russell JK, Nichols ARL, et al (2015b) Experiments and models on H₂O retrograde solubility in volcanic systems. *Am Mineral* 100:774–786. <https://doi.org/10.2138/AM-2015-5030>
- Sæmundsson K, Hjartarson Á, Kaldal I, et al (2012) Geological map of the Northern volcanic zone,

Iceland, Northern part. Icel Geosurvey Landsvirkjun, scale 1:

- Sæmundsson K, Pringle MS, Hardarson BS (2000) About the age of strata in the Krafla volcanic system. In: Proceedings of the Geoscience Society of Iceland, Spring Meeting. pp 26–27
- Sano K, Wada K, Sato E (2015) Rates of water exsolution and magma ascent inferred from microstructures and chemical analyses of the Tokachi–Ishizawa obsidian lava, Shirataki, northern Hokkaido, Japan. *J Volcanol Geotherm Res* 292:29–40. <https://doi.org/https://doi.org/10.1016/j.jvolgeores.2014.11.015>
- Saubin E, Kennedy B, Tuffen H, et al (2021) Textural and geochemical window into the IDDP-1 rhyolitic melt, Krafla, Iceland, and its reaction to drilling. 133:1815–1830. <https://doi.org/10.1130/B35598.1>
- Saubin E, Kennedy B, Tuffen H, et al (2019) Comparative field study of shallow rhyolite intrusions in Iceland: emplacement mechanisms and impact on country rocks. *J Volcanol Geotherm Res* 388:106691. <https://doi.org/10.1016/j.jvolgeores.2019.106691>
- Scaillet B, Holtz F, Pichavant M, Schmidt M (1996) Viscosity of Himalayan leucogranites: Implications for mechanisms of granitic magma ascent. *J Geophys Res Solid Earth* 101:27691–27699. <https://doi.org/https://doi.org/10.1029/96JB01631>
- Schawe JEK, Hess K-U (2019) The kinetics of the glass transition of silicate glass measured by fast scanning calorimetry. *Thermochim Acta* 677:85–90
- Schulze F, Behrens H, Holtz F, et al (1996) The influence of H₂O on the viscosity of a haplogranitic melt. *Am Mineral* 81:1155–1165. <https://doi.org/10.2138/AM-1996-9-1014/PDF>
- Seropian G, Kennedy BM, Kendrick JE, et al (2022) Vesiculation of rhyolitic melts under oscillatory pressure. *Front Earth Sci* 219. <https://doi.org/10.3389/FEART.2022.812311>
- Shaw HR (1963) Obsidian-H₂O viscosities at 1000 and 2000 bars in the temperature range 700° to 900°C. *J Geophys Res* 68:6337–6343. <https://doi.org/https://doi.org/10.1029/JZ068i023p06337>
- Sipp A, Richet P (2002) Equivalence of volume, enthalpy and viscosity relaxation kinetics in glass-forming silicate liquids. *J Non Cryst Solids* 298:202–212. [https://doi.org/https://doi.org/10.1016/S0022-3093\(02\)00948-1](https://doi.org/https://doi.org/10.1016/S0022-3093(02)00948-1)
- Sparks RSJ (1978) The dynamics of bubble formation and growth in magmas: A review and analysis. *J Volcanol Geotherm Res* 3:1–37. [https://doi.org/https://doi.org/10.1016/0377-0273\(78\)90002-1](https://doi.org/https://doi.org/10.1016/0377-0273(78)90002-1)
- Tobolsky A V., Taylor RB (1963) VISCOELASTIC PROPERTIES OF A SIMPLE ORGANIC GLASS. *J Phys Chem* 67:2439–2442. <https://doi.org/10.1021/j100805a044>
- Tuffen H, Castro JM (2009) The emplacement of an obsidian dyke through thin ice: Hrafninnuhryggur, Krafla Iceland. *J Volcanol Geotherm Res* 185:352–366
- Tuffen H, Owen J, Denton J (2010) Magma degassing during subglacial eruptions and its use to reconstruct palaeo-ice thicknesses. *Earth-Science Rev* 99:1–18. <https://doi.org/https://doi.org/10.1016/j.earscirev.2010.01.001>
- Tuffen H, Smith R, Sammonds PR (2008) Evidence for seismogenic fracture of silicic magma. *Nature* 453:511–514. <https://doi.org/10.1038/nature06989>
- Vasseur J, Wadsworth FB, Dingwell DB (2018) Forecasting Multiphase Magma Failure at the Laboratory Scale Using Acoustic Emission Data. *Front Earth Sci* 6:132. <https://doi.org/10.3389/feart.2018.00132>
- Vasseur J, Wadsworth FB, Dingwell DB (2023) Shear thinning and brittle failure in crystal-bearing magmas arise from local non-Newtonian effects in the melt. *Earth Planet Sci Lett* 603:117988. <https://doi.org/https://doi.org/10.1016/j.epsl.2023.117988>
- Vasseur J, Wadsworth FB, Lavallée Y, et al (2015) Heterogeneity: The key to failure forecasting. *Sci Rep* 5:13259. <https://doi.org/10.1038/srep13259>
- Wadsworth F Ben, Llewellyn E, Rennie C, et al (2022a) Using obsidian in glass art practice.

Volcanica 5:183–207. <https://doi.org/10.30909/vol.05.01.183207>

- Wadsworth F, Vasseur J, Casas A, et al (2021a) A model for the kinetics of high temperature reactions between polydisperse volcanic ash and SO₂ gas. *Am Mineral.* <https://doi.org/10.2138/am-2021-7691>
- Wadsworth FB, Llewellyn EW, Castro JM, et al (2022b) A reappraisal of explosive–effusive silicic eruption dynamics: syn-eruptive assembly of lava from the products of cryptic fragmentation. *J Volcanol Geotherm Res* 107672. <https://doi.org/https://doi.org/10.1016/j.jvolgeores.2022.107672>
- Wadsworth FB, Llewellyn EW, Vasseur J, et al (2020) Explosive-effusive volcanic eruption transitions caused by sintering. *Sci Adv* 6:eaba7940. <https://doi.org/10.1126/sciadv.aba7940>
- Wadsworth FB, Vasseur J, Heap MJ, et al (2024) A scaling for the viscous-brittle transition in flowing crystal-bearing volcanic dome lavas with implications for the development of permeability anisotropy. *J Volcanol Geotherm Res* (in Rev)
- Wadsworth FB, Vasseur J, Llewellyn EW, et al (2021b) A model for permeability evolution during volcanic welding. *J Volcanol Geotherm Res* 409:107118. <https://doi.org/https://doi.org/10.1016/j.jvolgeores.2020.107118>
- Wadsworth FB, Vasseur J, Schaubert J, et al (2019) A general model for welding of ash particles in volcanic systems validated using in situ X-ray tomography. *Earth Planet Sci Lett* 525:115726. <https://doi.org/https://doi.org/10.1016/j.epsl.2019.115726>
- Wadsworth FB, Witcher T, Vossen CEJ, et al (2018) Combined effusive-explosive silicic volcanism straddles the multiphase viscous-to-brittle transition. *Nat Commun* 9:1–8. <https://doi.org/10.1038/s41467-018-07187-w>
- Watson T (2018) Evolution of magmatic volatiles during drilling into a magma body, Krafla, Iceland. University of Canterbury (pp 129)
- Weaver J, Lamur A, Lea TD, et al (2023) Sintering of vesiculating pyroclasts. *Earth Planet Sci Lett* 623:118410. <https://doi.org/https://doi.org/10.1016/j.epsl.2023.118410>
- Weaver J, Lavallée Y, Ashraf M, et al (2022) Vesiculation and densification of pyroclasts: A clast-size dependent competition between bubble growth and diffusive outgassing. *J Volcanol Geotherm Res* 107550. <https://doi.org/https://doi.org/10.1016/j.jvolgeores.2022.107550>
- Webb SL, Dingwell DB (1990) Non-Newtonian rheology of igneous melts at high stresses and strain rates: Experimental results for rhyolite, andesite, basalt, and nephelinite. *J Geophys Res* 95:15695–15701
- Weidendorfer D, Hess K-U, Ruhekenya RM, et al (2023) Effect of water on the glass transition of a potassium-magnesium carbonate melt. *Philos Trans R Soc A Math Phys Eng Sci* 381:20220355. <https://doi.org/10.1098/rsta.2022.0355>
- Westrich HR, Eichelberger JC (1994) Gas transport and bubble collapse in rhyolitic magma: an experimental approach. *Bull Volcanol* 56:447–458. <https://doi.org/10.1007/BF00302826>
- Whittington AG, Richet P, Polian A (2012) Amorphous materials: Properties, structure, and durability. Water compressibility Silic Glas A Brillouin Spectrosc study 97:455–467. <https://doi.org/doi:10.2138/am.2012.3891>
- Wilding M, Webb S, Dingwell DB (1996) Tektite cooling rates: calorimetric relaxation geospeedometry applied to a natural glass. *Geochim Cosmochim Acta* 60:1099–1103
- Williams G, Watts DC (1970) Non-symmetrical dielectric relaxation behaviour arising from a simple empirical decay function. *Trans Faraday Soc* 66:80–85
- Wright FE (1915) Obsidian from Hrafninnuhryggur, Iceland: its lithopliysæ. and surface markings. *GSA Bull* 26:255–286. <https://doi.org/10.1130/GSAB-26-255>
- Yoshimura S, Nakamura M (2008) Diffusive dehydration and bubble resorption during open-system degassing of rhyolitic melts. *J Volcanol Geotherm Res* 178:72–80.

<https://doi.org/https://doi.org/10.1016/j.jvolgeores.2008.01.017>

Zandonà A, Scarani A, Löschmann J, et al (2023) Non-stoichiometric crystal nucleation in a spodumene glass containing TiO₂ as seed former: Effects on the viscosity of the residual melt. *J Non Cryst Solids* 619:122563. <https://doi.org/https://doi.org/10.1016/j.jnoncrysol.2023.122563>

Zierenberg RA, Schiffman P, Barfod GH, et al (2013) Composition and origin of rhyolite melt intersected by drilling in the Krafla geothermal field, Iceland. *Contrib to Mineral Petrol* 165:327–347. <https://doi.org/10.1007/s00410-012-0811-z>

Table 1 Average renormalized composition of IDDP-1 and Hraftinnuhryggur

Oxide*	IDDP-1 (n=295)	Standard deviation	Hraftinnuhryggur (n=15)	Standard deviation
SiO ₂	77.02	2.81	75.03	0.35
TiO ₂	0.3	0.07	0.24	0.02
Al ₂ O ₃	11.78	1.44	12.33	0.18
FeO _(T) **	2.68	0.56	3.25	0.19
MnO	0.07	0.03	0.14	0.04
MgO	0.19	0.07	0.09	0.02
CaO	1.32	0.44	1.69	0.06
Na ₂ O	3.33	0.43	4.48	0.19
K ₂ O	3.31	0.83	2.75	0.08
Mol. fraction excess cations [#]	0.0256		0.0387	
Anhydrous shift factor, c (Pa.K) ⁺	1.43×10^{10}		1.21×10^{10}	
Reference sources	Zierenberg et al. (2013); Masotta et al. (2018); Saubin et al. (2021)		Tuffen & Castro (2009); Rooyakkers et al. (2021)	

*Composition is renormalized to 100% total on an anhydrous basis after taking the average for each oxide

**All iron is assumed to be FeO

[#]Cations excess to charge balancing roles

⁺Computed via Gottsmann et al. (2001)

Table 2. Viscometry data for Krafla rhyolites			
Sample	Measurement type	Temperature (K)*	Viscosity (Pa.s)
IDDP-1	Differential scanning calorimetry	772	1.72E+11
IDDP-1	Differential scanning calorimetry	782	8.60E+10
IDDP-1	Differential scanning calorimetry	805	3.44E+10
Hrafninnuhryggur	Differential scanning calorimetry	1004	7.28E+10
Hrafninnuhryggur	Differential scanning calorimetry	1007	4.86E+10
Hrafninnuhryggur	Differential scanning calorimetry	1026	3.17E+10
Hrafninnuhryggur	Differential scanning calorimetry	1031	2.80E+10
Hrafninnuhryggur	Differential scanning calorimetry	1034	2.60E+10
Hrafninnuhryggur	Differential scanning calorimetry	1034	2.43E+10
Hrafninnuhryggur	Rotational rheometry	1724	5.13E+03
Hrafninnuhryggur	Rotational rheometry	1741	4.37E+03
Hrafninnuhryggur	Rotational rheometry	1758	3.24E+03
Hrafninnuhryggur	Rotational rheometry	1778	2.24E+03
Hrafninnuhryggur	Micropenetration	1053	1.58E+10
Hrafninnuhryggur	Micropenetration	1073	8.13E+09
Hrafninnuhryggur	Micropenetration	1093	3.47E+09
Hrafninnuhryggur	Micropenetration	1033	5.75E+10
Hrafninnuhryggur	Uniaxial compression	993	8.93E+10
Hrafninnuhryggur	Uniaxial compression	993	7.08E+11
Hrafninnuhryggur	Uniaxial compression	1013	4.31E+11
Hrafninnuhryggur	Uniaxial compression	1053	1.93E+10
Hrafninnuhryggur	Uniaxial compression	1053	4.46E+10
Hrafninnuhryggur	Uniaxial compression	1038	3.89E+10
Hrafninnuhryggur	Uniaxial compression	1094	3.55E+09
Hrafninnuhryggur	Uniaxial compression	1167	3.63E+08
Hrafninnuhryggur	Uniaxial compression	1238	4.79E+07

*The temperature values have an associated uncertainty of ± 1 K.

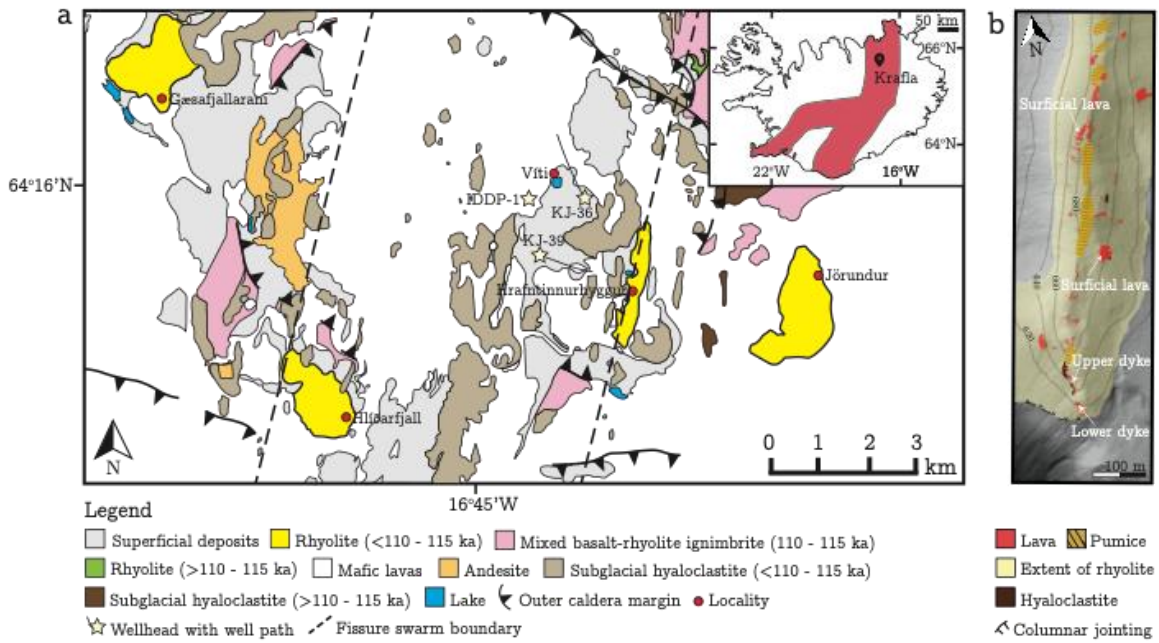


Figure 1. (a) Map of the Krafla volcanic field (Iceland) showing the location of the Hrafninnuhryggur rhyolite, the 2009 IDDP-1 borehole well head (drilled approximately vertically), and the KJ-39 borehole well head (including the slanted projection of the inclined borehole). Additionally shown are other Krafla rhyolites: Víti, Jörundur, Hlíðarfjall, and Gæsafjallaráni. *Inset:* the location of Krafla in the wider Icelandic rift zone(s). This map is simplified from a published source (Sæmundsson et al. 2012). (b) An annotated digital elevation model of the Hrafninnuhryggur ridgeline adapted from Foster et al. (2024) and showing the surficial lava, pumice, and hyaloclastite (country rock) outcrops.

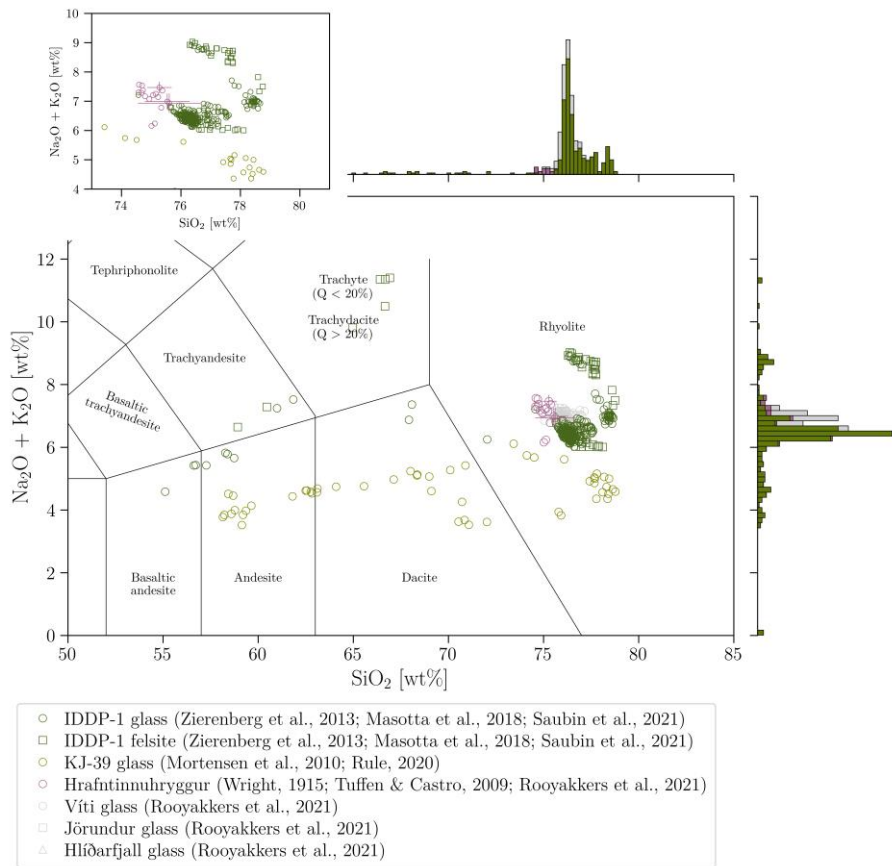


Figure 2. Total-alkali-silica (TAS) plot showing the glass and melt inclusion data available for the rhyolites and borehole glass chips relevant to this study from published sources (Wright 1915; Tuffen and Castro 2009; Mortensen et al. 2010; Zierenberg et al. 2013; Masotta et al. 2018; Rule 2020; Saubin et al. 2021; Rooyakkers et al. 2021b). *Inset:* a zoom-in of the main plot restricted to the rhyolite field and only showing the Hrafninnuhryggur and IDDP-1 datasets, for clarity.

[column width]

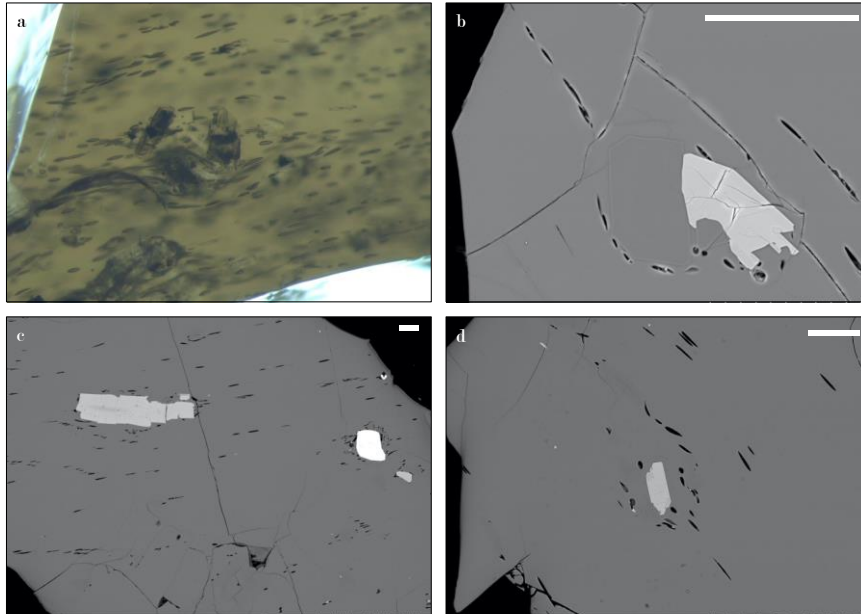


Figure 3. Images of the IDDP-1 glass chip textures. (a) A photomicrograph taken using a binocular microscope and showing deformed vesicles deflected around a local concentration of crystals with a horizontal field of view of 1.6 mm. (b-d) Backscattered electron images showing phenocrysts, groundmass glass, and deformed vesicles. The white scale bar represents 100 μm .

[column width]

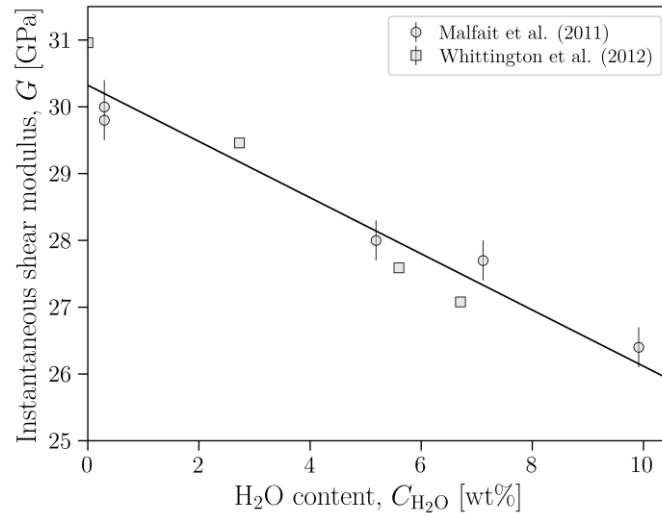


Figure 4. The dependence of the shear modulus of calc-alkaline metaluminous rhyolite melts on H₂O concentrations; circles (Malfait et al. 2011) and squares (Whittington et al. 2012). The linear regression is $G(C_{H_2O}) = b_1 - b_2 C_{H_2O}$ where $b_1 = 30.23$ GPa and $b_2 = 0.42$ and C_{H_2O} is the water content in wt.%.

[column width]

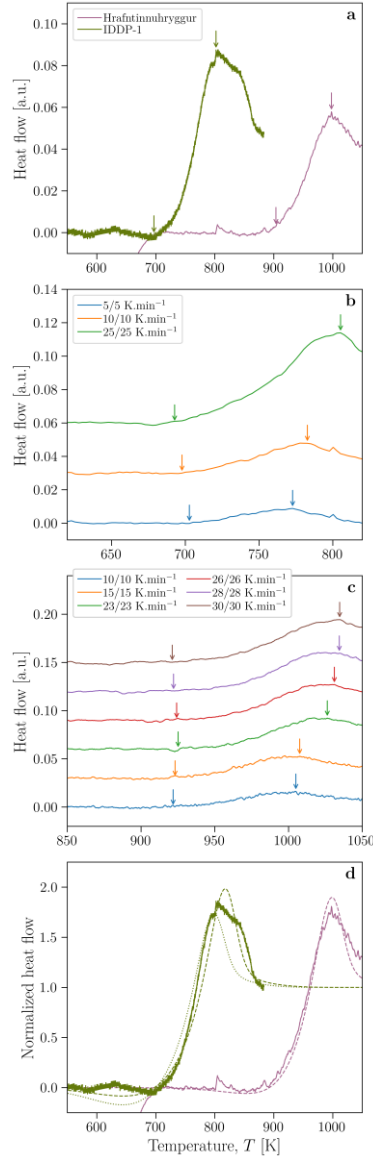


Figure 5. Structural relaxation of IDDP-1 and Hrafninnuhryggur glass chips cast as heat flow (arbitrary units) as a function of temperature as chips are heated at a constant rate. All datasets are baseline-subtracted. (a) The heat flow of an IDDP-1 and a Hrafninnuhryggur glass chip on first heating (heated at 25 K. min^{-1}). For the IDDP-1 signal, we note there is a ‘notch’ on the peak of the glass transition where the arrow is indicating (see panel d). (b) The same IDDP-1 glass chip as used for (a) but here cooled and then reheated at matching rates from 5 K. min^{-1} to 25 K. min^{-1} . In all cases, the onset and peak of the glass transition hump are marked with arrows, found by using a peak-finding algorithm (for the peak) and the intersection of two linear regressions through the curve (for the onset). (c) Heat flow of the same surficial obsidian glass chip from Hrafninnuhryggur as used for (a) at different cooling/heating rate cycles. (d) The same curves as in (a) but here normalized as $(\beta - \beta_g)/(\beta_l - \beta_g)$; see Section 4 for details. The dashed curve fits are the best-fit geospeedometry models (see Section 4b) for cooling rates of 7 K. min^{-1} , for IDDP-1 and Hrafninnuhryggur. The dotted curve on the IDDP-1 signal is the same model but for 80 K. min^{-1} which, by eye, matches the rising signal on the low temperature side of the glass transition peak and appears to better reproduce the ‘notch’ in the peak. This leads us to conclude that $7 - 80 \text{ K. min}^{-1}$ with $\mathcal{O}(50) \text{ K. min}^{-1}$ are reasonable constraints.

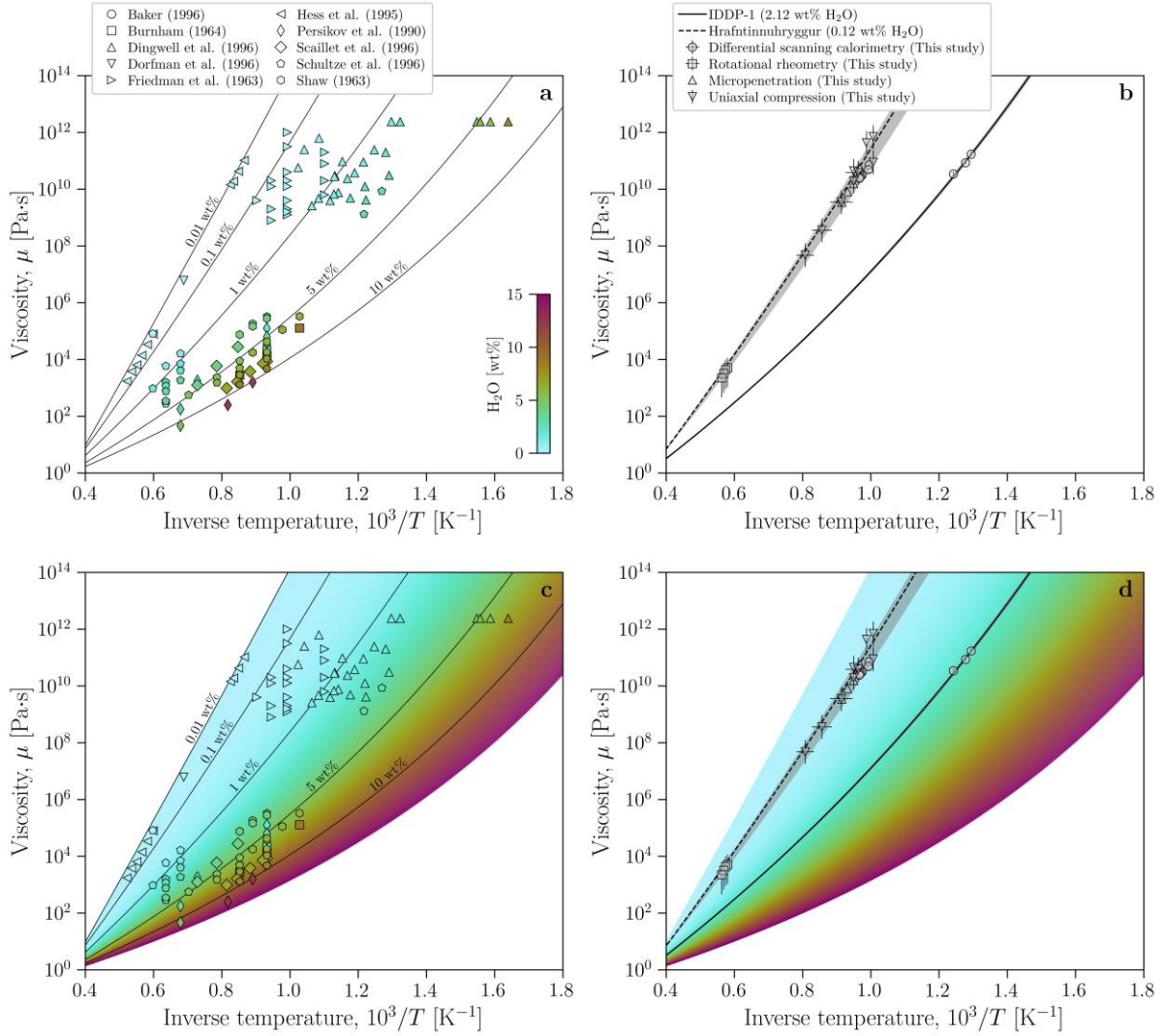


Figure 6. The viscosity of the model rhyolite ‘haplogranite’ system (color-coded) compared with the measured viscosity of the Hrafninnuhryggur rhyolite and IDDP-1 glass chips. (a) The model haplogranite system with data from direct viscometry measurements compiled from published sources (Friedman et al. 1963; Shaw 1963; Burnham 1964; Persikov et al. 1990; Hess et al. 1995; Baker 1996; Dingwell et al. 1996; Schulze et al. 1996; Dorfman et al. 1996; Scaillet et al. 1996) all used to underpin a widely-used rhyolite viscosity model (Hess and Dingwell 1996). Indicative solid curves at chosen water contents 0.01, 0.1, 1, 5, and 10 wt.% are given to help guide the reader. The data symbols are also color-coded in accordance with their measured water content. (b) The same H $_2$ O-dependent rhyolite model as given in (a) but here compared with data from Hrafninnuhryggur (Wadsworth et al. 2022a) and the differential scanning calorimetric constraints provided for IDDP-1 herein (see text). The dashed curve is the Hess and Dingwell (1996) model for 0.12 wt.% H $_2$ O and the solid black curve is the same model for 2.12 wt.% H $_2$ O. The grey band either side of the Hrafninnuhryggur data represents the range of H $_2$ O concentrations measured for Hrafninnuhryggur (upper bound 0.2 wt. %; lower bound 0.1 wt. %; Tuffen and Castro 2009); this band is wider than the uncertainty on the fit for H $_2$ O (± 0.01 wt. %). The grey band either side of the IDDP-1 data represents the Monte Carlo uncertainty (see text) on the best-fit H $_2$ O (± 0.08 wt. %). Panels (c) and (d) are the same as panels (a) and (b), respectively, but with the Hess & Dingwell (1996) model contoured in a continuous color map.

[page width]

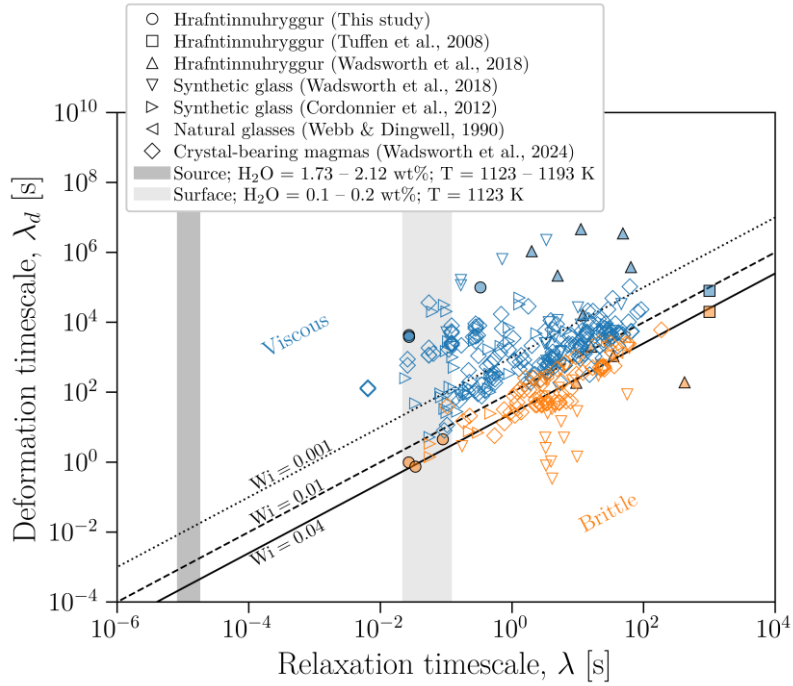


Figure 7. The viscoelastic rheology of rhyolite glass at Krafla, Iceland. We measure the response of samples to deformation at a constant rate of axial strain $\dot{\gamma}$: the response is viscous (blue points) if the evolution of the measured stress evolves smoothly toward an equilibrium value and is brittle (orange points) if there are drops in the stress that are associated with acoustic emissions or audible cracking. Here we compile existing data for synthetic glasses (Cordonnier et al. 2012c; Wadsworth et al. 2018), crystal-bearing glass (Pistone et al. 2012; Cordonnier et al. 2012b), natural glass compositions (Webb and Dingwell 1990), natural dome lavas (Lavallée et al. 2007, 2013; Kendrick et al. 2013; Coats et al. 2018), and Hrafninnuhryggur lavas (Tuffen et al. 2008; Wadsworth et al. 2018). The black curves represent a constant ratio (termed a Weissenberg number Wi) between the deformation timescale and the relaxation timescale of $Wi = 0.04$ (dotted line), $Wi = 0.01$ (dash line), and $Wi = 0.001$ (solid line) (see text). The vertical zones represent the estimated conditions of λ for lava emplacement (labelled ‘surface’) and IDDP-1 (labelled ‘source’ and informed by our rheology estimates; Figs 4 & 5).

[column width]

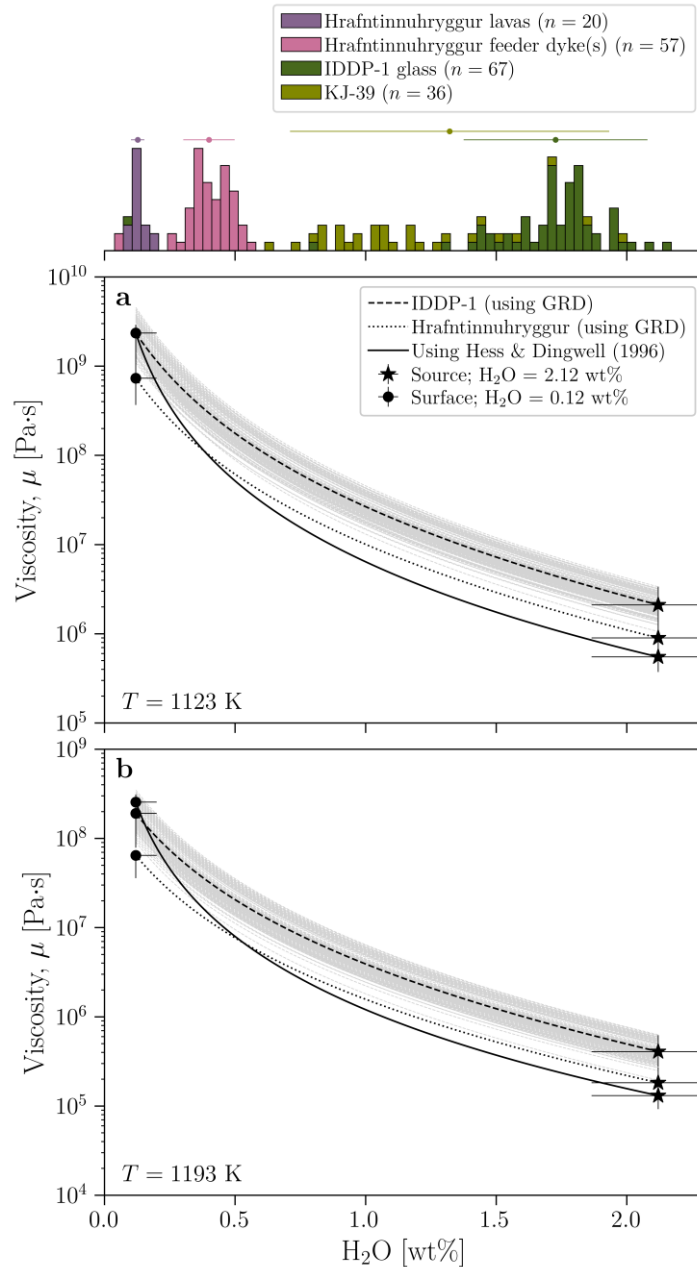


Figure 8. The relationship between the computed viscosity μ and the H_2O concentration in the glass ($C_{\text{H}_2\text{O}}$) showing the estimated source values (stars; derived from calorimetry) and the measured surface values (points) assuming the estimated storage temperature of (a) $T = 1123$ K and (b) $T = 1193$ K (Zierenberg et al. 2013; Masotta et al. 2018). The solid black curve is plotted using the Hess and Dingwell (1996) model (see Fig. 4), the dotted and dashed black curves are plotted using the Giordano et al. (2008) model and an average of the Hrafninnuhryggur and IDDP-1 glass compositions, respectively (see Fig. 1). The grey curves are plotted using the Giordano et al. (2008) model with all individual glass analyses from IDDP-1. Above the plot is a histogram of measured $C_{\text{H}_2\text{O}}$ values from: (1) Hrafninnuhryggur lavas $n = 20$ (Tuffen and Castro 2009; Ryan et al. 2015a; Wadsworth et al. 2019; Seropian et al. 2022); (2) Hrafninnuhryggur feeder dyke(s) approximately 35–50 and 90 m below the paleo-surface $n = 57$ (Tuffen and Castro 2009; Tuffen et al. 2010; Foster et al. 2024); and (3) KJ-39 $n = 36$ (Rule 2020) and IDDP-1 glass chips $n = 67$ (Zierenberg et al. 2013; Lowenstern and Pitcher 2013; Watson 2018; Bindeman et al. 2021; Saubin et al. 2021).

[column width]

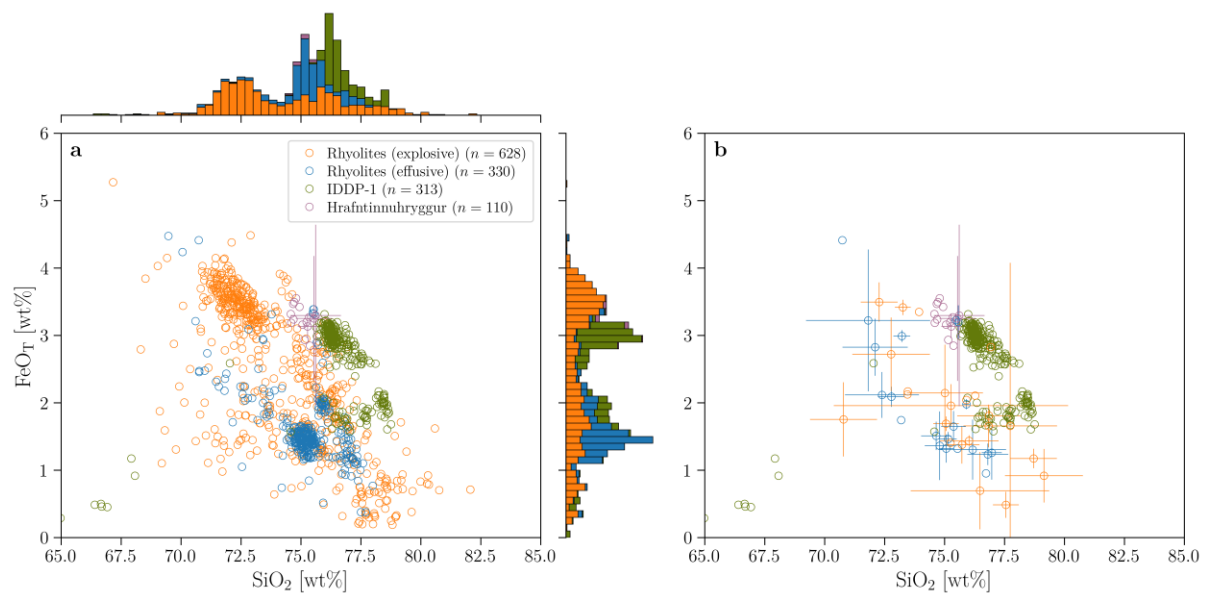


Figure 9. The major element composition of the Hrafninnuhryggur rhyolite glass (purple) and the IDDP-1 glass (green) using the published major element analysis with associated uncertainty (Tuffen and Castro 2009; Zierenberg et al. 2013; Masotta et al. 2018; Saubin et al. 2021). Here, we compare those compositions with rhyolite glass measurements split into the products of explosive eruptions and the products of effusive eruptions worldwide (Di Genova et al. 2017). The Hrafninnuhryggur and IDDP-1 rhyolites are especially iron-rich when compared with a global distribution of effusive lavas (see the histogram associated with the C_{FeO_T} data here) with implications for the propensity for nanolite formation. Compositions are re-normalized to anhydrous 100%. (a) All individual analyses. (b) Only the mean of any given eruption product. Note that (b) is more representative because it acknowledges that most of the high- FeO_T analyses in (a) come from a single eruption (Cordón Caulle 2011-12; Chile).

[page width]